ALTERNATIVE SURFACE TEXTURING, PASSIVATION AND CHARGE SELECTIVE CONTACTS FOR CRYSTALLINE SILICON SOLAR CELLS

A THESIS SUBMITTED TO
THE GRADUATE SCHOOL OF NATURAL AND APPLIED SCIENCES
OF
MIDDLE EAST TECHNICAL UNIVERSITY

BY

ELİF SARIGÜL DUMAN

IN PARTIAL FULFILLMENT OF THE REQUIREMENTS
FOR
THE DEGREE OF DOCTOR OF PHILOSOPHY
IN
MICRO AND NANOTECHNOLOGY

SEPTEMBER 2022

Approval of the thesis:

ALTERNATIVE SURFACE TEXTURING, PASSIVATION AND CHARGE SELECTIVE CONTACTS FOR CRYSTALLINE SILICON SOLAR CELLS

submitted by **ELİF SARIGÜL DUMAN** in partial fulfillment of the requirements for the degree of **Doctor of Philosophy** i**n Micro and Nanotechnology, Middle East Technical University** by,

Prof. Dr. Halil Kalıpçılar
Dean, Graduate School of **Natural and Applied Sciences** _____

Prof. Dr. Deniz Üner
Head of the Department, **Micro and Nanotechnology** _____

Prof. Dr. Raşit Turan
Supervisor, **Physics, METU** _____

Assoc. Prof. Dr. Selçuk Yerci
Co-Supervisor, **Electrical and Electronics Eng., METU** _____

Examining Committee Members:

Prof. Dr. Uğur Serincan
Physics, Eskişehir Technical University _____

Prof. Dr. Raşit Turan
Physics, METU _____

Prof. Dr. Hamza Kurt
School of Electrical Engineering, KAIST _____

Prof. Dr. Alpan Bek
Physics, METU _____

Assoc. Prof. Dr. E. Görkem Günbaş
Chemistry, METU _____

Date: 02.09.2022

I hereby declare that all information in this document has been obtained and presented in accordance with academic rules and ethical conduct. I also declare that, as required by these rules and conduct, I have fully cited and referenced all material and results that are not original to this work.

Name Last name : Elif Sarıgül Duman

Signature :

ABSTRACT

ALTERNATIVE SURFACE TEXTURING, PASSIVATION AND CHARGE SELECTIVE CONTACTS FOR CRYSTALLINE SILICON SOLAR CELLS

Sarıgül Duman, Elif
Doctor of Philosophy, Micro and Nanotechnology
Supervisor: Prof. Dr. Raşit Turan
Co-Supervisor: Assoc. Prof. Dr. Selçuk Yerci

September 2022, 130 pages

This study focuses on realizing three crucial steps in silicon solar cell manufacturing by utilizing alternative methods. Black silicon is of interest as an alternative surface texturing method for achieving enhanced light trapping and reduced reflection of the crystalline silicon solar cell. Black silicon fabrication via the inductively coupled plasma reactive ion etching method and the feasibility of black silicon solar cells were investigated. Reduced optical reflectance was achieved with a total weighted average reflectance as low as 2.3% with superior uniformity. By the investigations conducted to comprehend potential loss mechanisms in the silicon solar cells, black silicon PERC solar cell was realized with a power conversion efficiency of 19.7%.

As an alternative silicon surface passivation method, ozone-based thermal atomic layer deposited aluminum oxide films were investigated. The influence of oxidant precursors in atomic layer depositions was examined regarding silicon surface passivation quality. Its potential applications, such as the passivation of crystalline silicon surfaces in PERC solar cells, were discussed. A simplified process flow for the rear passivation stack of PERC solar cell was proposed by eliminating the out-

gassing step. Superior silicon surface passivation was demonstrated by aluminum oxide/silicon nitride stacks with an implied open-circuit voltage of 730 mV.

Considering the intrinsic drawbacks of doped amorphous films and complex deposition requirements, carrier selective contact formation by a low-cost, vacuum-free method was proposed. Organic self-assembled organic molecules, namely FOPA and 2PACz, were investigated as novel and alternative electron-selective contact in silicon heterojunction solar cells. The stability of organic films under ambient air was demonstrated. Silicon heterojunction solar cells with organic molecule modified electron-selective contacts were developed, resulting in a power conversion efficiency of 16.5%.

Keywords: Black silicon, Inductively coupled plasma reactive ion etching, Charge carrier selective contacts, Self- assembled organic molecules, Surface passivation

ÖZ

KRİSTAL SİLİSYUM GÜNEŞ HÜCRELERİ İÇİN ALTERNATİF YÜZEY DOKULANDIRMA, PASİVASYON VE YÜK SEÇİCİ KONTAKLAR

Sarıgül Duman, Elif
Doktora, Mikro ve Nanoteknoloji
Tez Yöneticisi: Prof. Dr. Raşit Turan
Ortak Tez Yöneticisi: Doç. Dr. Selçuk Yerci

Eylül 2022, 130 sayfa

Bu çalışma silisyum güneş hücresi üretiminde yer alan üç önemli basamağın alternatif yöntemlerle gerçekleştirilmesine odaklanmaktadır. Siyah silisyum, kristal silisyum güneş hücrelerinin ışık hapsetme özelliğini geliştirmek ve yansıma kayıplarını azaltmak için alternatif bir yüzey dokulandırma yöntemi olarak ilgi çekmektedir. Bu çalışmada, reaktif iyon aşındırma yoluyla siyah silisyum üretimi ve güneş hücrelerine uygulanabilirliği araştırılmıştır. Üstün yeknesaklıkla %2.3'e kadar düşük toplam ağırlıklı ortalama yansıma elde edilmiştir. Silisyum güneş hücrelerindeki potansiyel kayıp mekanizmalarını anlamak üzere yapılan çalışmalar sonucu %19.7 verime sahip siyah silisyum PERC güneş hücresi üretilmiştir.

Alternatif bir silisyum yüzey pasivasyon yöntemi olarak, ozon bazlı termal atomik katman biriktirme kullanılarak kaplanan aluminyum oksit tabakalar incelenmiştir. Atomik katman biriktirme yönteminde kullanılan çeşitli oksitleyicilerin silisyum yüzey pasivasyon kalitesiyle ilgisi incelenmiştir. PERC güneş hücrelerinde kristal silisyumun pasifleştirilmesi gibi potansiyel uygulamaları tartışılmıştır. Gazdan arındırma adımı ortadan kaldırılarak, PERC güneş hücrelerinin arka yüzey pasivasyonu için basitleştirilmiş bir işlem önerilmiştir. Üstün silisyum yüzey

pasivasyonuyla 730 mV açık devre potansiyeline sahip alüminyum oksit/silisyum nitrat yığınları üretilmiştir.

Katkılı amorf filmlerin materyal dezavantajları ve karmaşık kaplama gereksinimleri göz önüne alınarak, buna alternatif olarak düşük maliyetli, atmosferik yöntemle yük seçici kontak oluşumu önerilmiştir. Silisyum heteroeklem güneş hücrelerinde yeni ve alternatif elektron seçici kontak olarak FOPA ve 2PACz kendiliğinden kaplanan organik moleküller araştırılmıştır. Organik filmlerin oda koşullarında dayanıklılığı gösterilmiştir. Organik moleküllerle modifiye edilmiş elektron seçici kontaklara sahip silisyum heteroeklem güneş hücreleri üretilmiş ve %16.5 verim elde edilmiştir.

Anahtar Kelimeler: Siyah silisyum, Endüktif olarak eşleştirilmiş plazma reaktif iyon aşındırma, Yük seçici kontaklar, Kendiliğinden oluşan organik moleküller, Yüzey pasivasyonu

Dedicated to my beloved family and the memory of my grandparents

ACKNOWLEDGMENTS

First and foremost, I would like to express my deepest gratitude to my supervisor Prof. Dr. Raşit Turan for his excellent guidance, advice, encouragement, and insights throughout the research. I would also thank him for providing all the facilities at ODTÜ-GÜNAM to be able to conduct this study. I would like to thank Prof. Dr. Alpan Bek as my former supervisor and thesis monitoring committee member. His encouragement throughout this work means a lot to me. I would also like to thank Assoc. Prof. Dr. Selçuk Yerci, Assoc. Prof. Dr. E. Görkem Günbaş and Prof. Dr. Hamza Kurt for their valuable contributions, and suggestions.

I would like to express my gratitude to Prof. Dr. Stefan Glunz for giving me the opportunity to conduct an essential part of this work at Fraunhofer ISE. I would like to thank Dr. Armin Richter, Dr. Christian Reichel, and Dr. Martin Bivour for their time and valuable guidance throughout my studies at Fraunhofer ISE. I would like to thank all Fraunhofer ISE collaborators Dr. Christoph Luderer, Dr. Leonard Tutsch, Dilara Kurt, Dr. Jana-Isabelle Polzin, Dr. Thibaut Hatt, Dr. Markus Kohlstädt, Dr. Anamaria Moldovan, and Dr. Martin Hermle. I would like to thank them for their supportive attitude and for providing an encouraging working environment during my two-year visit to Fraunhofer ISE.

I am very grateful to all my colleagues at ODTÜ-GÜNAM, especially Dr. Gence Bektaş, Ahmet Emin Keçeci, Sümeyye Koçak Bütüner, Hasan Hüseyin Canar, Hasan Asav, Ateş Aliefendioğlu, Milad Ghasemi, and Dr. Bülent Arıkan for their valuable contributions.

I would like to acknowledge the technical support of Tayfun Yıldız, Furkan Çiçek, Murat Aynacıoğlu, Batuhan Taş, Samet Özdemir, Toni Leimenstoll, Felix Schätzle, Christian Schetter, Harald Steidel, Karin Zimmermann, and Felix Martin.

I would also like to thank Atılım University Physics Group and THK University Aviation Engineering Department, where I worked in the first years of my Ph.D.

It is kindly acknowledged the support from Scientific and Technological Research Council of Turkey (TÜBİTAK) 1003 Primary Subjects R&D Funding Program under grant number 218M994, TÜBİTAK BIDEB-2214/A International Research Fellowship Program for Ph.D. Students under grant number 1059B14180160, TÜBİTAK under grant number 119N339, and 218M994.

I would like to express my gratitude to my dear friends Tuğba Bulut, Merve Turhan Babur, Dr. Selen Postacı, Dr. Çidem Argunhan Atalay, and Dr. Arzu Arslan Kelam, who are always at my side and enrich my life.

Finally, I would like to thank my family for their endless support through all these difficult times. My special thanks go to my dear Burak for his unconditional and immeasurable love, patience and for giving me the motivation and strength throughout my life.

TABLE OF CONTENTS

ABSTRACT v

ÖZ vii

ACKNOWLEDGMENTS x

TABLE OF CONTENTS xii

LIST OF TABLES xv

LIST OF FIGURES xvi

LIST OF ABBREVIATIONS xxi

LIST OF SYMBOLS xxv

CHAPTERS

1 INTRODUCTION 1

1.1 Motivation 3

1.2 Outline 4

2 FUNDAMENTALS 5

2.1 Silicon Surface Texturing and Black Silicon Method 5

2.2 Silicon Solar Cell Operation Principle 11

2.3 Silicon Surface Passivation 16

2.4 Atomic Layer Deposition 18

2.5 Charge Transport Mechanism in Solar Cells 21

3 CHARACTERIZATION METHODS 23

3.1 Reflectance and Transmittance Measurements 23

3.2 Contact Resistance Measurement 25

3.3 Quasi-Steady-State Photoconductance Measurement 28

3.4 Fourier Transform Infrared Spectroscopy 28

3.5 X-Ray Photoelectron Spectroscopy 29

4 CRYSTALLINE SILICON SURFACE PASSIVATION FOR PERC SILICON SOLAR CELL APPLICATIONS 31

4.1 Silicon Surface Passivation via ALD Al_2O_3: Effect of Oxidant Precursor on Silicon Passivation Quality 32

4.1.1 Experimental Details 32

4.1.2 Results and Discussion 34

4.1.3 Conclusion 39

4.2 C-Si Surface Passivation via Ozone-Based Thermal-ALD Al_2O_3 40

4.2.1 Experimental Details 40

4.2.2 Results and Discussion 41

4.2.3 Conclusion 50

4.3 Thermal-ALD Ozone Concentration-Dependent c-Si Surface Passivation for PERC Applications 51

4.3.1 Experimental Details 51

4.3.2 Results and Discussion 52

4.3.3 Conclusion 62

5 BLACK SILICON FABRICATION VIA ICP-RIE AND ITS INCORPORATION IN SILICON SOLAR CELLS 65

5.1 Black Silicon Fabrication via Reactive Ion Etching Method 67

5.1.1 Experimental Details 67

5.1.2 Results and Discussion 67

5.1.3 Conclusion 73

5.2 Influence of Phosphorus Emitter Formation on the Performance of Black Silicon PERC Solar Cells 74
5.2.1 Experimental Details 74
5.2.2 Results and Discussion 77
5.2.3 Conclusion 83
6 DOPANT-FREE CHARGE SELECTIVE CONTACTS FOR C-SI HETEROJUNCTION SOLAR CELLS 85
6.1 Self-Assembled Organic Molecule-Modified Charge Selective Contacts 87
6.1.1 Experimental Details 87
6.1.2 Results and Discussion 90
6.1.3 Conclusion 101
7 CONCLUSION AND OUTLOOK 103
REFERENCES 107
APPENDICES
A. Fast-Firing Profile for PERC Solar Cells 127
CURRICULUM VITAE 129

LIST OF TABLES

TABLES

Table 4.1 Optimized ozone-based thermal ALD Al_2O_3 deposition parameters 45
Table 4.2 Blistering behavior of samples with Al_2O_3/SiN_x stacks for each Al_2O_3 deposition temperature, ozone concentration, Al_2O_3 thickness, and annealing process. Color code: green represents no blistering, yellow (with 'x') represents partial inhomogeneous blistering on some samples, and red (with 'xx') represents severe blistering on samples. 62
Table 5.1 Total weighted average reflectance of b-Si samples with various pre-etching treatments. 71
Table 5.2 Optimized ICP-RIE etching parameters for the b-Si fabrication..... 73
Table 5.3 Surface texturing methods and sequences employed for each group for various surface morphologies 74
Table 5.5 Solar cell parameters of PERC solar cells with implanted emitter extracted from the light J-V measurements. 81
Table 5.6 Solar cell parameters of PERC solar cells with diffused emitter extracted from the light J-V measurements. 81
Table 5.7 Solar cell parameters of PERC solar cells with diffused (denoted as dif.) or implanted emitter with improved front fingers extracted from the light J-V measurements. 83
Table 6.1 Spin-coating and consecutive hotplate annealing process parameters of self-assembled molecule depositions. 88
Table 6.2 Composition of the sample surface given in atomic %..... 100
Table 6.3 Chemical states of O on FOPA and 2PACz deposited c-Si surfaces.... 101

LIST OF FIGURES

FIGURES

Figure 1.1 The change in the share of renewable resources in global power generation over the years [1]. 2
Figure 2.1 SEM images of alkaline textured c-Si resulting in random pyramids on the c-Si surface from a) the top view, b) the tilted view. 6
Figure 2.2 a) Reflected and transmitted counterparts of the incident light on planar silicon surface b) Schematic illustration of light trapping property of the structured silicon. 7
Figure 2.3 SEM images of the various black silicon nanostructures fabricated by different methods, taken from [8] and [9]. 8
Figure 2.4 A schematic illustration of the black silicon formation by the reactive ion etching method. 10
Figure 2.5 Energy band diagram of a p-n junction in forward bias demonstrating quasi-Fermi levels. 12
Figure 2.6 Recombination mechanisms in a semiconductor. 13
Figure 2.7 Current-voltage characteristics of a solar cell in the dark (black) and under illumination (red). 15
Figure 2.8 Schematic representation of silicon-oxide interface and the associated charges, redrawn from [15]. 18
Figure 2.9 Schematic illustration of the ALD cycle and self-terminating surface reaction mechanism 19
Figure 2.10 Schematic representation of a) ALD reactor b) ALD cycles of thermal ALD and c) plasma-assisted ALD for Al_2O_3 depositions, adapted from [19]. 20
Figure 2.11 Growth per cycle as a function of deposition temperature and the corresponding growth mechanisms. 21
Figure 3.1 Schematic representation of integrating sphere demonstrating a) total reflectance and b) diffuse reflectance measurements, redrawn from [20]. 24

Figure 3.2 Two-terminal dark I-V measurement and corresponding equivalent circuit for the contact resistivity calculation. 25
Figure 3.3 Schematic representation of TLM test structure a) top view b) cross-sectional view. 26
Figure 3.4 The measured resistance as a function of distance L 27
Figure 4.1 Spectroscopic ellipsometry measurement results for varied ALD cycles. Inset shows implication of interfacial silicon oxide formation and initial growth delay. 35
Figure 4.2 Injection-dependent effective minority carrier lifetime τ_{eff} of 10 nm thick plasma-assisted ALD Al_2O_3 deposited n-type c-Si sample for varied FGA temperatures. 36
Figure 4.3 Comparison of effective minority carrier lifetimes of Al_2O_3 deposited samples for varied Al_2O_3 thickness and FGA temperature on p-type (top row) and n-type (bottom row) c-Si samples. 38
Figure 4.4 Implied open-circuit voltage values at 1-sun illumination extracted from PCD measurements for a) p-type c-Si and b) n-type c-Si samples passivated by varied ALD Al_2O_3 films after FGA at 500 ℃ and 550 ℃. 39
Figure 4.5 Growth per ALD cycle of Al_2O_3 films depending on O_3 purge time for varied O_3 dose times and O_3 concentrations. 42
Figure 4.6 Growth per ALD cycle of Al_2O_3 films depending on O_3 concentration and O_3 dose time. 43
Figure 4.7 Change in growth per ALD cycle of Al_2O_3 films depending on O_3 dose time for varied O_3 purge times and depositions with O_3 concentration of 20% wt.. 44
Figure 4.8 GPC behavior depending on the ALD deposition temperature. GPC values of ALD Al_2O_3 depositions by using Atlas 30 ozone generator is adopted from [34]. 45
Figure 4.9 Injection-dependent effective minority carrier lifetime τ_{eff} of the ozone-based ALD Al_2O_3 deposited samples with varied ozone concentration and

deposition temperature after FGA treatment at a temperature of a) 425 ℃ and b) 500 ℃. 46
Figure 4.10 Effective lifetime results of n-type c-Si samples at an injection level of $\Delta n = 3 \times 10^{15} cm^{-3}$ depending on ALD ozone concentration and the deposition temperature. 47
Figure 4.11 Implied open-circuit voltage iV_{oc} of ozone-based ALD Al_2O_3 deposited samples, measured at 1-sun illumination. 48
Figure 4.12 Overview FTIR spectra of ALD Al_2O_3 films deposited at varied deposition temperatures and with varied ozone concentrations. 49
Figure 4.13 FTIR spectra and assigned vibrational modes of ALD Al_2O_3 films for varied deposition temperature and ozone concentrations. 50
Figure 4.14 Process flow for Al_2O_3 and Al_2O_3/SiN_x samples with varied ALD parameters. 52
Figure 4.15 a) Photograph and b) Photoluminescence (PL) image of c-Si wafer after Al_2O_3/SiN_x stack deposition. 53
Figure 4.16 Thickness mapping of Al_2O_3 layer deposited at 300 ℃ with an ozone concentration of 20% wt. 54
Figure 4.17 QSS-PL calibrated effective lifetime images of Al_2O_3 deposited samples without any thermal treatment. 55
Figure 4.18 PL calibrated effective lifetime images of Al_2O_3 deposited samples with varied ALD deposition temperatures, ozone concentrations and Al_2O_3 thicknesses after FGA at 500 ℃. 56
Figure 4.19 Effective charge carrier lifetime results of ozone-based ALD Al_2O_3 samples after consecutive FGA. 57
Figure 4.20 Effective charge carrier lifetime results of Al_2O_3/SiN_x stacks after consecutive FGA. 59
Figure 4.21 Effective charge carrier lifetime results of Al_2O_3/SiN_x stacks after fast-firing with varied temperatures. Samples showing blistering are indicated by letter the ‘B’. 60

Figure 4.22 Some exemplary microscope images of Al_2O_3/SiN_x stacks after fast-firing to demonstrate blistering behavior. 61
Figure 5.1 B-Si fabrication process results before the modification of ICP-RIE tool and the process optimization. 68
Figure 5.2 Photograph of ICP-RIE processed c-Si wafers a) before and b) after the process optimization. 69
Figure 5.3 SEM images of b-Si samples processed by ICP-RIE mode (a and b) or RIE mode (c and d) 70
Figure 5.4 Total reflectance spectra of b-Si on the samples with different pre-etching treatments. 71
Figure 5.5 Total reflectance of b-Si samples fabricated on SDE c-Si with varied chamber pressure and process durations. 72
Figure 5.6 Process flow of PERC solar cell fabrication. 76
Figure 5.7 Schematic cross-sections of PERC solar cells with a) diffused emitter and b) implanted emitter. 76
Figure 5.8 SEM images of each group subjected to various surface texturing treatments. 77
Figure 5.9 Total reflectance spectra of a) textured c-Si wafers with various surface morphologies b) the solar cells with SiO_xN_y/SiN_x ARC film and metal grid. 78
Figure 5.10 Open-circuit voltage values as a function of fast-firing peak temperature and firing belt speed for b-Si (denoted as Tex. 1) and pyramidal textured (denoted as Pyr.) c-Si PERC solar cells. 79
Figure 5.11 Photograph of pyramidal textured (left) and b-Si textured solar cells. 79
Figure 5.12 Contact resistivity of Ag screen-printed Ag front fingers on varied surface textures. 82
Figure 6.1 Bonding of the phosphonic acid to the surface with different modes: a) monodentate, b) bidentate with H bonding to the surface, c) bidentate, d) tridentate, e) bidentate with residual H bonding to the surface -OH group. Taken from [161]. 86

Figure 6.2 Molecular structures of organic molecules used as charge selective contacts: a) FOPA ($C_8H_6F_{13}O_3P$), b) 2PACz ($C_{14}H_{14}NO_3P$).....87
Figure 6.3 Schematic cross-sections of a) symmetrical test structures and b) ρ_c test structures on n-type and p-type c-Si for the carrier selectivity and the contact resistivity analyses.....89
Figure 6.4 a) Schematic cross-section of SHJ solar cells with organic molecule modified electron-selective contacts b) Photograph of the front side of the organic molecule modified SHJ solar cells. 90
Figure 6.5 Dark I-V characteristics of the contact resistivity test structures for varied stacks capped by Al on (a) n-type c-Si and (b) p-type c-Si.....91
Figure 6.6 Screening FOPA and 2PACz contact resistivity for various stacks and metals on n-type and p-type c-Si contact resistivity test structures.....93
Figure 6.7 Stability of contact resistivity for FOPA/Al and 2PACz/Al contacts after hotplate annealing and storage under ambient air. 94
Figure 6.8 Light J-V measurements of SHJ solar cells: a) Open-circuit voltage, b) fill factor, c) short-circuit current density, d) power conversion efficiency.....96
Figure 6.9 J-V characteristics of the SHJ solar cells under illumination. 97
Figure 6.10 Evolution of SHJ solar cell parameters as a function of annealing temperature: (a) Open-circuit voltage, (b) fill factor, (c) short-circuit current density, (d) power conversion efficiency. 98
Figure 6.11 External quantum efficiency and the corresponding reflectance spectra of the SHJ solar cells with varied electron-selective contacts.....99
Figure 6.12 The survey spectra of the substrate and organic molecule deposited surfaces. 100
Figure A.7.1 Fast-firing profile for PERC solar cells 127

LIST OF ABBREVIATIONS

ABBREVIATIONS

Ag	silver
Al	aluminum
Al-BSF	aluminum back surface field
ALD	atomic layer deposition
AM1.5g	Air mass 1.5 global spectrum
ARC	anti-reflection coating
a-Si:H	hydrogenated amorphous silicon
a-Si:H(i)	hydrogenated intrinsic amorphous silicon
ATR	attenuated total reflection
AZO	aluminum zinc oxide
BSF	back surface field
BSG	borosilicate glass
b-Si	black silicon
CB	conduction band
CCP	capacitively coupled plasma
CPS	counts per second
c-Si	crystalline silicon
CVD	chemical vapor deposition
CZ	Czochralski

DRIE	deep reactive ion etching
EQE	external quantum efficiency
FF	fill factor
FFC	Fray-Farthing-Chen
FGA	forming gas annealing
FOPA	1H,1H,2H,2H-Perfluorooctanephosphonic acid
FTIR	Fourier transform infrared
FZ	float-zone
GPC	growth per cycle
HIT	heterostructure with intrinsic thin layer
IBC	interdigitated back contact
ICP-RIE	inductively coupled plasma reactive ion etching
IR	infrared
ITO	indium tin oxide
MACE	metal-assisted chemical etching
MEMS	micro-electro-mechanical systems
OPV	organic photovoltaics
PA	phosphonic acid
PCD	photoconductance decay
PCE	power conversion efficiency
PECVD	plasma-enhanced chemical vapor deposition
PERC	passivated emitter and rear contact

PERT	passivated emitter and rear totally diffused
PIII	plasma immersion ion implantation
PL	photoluminescence
PSG	phosphosilicate glass
PV	photovoltaic
QSS	quasi-steady-state
QSSPC	quasi-steady state photoconductance
RF	radio frequency
RIE	reactive ion etching
RPM	revolutions per minute
SAM	self-assembled monolayer
sccm	standard cubic centimeters per minute
SDE	saw damage etched
SEM	scanning electron microscope
SERS	surface-enhanced Raman scattering
SHJ	silicon heterojunction
SLM	standard liter per minute
SRH	Shockley-Read-Hall
TCO	transparent conductive oxide
TLM	transfer length method
TMA	trimethylaluminum
XPS	X-ray photoemission spectroscopy

VB	valance band
VLS	vapor-liquid-solid
2PACz	[2-(9H-Carbazol-9-yl)ethyl]phosphonic acid
4pp	4-point-probe

LIST OF SYMBOLS

SYMBOLS

Al_2O_3	aluminum oxide
$Al(CH_3)_3$	trimethylaluminum
AZO	aluminum zinc oxide
$BaSO_4$	barium sulfate
D_{it}	interface defect density
E_{be}	binding energy
E_g	bandgap energy
HCl	hydrochloric acid
HF	hydrofluoric acid
HNO_3	nitric acid
H_2O	water
ITO	indium tin oxide
iV_{oc}	implied open-circuit voltage
I_{sc}	short-circuit current
J_{ph}	photogenerated current density
J_{sc}	short-circuit current density
KOH	potassium hydroxide
O_2	oxygen
O_3	ozone

P	phosphorus
PEDOT:PSS	poly(3,4-ethylenedioxythiophene) polystyrene sulfonate
$POCl_3$	phosphoryl chloride
R_c	contact resistance
R_S	series resistance
R_{SH}	Shunt resistance
R_{sheet}	sheet resistance
R_w	total weighted average reflectance
SF_6	sulfur hexafluoride
SiO_2	silicon oxide
SiN_x	silicon nitride
$Si_xO_yF_z$	silicon oxyfluoride
SiO_xN_y	silicon oxynitride
TiO_2	titanium oxide
T_{Dep}	deposition temperature
V_{oc}	open-circuit voltage
Δn	excess carrier density
η	power conversion efficiency
τ_{eff}	effective carrier lifetime
ρ_c	contact resistivity

CHAPTER 1

INTRODUCTION

Energy consumption demand in the industrialized world is colossal, and this demand keeps on increasing every day. As of 2022, fossil fuels are still the world's primary energy source. However, this excessive energy requirement cannot be matched by conventional energy resources (i.e., oil, natural gas, or coal) because of limited natural resources and high carbon emission concerns. Considering these problematic fossil resource consumption aspects, the world's primary energy supply must be replaced by renewable energy resources. The change in the share of renewable resources in global power generation compared to coal and natural gas is shown in Figure 1.1. The annual growth rate of renewable energy generation, which was higher than the annual growth rate of all other energy sources in 2021, was reported as 16.5% by bp Statistical Review of World Energy 2021. As a result, global renewable generation capacity has reached 3657 TWh, with an annual increase of 510 TWh at the end of 2021. Solar energy played the most significant role in this generation capacity expansion, with a rise of 22.3% [1]. This is because solar energy has several advantages over other renewable energy sources in terms of sustainability, production cost and consequential cost to the environment and climate. Solar energy became the most cost-effective renewable energy source in 2019. Therefore, considering the zero carbon emission targets of the countries by 2050, it is foreseen that the development of the photovoltaic industry will be several times larger than it has been thus far and that its market share among energy resources will expand in the coming years.

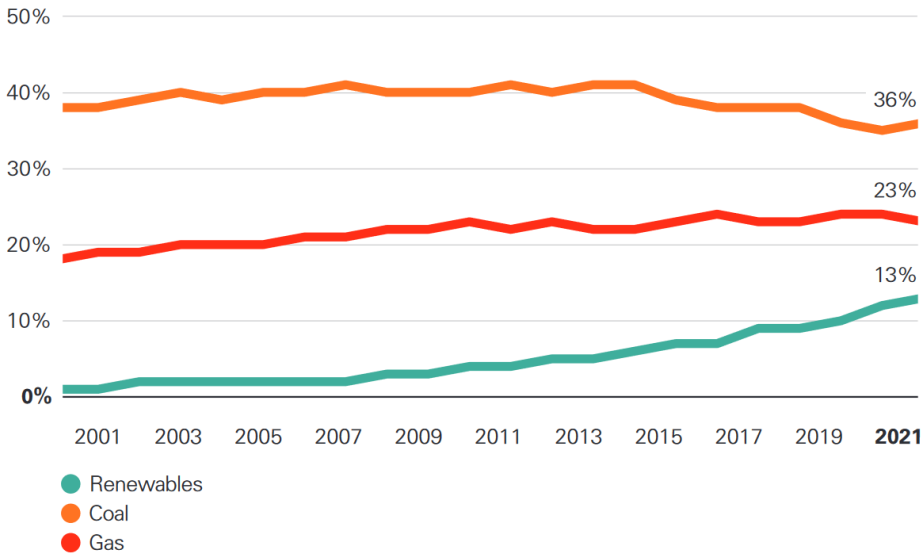

Figure 1.1 The change in the share of renewable resources in global power generation over the years [1].

Solar cells have a history dating back to even 1830s when Edmond Becquerel discovered that an electric current is generated by the illumination of two separate brass plates by the light that are immersed in a conductive liquid [2]. However, the principles of this mechanism were not known at the time. These principles were identified much later. After the introduction of quantum theory in early the 1900s and the invention of the bipolar transistor in 1947, the semiconductor industry started to grow rapidly. The first c-Si solar cell with a conversion efficiency of 6% was fabricated by Chapin et al. in 1954 [3]. C-Si solar cells have been dominating technology in the photovoltaic (PV) industry as silicon is robust and one of the most abundant materials on earth. Moreover, industrial processing techniques of silicon-based PV have advanced over time. Currently, the maximum efficiency limits that can be achieved using c-Si combined with various technologies and structures such as passivated emitter and rear contact (PERC), passivated emitter and rear totally diffused (PERT), interdigitated back contact (IBC), or heterostructure with intrinsic thin layer (HIT) are almost reached and ways to exceed these limits by utilizing tandem structures are being searched.

1.1 Motivation

This thesis study focuses on three main topics to search for an alternative texturing method, the crystalline silicon passivating materials, and the carrier selective contacts for silicon solar cells.

The first part of the study focuses on the effect of oxidant precursors on silicon surface passivation by atomic layer deposited aluminum oxide layers. Moreover, the effect of post-deposition treatments, such as annealing and fast-firing, is investigated in detail. The second part consists of black silicon fabrication via the reactive ion etching method and its implementation in homojunction crystalline silicon solar cells. The third part focuses on dopant-free charge selective contacts for silicon heterojunction solar cell applications.

This thesis study targets the following key objectives:

- **Investigate alternative materials for the surface passivation of silicon:** Investigation of the passivation property and the material quality of ozone-based thermal atomic layer deposited aluminum oxide films after the post-annealing treatments to examine the applicability of aluminum oxide films to PERC solar cells. It is targeted to achieve a good level of passivation to increase open-circuit voltage of the solar cells. Moreover, process simplification for the PERC solar cell fabrication is aimed at the process flow without any out-gassing step.
- **Black silicon as an alternative surface texturing method:** Black silicon (b-Si) fabrication via reactive ion etching (RIE) method to investigate its surface morphology and optical properties. It is targeted to increase light coupling into the silicon solar cell by black silicon and obtain a high short-circuit current in the silicon solar cell. Moreover, it is aimed to fabricate black silicon PERC solar cells with enhanced light coupling in the device.
- **Alternative charge carrier selective materials for silicon heterojunction solar cells**: Investigating novel organic materials as charge selective contacts

in silicon heterojunction solar cells to replace doped amorphous silicon layers with cost-effective, solution-based self-assembled organic layers.

1.2 Outline

The fundamental basis and relevant theoretical information are introduced in Chapter 2.

The fundamental characterization methods used during the research are introduced in Chapter 3.

A systematic experimental study on crystalline silicon surface passivation via atomic layer deposited aluminum oxide films and the influence of oxidant precursor are presented in Chapter 4. Moreover, a simplified process flow for surface passivation of rear side of PERC solar cell is proposed in Chapter 4.

Large area black silicon fabrication via inductively coupled plasma reactive ion etching and its implementation in crystalline silicon solar cells is addressed in Chapter 5.

Alternative self-assembled organic molecule-based dopant-free electron-selective contacts are presented in Chapter 6.

The main findings of the study are summarized and the outlook for further studies is presented in Chapter 7.

CHAPTER 2

FUNDAMENTALS

2.1 Silicon Surface Texturing and Black Silicon Method

Effective light absorption is a crucial requirement to generate charge carriers (electron-hole pairs) in a solar cell. The absorption depends on the reflectivity of the material, which can be reduced by using various strategies. Surface texturing and depositing anti-reflection coating (ARC) film having a suitable refractive index are the most employed methods to minimize reflection losses. ARC approach is based on destructive interference of the light with an optical path difference at the air-ARC interface, which is wavelength-dependent. Therefore, these anti-reflection coating films can suppress the reflection in a narrow spectral range and angles of incidence. Industrial applications of surface texturing rely mainly on the wet chemical etching of the crystalline silicon surface using alkaline solutions. This wet chemical process is based on the anisotropic etching of c-Si due to <100> and <111> crystal planes having different etching rates [4]. As a result, random pyramids are formed on the surface of c-Si. The surface morphology of the c-Si with the random pyramidal texturing via scanning electron microscopy (SEM) imaging is shown in Figure 2.1.

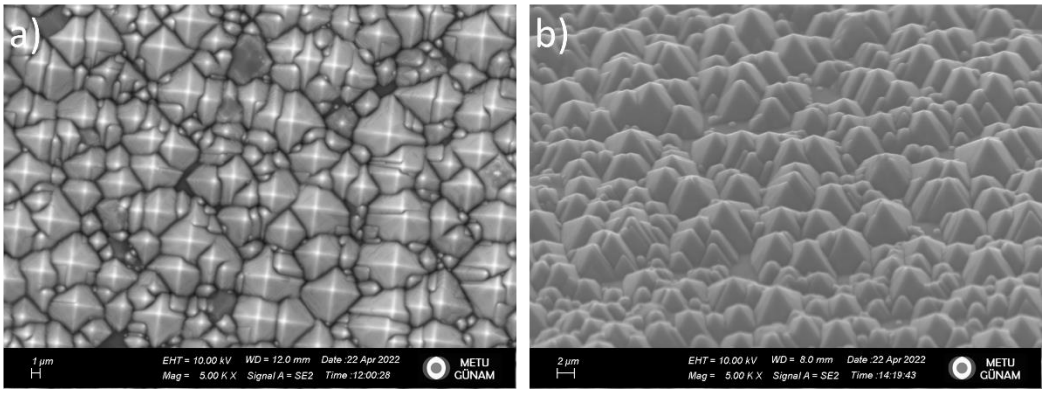

Figure 2.1 SEM images of alkaline textured c-Si resulting in random pyramids on the c-Si surface from a) the top view, b) the tilted view.

In addition to the random pyramidal texturing technique, alternative surface texturing methods include reactive ion etching, metal-assisted chemical etching (MACE), plasma immersion ion implantation (PIII), and laser texturing. One of the unique applications of surface texturing is the black silicon method. Black silicon (b-Si) was first discovered as a side effect of deep trench etching of silicon via RIE using fluorine-based plasma [5]. B-Si has extremely low optical reflectance in an extremely broad-spectrum range with superior light trapping property. Besides geometric light trapping, optical gain is also accomplished based on the change in the refractive index at the air-silicon interface, called the “density-graded index profile” [6]. Moreover, low reflectance is achieved in a wide range of light incident angles. Suppression of reflection obtained by the geometric light trapping property of the structured surface is schematically shown in Figure 2.2. In this case, reflected light has a second chance of being absorbed by the silicon. When nanostructured surfaces are employed, optical path length improvement approaches the Lambertian limit [7].

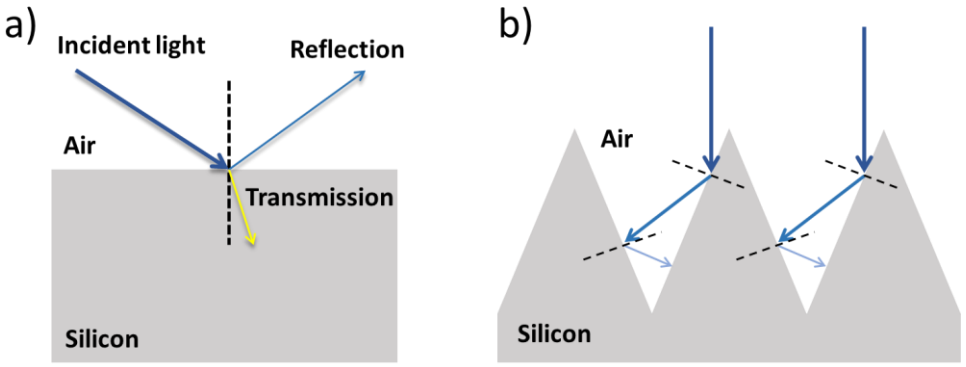

Figure 2.2 a) Reflected and transmitted counterparts of the incident light on planar silicon surface b) Schematic illustration of light trapping property of the structured silicon.

Black silicon can be obtained with various nanostructures, such as cones/spikes, wires/rods, and porous, as shown in Figure 2.3. Random and/or periodic structures can also be formed depending on the chosen method and the process flow. Although surface morphology changes drastically depending on the methodology adopted, reduced reflectance can be achieved for varied surface morphologies resulting in a black appearance.

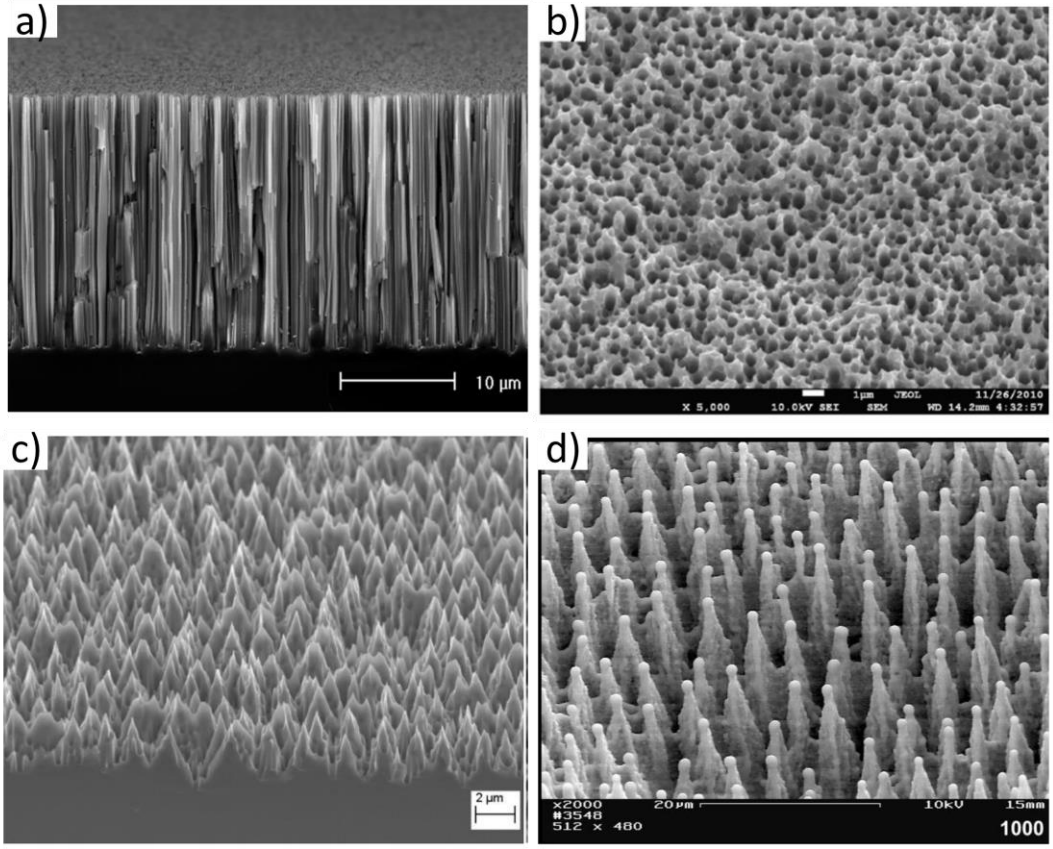

Figure 2.3 SEM images of the various black silicon nanostructures fabricated by different methods, taken from [8] and [9].

Among these black silicon fabrication methods, RIE is of interest in this study. RIE is one of the most robust dry etching methods. A wide range of surface modifications is accomplished via RIE by introducing reactive and passivating gasses into the chamber with varied process conditions. Reactive ion etching comes in various forms, including deep reactive ion etching (DRIE) using cryogenic temperatures or inductively coupled plasma reactive ion etching (ICP-RIE) methods. It is widely employed for microfabrication in the semiconductor manufacturing industry. This study focuses on the etching of silicon and b-Si fabrication via sulfur hexafluoride (SF_6) and oxygen (O_2) gasses. Therefore, the theoretical information provided is primarily limited to that topic.

Black silicon via RIE is based on anisotropic etching of silicon via halogen gasses (i.e., fluorine, chlorine, or bromine) with the incorporation of additive passivating gasses, such as oxygen. If the case where SF_6 and O_2 gases are used is considered, the synergetic influence of fluorine and oxygen radicals on silicon results in a trade-off between etching and passivation of silicon by SF_x^+, F^+ ions, and $Si_xO_yF_z$, respectively. The main reaction occurring with the mixture of SF_6/O_2 plasma is

$$xSi + yO + zF \rightarrow Si_xO_yF_z \tag{2.1}$$

When extreme conditions are considered, etching and passivating reactions can be described as the following.

$$Si + 4F^* \rightarrow SiF_4 \text{ (etching/halogenation)} \tag{2.2}$$

$$Si + 2O \rightarrow SiO_2 \text{ (passivation)} \tag{2.3}$$

These two reactions take place simultaneously on the silicon surface. Silicon halogenation and oxidation are the competing reactions that should be balanced to control the etch profile. Etching and passivation mechanisms for random nano-needle formation are depicted in Figure 2.4. At the beginning of the etching process, $Si_xO_yF_z$ particles constituting the plasma precipitate randomly on the silicon surface. This spontaneous precipitation of the particles also called dust in literature, acts as a random mask on the surface, affecting the etching profile [10]. Sidewall protection occurs either by SiO_2 film deposition due to oxygen in the gas mixture or by oxidation of unsaturated etching species, which redeposit on the sidewalls during the etching process [11]. Under both circumstances, the passivation layer deposited on the sidewalls works as an inhibitor for lateral etching. Therefore, the isotropic chemical etching mechanism is suppressed on the sidewalls. On the other hand, bombarded ions assist the anisotropic etching of the surface. This process is also defined as "ion-enhanced plasma chemical etching with sidewall inhibitor" [12]. The superposition of these chemical etching and ion-assisted physical etching mechanisms results in random nanostructures on the silicon surface. This nano-structured silicon is called "black silicon" due to its minimized reflection resulting in a black appearance.

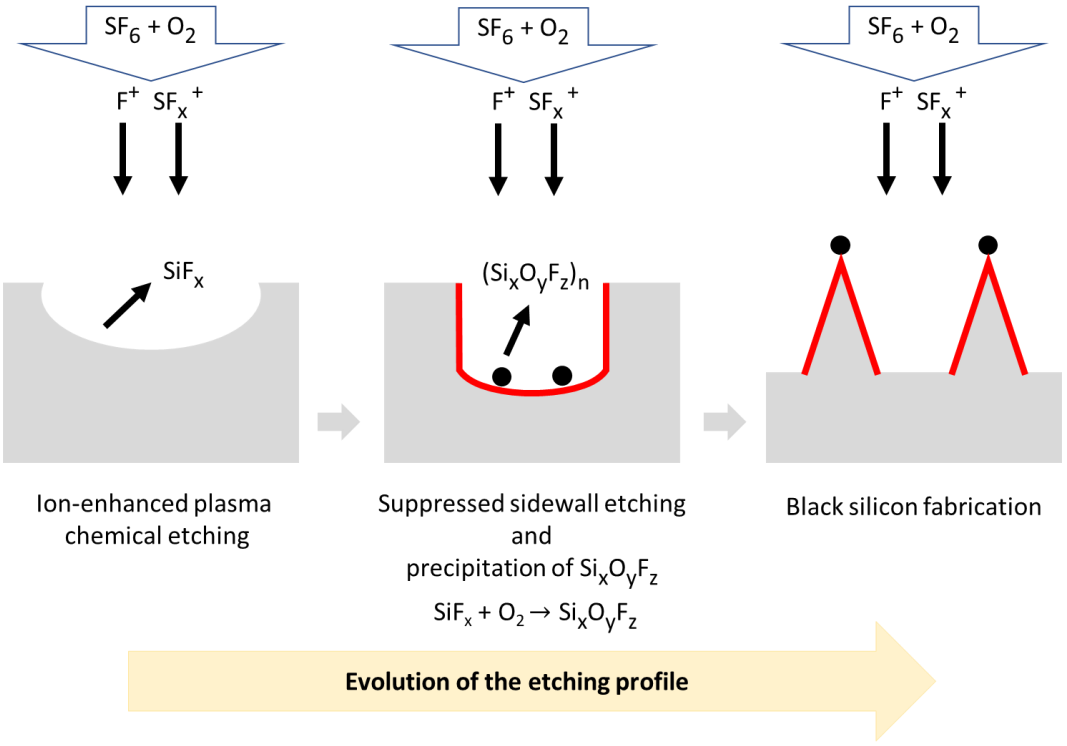

Figure 2.4 A schematic illustration of the black silicon formation by the reactive ion etching method.

Silicon etch rate is a function of the reaction probability of etching species on the surface of the silicon and the density of etching species [13]. Therefore, the etch rate and the resulting surface morphology are strongly influenced by the process parameters, such as radio frequency (RF) power, gas flow ratio, substrate temperature, etching duration, selectivity of the gas mixture, and pressure. Unlike wet chemical etching methods (i.e., metal-assisted chemical etching), the RIE method enables anisotropic etching regardless of crystallographic orientation (i.e., mono-crystalline, or multi-crystalline silicon).

In inductively coupled plasma reactive ion etching (ICP-RIE), plasma excitation and ion acceleration towards the substrate are controlled by two different power sources, allowing additional flexibility during the processes. ICP-RIE has substantial advantages over RIE. Plasma is generated in a separate zone, and a bias voltage is

required for the ion bombardment. Therefore, by using separate power sources, the physical and chemical components of the etching mechanism can be controlled separately, and plasma damage on the substrate is minimized. Moreover, a higher plasma density is obtained compared to conventional RIE, in which plasma is created by capacitively coupled plasma (CCP). Both chemical-dominated and/or physical-dominated etching can be provided by the ICP-RIE method. While the chemical-dominated etching process yields reduced surface damage, the physical-dominated process can result in anisotropic etching with higher aspect ratio structures with the help of the physical bombardment of radicals (ions) [14].

2.2 Silicon Solar Cell Operation Principle

Silicon solar cell working mechanism mainly relies on the p-n junction theory, which is the basis of the semiconductor technology as well. The fundamental working mechanism is based on photogeneration and collection of excess charge carriers. Photogeneration of the excess charge carriers arises from the absorption of the incoming photons. Excess photogenerated electron and hole density (Δn and Δp, respectively) are quantified by the quasi-Fermi level splitting for electrons and holes (E_{Fn} and E_{Fp}) under illumination as follows:

$$E_{Fn} - E_{Fp} = k_B T \ln\left(\frac{(p_0 + \Delta p)(n_0 + \Delta n)}{{n_i}^2}\right) \tag{2.4}$$

where n_i is the intrinsic carrier concentration, n_0 and p_0 are the equilibrium electron and hole concentrations, respectively. Quasi-Fermi levels are demonstrated on the forward-biased p-n junction, which is depicted in Figure 2.5.

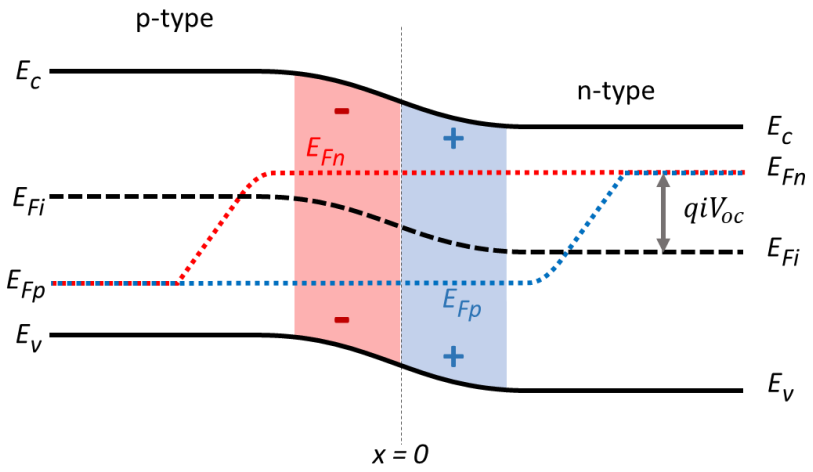

Figure 2.5 Energy band diagram of a p-n junction in forward bias demonstrating quasi-Fermi levels.

The excess charge carrier generation rate depends on the absorption coefficient of the material, which is determined by the bandgap of the semiconductor. The bandgap of a semiconductor in thermal equilibrium is defined as the energy difference between the valance band (VB) and the conduction band (CB). Incoming photons with the energy (E_{ph}) larger than or equal to the semiconductor bandgap (E_g) can generate electron-hole pairs within the semiconductor. On the other hand, a photon with energy lower than the threshold energy is transmitted. High bandgap semiconductors can absorb fewer photons resulting in increased transmission losses. On the other hand, while the generation rate increases for the low bandgap materials, it causes more thermalization losses within the absorber. Because of this compromise between the thermalization losses and transmission losses, precise material selection and solar cell design are required. Since the bandgap is an intrinsic property of the semiconductor, the absorption does not change unless the material is altered or novel technologies are utilized, such as tandem devices (i.e., silicon-perovskite solar cells). In conclusion, how many carriers are generated and how effectively these carriers are collected are the critical aspects of obtaining high short-circuit current density (J_{sc}) values for a high-efficiency solar cell. Therefore, the collection probability of

the carriers is an important parameter determining the light-generated current. The photogenerated electron-hole pairs are separated and collected by the external electrodes to attain electrical energy. However, some recombination mechanisms affect the carrier collection efficiency and hence the external quantum efficiency of the solar cell. There are three recombination mechanisms in the semiconductor, which are depicted in Figure 2.6.

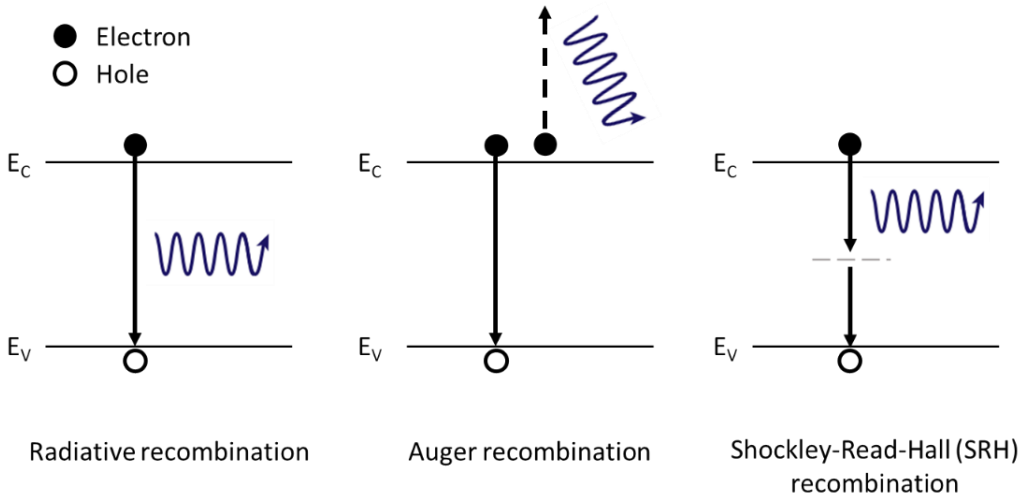

Figure 2.6 Recombination mechanisms in a semiconductor.

- Radiative recombination arises if an electron in the conduction band recombines with a hole in the valance band, which results in emission of a photon. Radiative recombination requires a phonon in an indirect semiconductor, such as silicon, since momentum change via thermal vibration is necessary. Therefore, the radiative recombination rate in silicon is relatively low compared to a direct semiconductor or other recombination mechanisms.
- Auger recombination occurs if the excess energy released from the recombination of an electron-hole pair is transferred to another free carrier (i.e., to an electron or a hole at the conduction band or valance band, respectively). Therefore, Auger recombination requires three carriers. In the

end, the excess energy is dissipated by the collisions with the lattice (thermalization loss). It is known that Auger recombination is more pronounced for higher charge carrier concentrations, such as high injection conditions and/or heavily doped samples.

- Shockley-Read-Hall (SRH) recombination takes place via impurity traps or defect states within the energy bandgap of the semiconductor. The effect of SRH recombination on device performance can be minimized using float-zone (FZ) or high-quality Czochralski-grown (CZ) monocrystalline silicon.

As a result of these recombination mechanisms, the effective lifetime of the excess charge carriers reduces, which is a figure of merit to characterize the recombination in the device. Effective bulk lifetime (τ_{bulk}) is defined as

$$\frac{1}{\tau_{bulk}} = \frac{1}{\tau_{rad}} + \frac{1}{\tau_{Auger}} + \frac{1}{\tau_{SRH}} \tag{2.5}$$

in which the highest recombination rate limits the effective bulk lifetime. Besides recombination in bulk, the surface recombination should be taken into consideration so that the effective lifetime (τ_{eff}) becomes

$$\frac{1}{\tau_{eff}} = \frac{1}{\tau_{bulk}} + \frac{1}{\tau_{surface}} \tag{2.6}$$

Effective lifetime is defined as the average lifetime of the excess carriers before they recombine. It is a ratio of the excess charge carrier density Δn to the net recombination rate R, as shown by

$$\tau_{eff} = \frac{\Delta n}{R} \tag{2.7}$$

A deliberate optimization of emitter formation (i.e., doping profile, which determines excess carrier concentration) and surface passivation are required to achieve a high effective lifetime of the carriers, in turn, high open-circuit voltage (V_{oc}). Considering all these variables, solar cell fabrication should be optimized by maintaining a delicate balance. These parameters that are figures of merit for the solar cell efficiency, such as open-circuit potential, short-circuit current density, and

fill factor, are explained below. Solar cell characteristics of dark and illuminated current-voltage (I-V) are given in Figure 2.7.

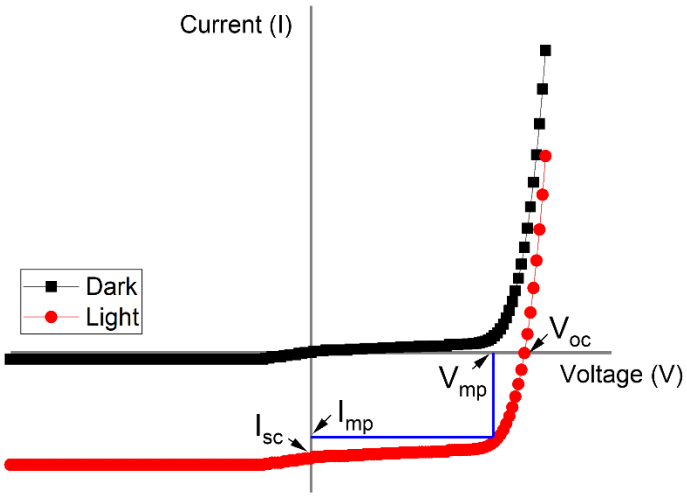

Figure 2.7 Current-voltage characteristics of a solar cell in the dark (black) and under illumination (red).

In an ideal case, the solar cell working mechanism is explained by the diode equation given as

$$I = I_0 \left[exp\left(\frac{qV}{nk_BT}\right) - 1 \right] - I_L \tag{2.8}$$

where I_0 is dark saturation current, q is the elementary (electronic) charge, V is the voltage across the solar cell, n is the ideality factor, k_B is Boltzmann's constant, T is the absolute measurement temperature, and I_L is light-generated current. However, the performance of the solar cell is affected by the electrical losses in the solar cell. When parasitic resistive losses are considered, they are modeled by the addition of series and shunt resistance (R_S and R_{SH}, respectively) into the equation. The equation for the first quadrant with the effect of series and shunt resistances is given by

$$I = I_L - I_0 exp\left[\frac{q(V + IR_S)}{nk_BT}\right] - \frac{V + IR_S}{R_{SH}} \tag{2.9}$$

Series resistance contribution arises from the base, emitter, front (finger and busbar), and rear metal contacts in the solar cell. On the other hand, shunt resistance creates an alternative path for the current flow.

The performance of the solar cells is mainly characterized by the current-voltage curve under illumination, where solar cell parameters are extracted from. Open-circuit voltage (V_{oc}) is the maximum voltage across the solar cell when the net current is zero. Short-circuit current (I_{sc}) is the maximum current passing through the solar cell when the voltage equals zero. The fill factor (FF) is directly proportional to the maximum achievable power and is defined as

$$FF = \frac{V_{MP} I_{MP}}{V_{oc} I_{sc}} \tag{2.10}$$

and a low FF value of a solar cell indicates the presence of parasitic resistive losses. V_{oc} is influenced by effective surface passivation. Last of all, power conversion efficiency (PCE) is the ratio of output power to the incident power from the sun, which is given as

$$\eta = \frac{V_{oc} I_{sc} FF}{P_{in}} \tag{2.11}$$

where P_{in} is incident power which depends on the photon flux of the solar spectrum. Solar cells are generally characterized for the air mass 1.5 global spectrum (AM1.5g) to extract solar cell parameters for a solar cell operation on the earth. The following references can be consulted for further in-depth theoretical knowledge of solar cell working mechanisms [15,16].

2.3 Silicon Surface Passivation

The recombination mechanisms mentioned in Section 2.2 should be suppressed in a solar cell to obtain a high-efficiency device. As radiative band-to-band recombination is an intrinsic process, extrinsic recombination routes, such as surface recombination and Auger recombination, should be minimized in the device to

maximize the effective lifetime of excess carriers. Although defect-related recombination in bulk can be negligible when a high-quality c-Si is used, defect recombination at the surface is one of the dominating mechanisms that cannot be ignored. In this context, providing surface passivation is one of the most critical aspects. Passivation schemes rely on two different mechanisms which suppress surface recombination. The first mechanism is the reduction of charge carrier concentration by the electric field. The second is the saturation of the dangling bonds leading to a reduction of the density of surface states. These two mechanisms correspond to field-effect passivation and chemical passivation, respectively.

- **The field-effect passivation:** It originated from the electric field created in the silicon so that photo-generated carriers are kept away from the recombination centers at the surface of silicon. Therefore, the concentration of free carriers is decreased at the surface. The built-in electric field is induced by the doped region in the silicon, or the fixed charge density provided by the dielectric passivation film deposited.
- **The chemical passivation:** Recombination centers due to imperfections of the silicon lattice (i.e., Si dangling bonds) are saturated by thin films deposited on the silicon surface. Therefore, chemical passivation is closely correlated with interface trap density.

Generally, dielectric layers which can provide both chemical and field-effect passivation are employed for the silicon surface passivation, such as silicon oxide (SiO_2), silicon nitride (SiN_x), titanium oxide (TiO_2), aluminum oxide (Al_2O_3), and the combination of these dielectric layers in the form of stacks. These are extensively used in photovoltaic and integrated circuit industries. A schematic illustration of a silicon-oxide interface and the associated charges are depicted in Figure 2.8. Mobile ionic charges (Q_m) arise from ionic impurities, such as sodium or potassium. Interface trapped charges (Q_{it}) are located at the interface which originate from the impurities, defects, and excess silicon or oxygen. Fixed oxide charges (Q_f) are directly related to the dielectric film deposited on the surface, which alter depending

on the thin film deposition technique and post-treatments, such as annealing. Oxide trapped charges (Q_{ot}) originate from the trapping of electrons or holes distributed inside the oxide. Total effective fixed charges (Q_{tot}) correspond to the effective charge arising from all these trapped charges (both oxide trapped charges and interface trapped charges).

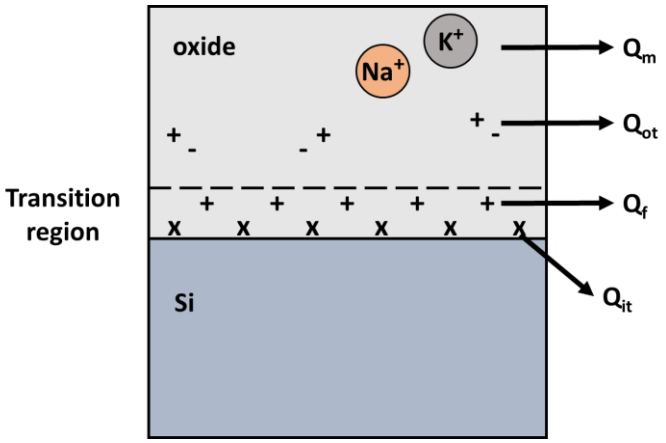

Figure 2.8 Schematic representation of silicon-oxide interface and the associated charges, redrawn from [15].

Al_2O_3 is an excellent material for c-Si surface passivation since it provides both field-effect passivation with the help of high negative fixed charge density and chemical passivation, especially after post-annealing processes. The superior passivation property of Al_2O_3 is demonstrated in Chapter 4.

2.4 Atomic Layer Deposition

Atomic layer deposition (ALD) is a thin film deposition technique based on a chemical vapor deposition (CVD) process. However, due to its self-terminating nature, ALD differs from other CVD processes, such as sputtering or plasma-enhanced chemical vapor deposition (PECVD). One of the main features of ALD distinguishing it from the CVD technique is that an ALD process is performed through sequential chemical reactions called “half-reactions”, which enables a

growth mechanism with an atomic layer precision [17]. A schematic illustration of an ALD cycle is shown in Figure 2.9. An ALD cycle consists of four process steps, the pulsed introduction of each precursor for the self-limiting half-reactions and the purging steps in between to remove by-products and unreacted precursors. Each pulse time is optimized to allow the precursor to react totally with the sites on the substrate. Purging with an inert carrier gas removes the reaction by-products and unreacted excess precursor. Therefore, purge time should also be optimized to avoid condensation of the precursor on the substrate. The resulting growth per cycle (GPC) is typically less than one Angstrom per cycle, depending on the deposited material. Therefore, this cycle is repeated until the desired film thickness is acquired.

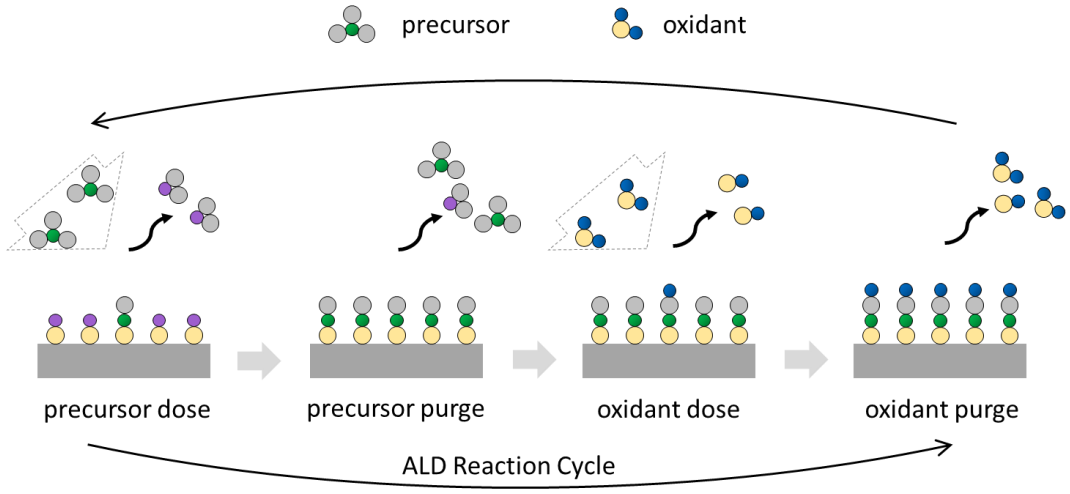

Figure 2.9 Schematic illustration of the ALD cycle and self-terminating surface reaction mechanism

The schematic representation of the ALD reactor and the ALD cycles for Al_2O_3 growth is shown in Figure 2.10. The reactions take place sequentially by introducing the pulsed precursors separated from each other by a carrier inert gas so that the deposition can be controlled at an even atomic size level which paves the way to deposit ultra-thin nanolayers. One of the most advantageous features of ALD is that the deposited layers are homogenous regardless of the surface geometry because of the self-limiting feature of the reactions that take place in an ALD process. To this

extent, it provides excellent conformal deposition on even very high aspect ratio structures (i.e., excellent step coverage). It is possible to control the thickness of the deposited film with perfect homogeneity all over the substrate. Moreover, ALD provides thin film deposition of various materials, including oxides, nitrides, and sulfides [18].

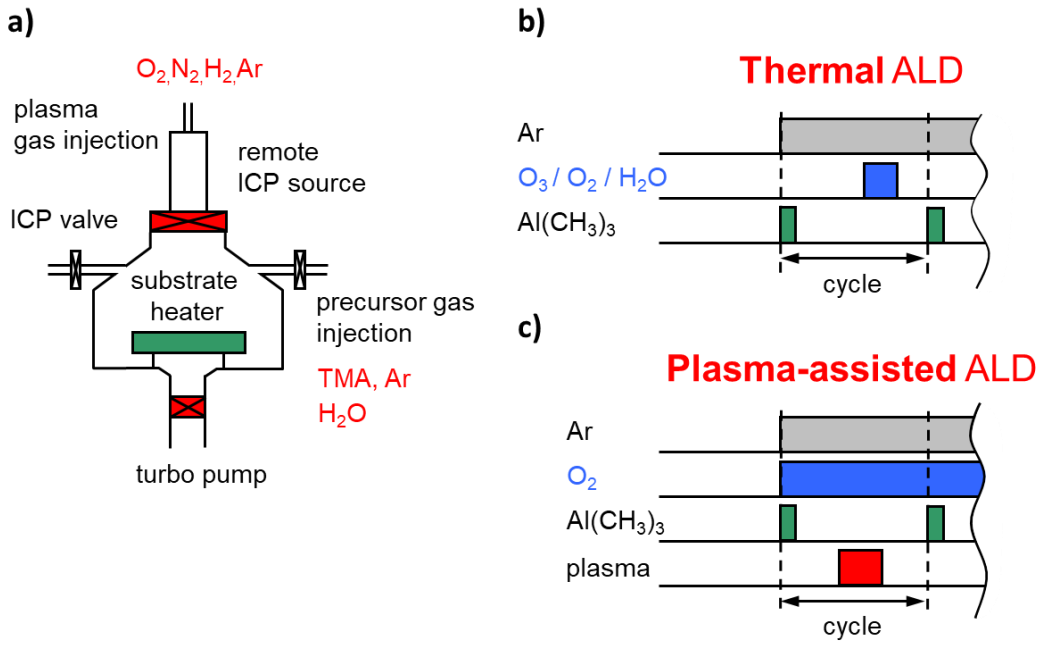

Figure 2.10 Schematic representation of a) ALD reactor b) ALD cycles of thermal ALD and c) plasma-assisted ALD for Al_2O_3 depositions, adapted from [19].

GPC as a function of deposition temperature is shown in Figure 2.11. Moreover, the growth mechanisms and their effects on growth behavior are also demonstrated. In an ideal ALD process, the self-limiting growth regime occurs in the ALD window resulting in monolayer deposition. Therefore, deposition temperature should be optimized for the reaction to take place in the ALD window for each deposited material.

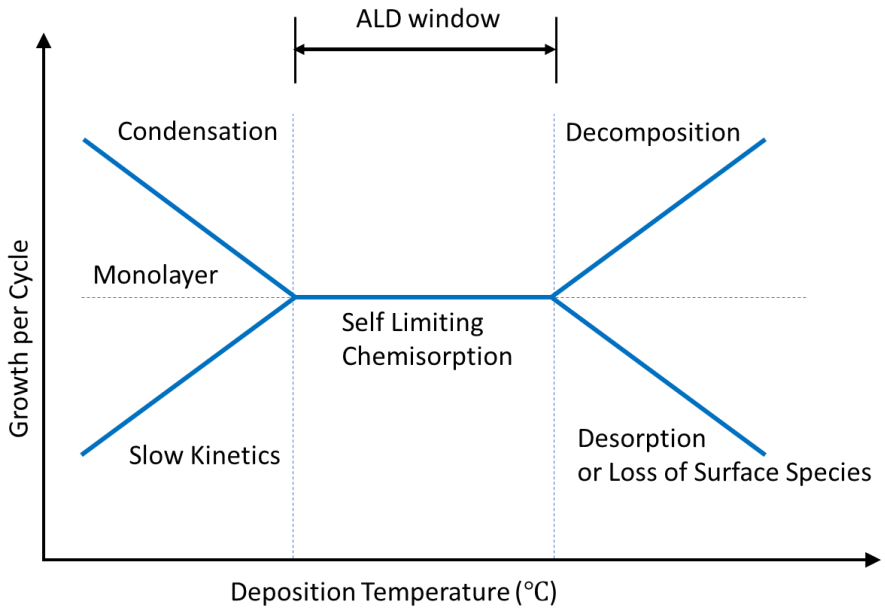

Figure 2.11 Growth per cycle as a function of deposition temperature and the corresponding growth mechanisms.

2.5 Charge Transport Mechanism in Solar Cells

The photogenerated electron-hole pairs are separated and collected by the external electrodes to attain electrical energy. Two forces determine the flow of the charge carriers in a solar cell, which results in either diffusion current or drift current. While diffusion current is driven by the inhomogeneous carrier densities in p-type and n-type regions, drift current results from the electric field. These two opposing forces determine electron current density (J_n) and hole current density (J_p), which are given in one dimension as

$$J_n = +qD_n \frac{dn}{dx} - q\mu_n n \frac{d\varphi}{dx} = \frac{\sigma_n}{q} \frac{dE_{Fn}}{dx} \tag{2.12}$$

$$J_p = -qD_p \frac{dp}{dx} - q\mu_p \mathrm{p} \frac{d\varphi}{dx} = \frac{\sigma_p}{q} \frac{dE_{Fp}}{dx} \tag{2.13}$$

where D_n and D_p are diffusion coefficients for the electrons and holes, respectively, n and p are electron and hole concentrations, respectively, μ_n and μ_p denote the electron and hole mobility, respectively. Total charge current density can be found by summation of the electron and hole current density. The relationship between the electron and hole conductivities and corresponding mobilities are defined as

$$\sigma_n = q\mu_n n \tag{2.14}$$

$$\sigma_p = q\mu_p p \tag{2.15}$$

Therefore, selective charge carrier extraction in a solar cell can be achieved if there is a significant difference in electron and hole conductivities. Electron and/or hole selective contacts are established by altering charge carrier concentration near the surface. There are three distinct methods to accomplish this goal. These methods are doping, depositing materials with fixed charges, and using materials with low or high work functions for electron and hole selective contacts, respectively.

Charge selectivity of a contact can be analyzed by contact resistivity measurement, which is further explained in Section 3.2.

CHAPTER 3

CHARACTERIZATION METHODS

3.1 Reflectance and Transmittance Measurements

The reflectance and transmittance measurements can determine the optical properties of a sample or a thin film (i.e., c-Si wafer, thin films, etc.). The total reflectance and total transmittance of the sample can be measured with the help of an integrating sphere coupled to the spectrometer. A schematic illustration of the integrating sphere and the reflectance measurement is shown in Figure 3.1. An integrating sphere is a spherical cavity with an interior surface coated with a diffuse reflective layer. It is generally coated with barium sulfate (BaSO4), and the measurements are carried out with the assumption that the interior of the integrating sphere has 100% reflectivity. Wavelength-dependent reflectance or transmittance is measured after multiple reflections in the integrating sphere. Since the light incident on a sample is reflected both specularly and diffusely, the sample is illuminated with an angle of incidence. Specular and diffuse components of the reflected/transmitted light can be determined individually with an absorber component attached at an angle of the specular reflection/transmission, as shown in Figure 3.1b. Wavelength-dependent optical characterization is performed with the help of a spectrometer and incident monochromatic light.

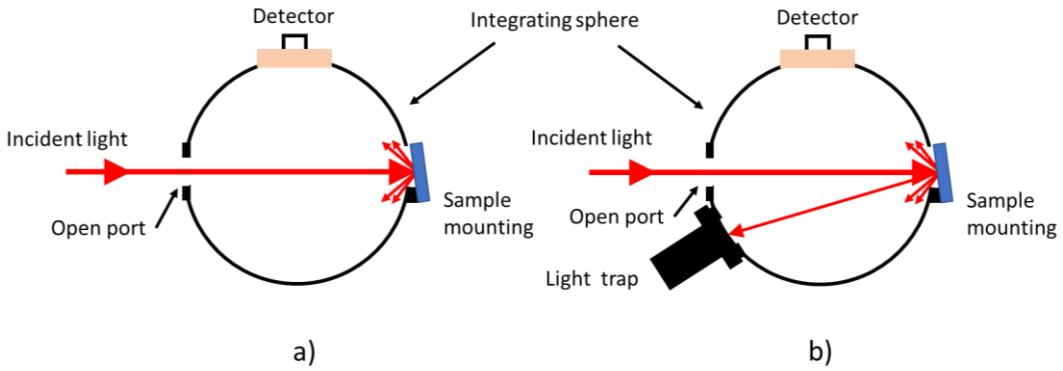

Figure 3.1 Schematic representation of integrating sphere demonstrating a) total reflectance and b) diffuse reflectance measurements, redrawn from [20].

Once spectral data is obtained, the total weighted average reflectance R_w can be calculated by integrating the total reflectance (typically in a wavelength range of 350-1100 nm for silicon) under AM1.5g solar spectrum conditions with an integrated power of 1000 W/m^2. The definition of R_w is as follows:

$$R_w = \frac{\int_{350nm}^{1100nm} R(\lambda)N(\lambda)d\lambda}{\int_{350nm}^{1100nm} N(\lambda)d\lambda} \tag{3.1}$$

where $R(\lambda)$ and $N(\lambda)$ are total reflectance as a function of wavelength and solar spectral irradiance under AM1.5g standard conditions, respectively.

Reflectance haze is a figure of merit for the optical characterization of the samples. It is defined as the ratio of the diffuse reflectance to the total reflectance. An increased haze of a sample accounts for the enhanced scattering and effective light coupling in the sample.

Optical measurements (total and diffuse spectrophotometric measurements of reflectance and transmittance) were carried out by Bentham Instruments PVE300 tool with DTR6 integrating sphere mounted to the system throughout the study.

3.2 Contact Resistance Measurement

Contact resistivity is a crucial figure of merit in analyzing the Ohmic behavior of metal-semiconductor contacts and determining the series resistance losses within a solar cell. There are several methods to extract contact resistivity from the contact resistance measurement, two of which are used in this study. The first one depends on a two-terminal dark I-V measurement, as depicted in Figure 3.2. When an Ohmic structure is constituted, the contact resistance of interest can be found from the linear I-V curve. Specific contact resistance R_C is extracted from the slope of the I-V curve by a linear regression at zero voltage as follows:

$$R_C = \left\{\frac{\partial I}{\partial V}\right\}_{V=0} \tag{3.2}$$

If the contribution of each contact is known, the contact resistivity of an electrode-semiconductor interface can be calculated. This method is adapted for the characterization of organic self-assembled charge selective contacts capped by different electrodes presented in Chapter 6.

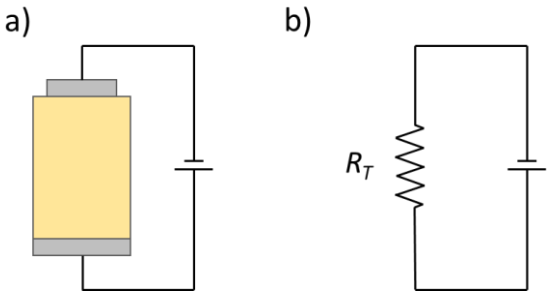

Figure 3.2 Two-terminal dark I-V measurement and corresponding equivalent circuit for the contact resistivity calculation.

The second approach to extract the contact resistivity is the transfer length method (TLM) by using a 4-terminal I-V measurement. A typical TLM test structure consists of parallel contacts of equal width but varied distances between them, as the schematic representation is shown in Figure 3.3. Unlike the previous method, the

TLM method does not require an Ohmic contact and metal electrodes at the rear side of the sample.

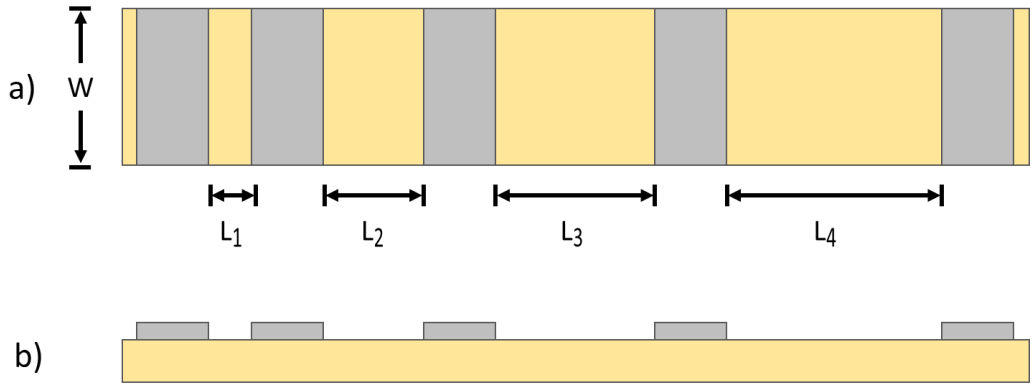

Figure 3.3 Schematic representation of TLM test structure a) top view b) cross-sectional view.

Assuming homogeneous sheet resistance throughout the entire layer, the resistance between two neighboring contacts ($R_{1,2}$) is calculated with a distance between them L_1 as follows

$$R_{1,2} = 2 \times R_C + R_{sheet}\left(\frac{L_1}{W}\right) \tag{3.3}$$

where R_C is the contact resistance, and W is the width of the contacts. Sheet resistance R_{sheet} and R_C are calculated by linear regression of the measured resistance as a function of the distance between the contacts. While the slope of the line gives R_{sheet}, R_C is found at the axis intercept by the numerical solution of the following equation:

$$R_C = \frac{\rho_C}{W\ L_T}\ \coth\frac{W_F}{L_T} \tag{3.4}$$

with the finger width W_F and transfer length defined as $L_T = \sqrt{\rho_C / R_{sheet}}$. These extracted values are shown in the measured resistance as a function of the distance graph given in Figure 3.4.

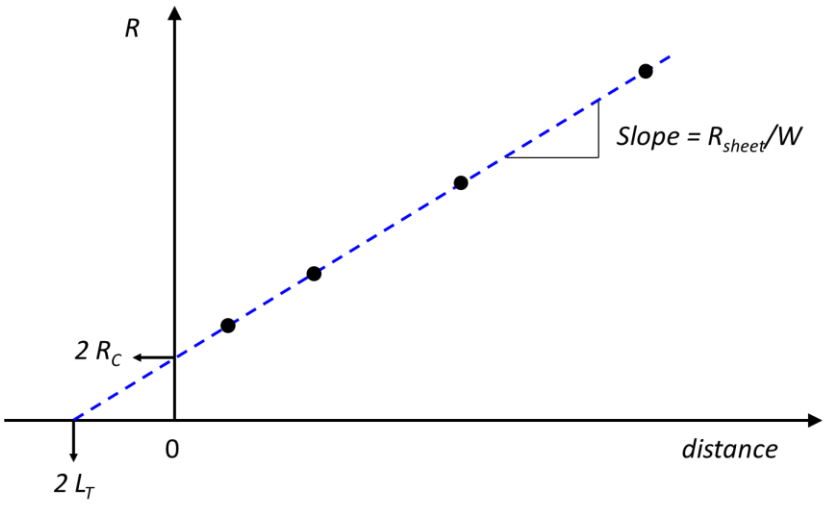

Figure 3.4 The measured resistance as a function of distance *L*

Contact resistance analysis is also possible on a solar cell stripe with equally spaced fingers. In this case, the resistance between non-neighboring fingers is measured. Moreover, the current partially flowing between the adjacent fingers instead of the emitter should be taken into consideration. Therefore, the resistance contribution from the intermediate fingers becomes

$$R_{int} = \frac{R_{sheet}}{W}\ 2L_T\ \tanh\frac{W_F}{2L_T} \tag{3.5}$$

The resistance is given as

$$R\ =\ 2R_C + \frac{R_{sheet}}{W}\left[(n+1)L + n\ d_{eff}\right] \tag{3.6}$$

where L is the distance between the fingers, n is the number of intermediate fingers, and d_{eff} is the effective width, a term defined to account for the current flowing through the intermediate fingers. Effective width d_{eff} is found by an iteration that ranges between values of W_F and $2 \times L_T$.

3.3 Quasi-Steady-State Photoconductance Measurement

The photoconductance decay (PCD) method is a versatile and contactless measurement technique to characterize the surface passivation properties by measuring the decay of the incident light and the change in the photoconductance of the sample in time [21]. The excess photoconductance σ_L is measured by the RF coil in the tool under illumination, which is defined as follows:

$$\sigma_L = q\Delta n_{av}(\mu_n + \mu_p)W \tag{3.7}$$

where Δn_{av} is the average excess minority carrier density, W is the thickness of the sample, μ_n and μ_p are electron and hole mobilities, respectively. Once the charge mobilities in the semiconductor, depending on the doping density and the injection level, are known, excess carrier density can be found iteratively. Interface passivation quality of the samples can be analyzed by determining the effective minority carrier lifetime τ_{eff} on symmetrically fabricated samples as follows:

$$\tau_{eff} = \frac{\sigma_L}{J_{ph}(\mu_n + \mu_p)} \tag{3.8}$$

where J_{ph} is the photogenerated current density. Moreover, implied open-circuit voltage iV_{oc} at 1-sun illumination can be calculated from the quasi-steady-state photoconductance measurement by using the relation given as

$$iV_{oc} = \frac{k_B T}{q} \ln\left(\frac{\Delta n(\Delta n + N_{A,D})}{{n_i}^2}\right) \tag{3.9}$$

where $N_{A,D}$ is the dopant density and n_i is the intrinsic carrier concentration.

3.4 Fourier Transform Infrared Spectroscopy

Fourier transform infrared (FTIR) spectroscopy is a powerful and reliable technique to identify and quantify a large variety of substances, from solids to liquids. Fingerprints of specific binding structures and the composition of the material are identified by measuring transmitted infrared (IR) radiation and analyzing their

vibrational modes. The fingerprint of each atomic bond vibration is specified to investigate chemical bonds in the material. FTIR is advantageous over other dispersive spectroscopy methods as all wavelengths are measured simultaneously, providing high-speed scanning with enhanced sensitivity. Fourier transform is utilized to convert the time domain to the frequency domain. Attenuated total reflection (ATR) accessorize is utilized for the characterization of thinner films. By means of the evanescent wave only a few microns beyond the ATR diamond crystal, change in totally internally reflected beam is measured with direct contact of diamond crystal with the sample.

3.5 X-Ray Photoelectron Spectroscopy

X-ray photoelectron spectroscopy (XPS) is a surface-sensitive characterization technique for quantitative elemental analysis of materials. It is based on the principle that chemical shift in the core-level binding energies of atoms takes place when the atoms are bonded to various elements. Core-level electrons are excited by the X-ray irradiation with known energy ($h\upsilon$). The binding energy (E_{be}) of the core-electron can be determined by measuring the kinetic energy of the ejected photoelectrons (E_{ke}). For that purpose, counts per second (CPS) is measured as a function of the kinetic energy of the emitted electrons.

$$E_{ke} = h\upsilon - E_{be} \tag{3.10}$$

Binding energy which is determined from this relation is specific to the element, if the orbital in question is a core-electron and the shift in a core level is attributed to the variations in valance levels due to the bonding with other atoms, hence the chemistry of the material surface. Normalized peak intensities are used to determine the elemental composition of the material and the corresponding atomic %. Background subtraction is carried out to eliminate the contribution of inelastic electron scattering. It provides chemical state analysis and molecular composition determination from the ratio of the relevant peak intensities. The atomic ratio is given in %.

CHAPTER 4

CRYSTALLINE SILICON SURFACE PASSIVATION FOR PERC SILICON SOLAR CELL APPLICATIONS

Aluminum oxide (Al_2O_3) is of interest due to its excellent surface passivation quality on both p-type and n-type silicon, providing both chemical passivation and field-effect passivation. Moreover, Al_2O_3 has no absorption in the wavelength range where solar cell operation is relevant. These properties make Al_2O_3 attractive for silicon solar cell applications. The key to high-efficiency c-Si solar cell manufacturing is the efficient passivation of c-Si surfaces. Thermal and plasma-enhanced ALD Al_2O_3 has been used extensively due to its excellent passivation performance on c-Si. Al_2O_3 films are generally capped with silicon nitride (SiN_x) layers, which is the mainstream for passivated emitter and rear cell (PERC) applications. However, Al_2O_3/SiN_x stacks are prone to blister formation, which deteriorates the surface passivation quality, when subjected to thermal treatments at high temperatures (e.g., firing), which is essential for contact formation of screen-printed metals in industrial silicon solar cell production [22-24]. Therefore, the application of ALD Al_2O_3 on c-Si solar cells becomes challenging. An additional out-gassing step, which is found to be beneficial in avoiding blister formation, is generally applied after H_2O-based thermal ALD Al_2O_3, prior to any capping layer deposition [25]. In this study, we show that blister-free films with efficient passivation quality can be obtained by careful control of ozone-based Al_2O_3 deposition without the necessity of an additional out-gassing step.

Thermal ALD Al_2O_3 based on trimethylaluminum (TMA, $Al(CH_3)_3$) and water (H_2O) has been a benchmark for a while for effective surface passivation of c-Si in solar cell production. However, ozone-based ALD Al_2O_3 is stated to have lower interface defect density (D_{it}) and higher fixed negative charge density (Q_f), resulting

in better surface passivation compared to H_2O-based ALD Al_2O_3 [26,27]. Ozone-based ALD processes are also reported to result in lower carbon contamination compared with those deposited with H_2O-based ALD [28]. In this study, we investigate the effect of ozone concentration and deposition temperature on passivation quality and stability (blistering) of Al_2O_3 films and Al_2O_3/SiN_x stacks with a broad range of post-deposition thermal treatments. In particular, the effect of ozone concentration on the passivation properties of Al_2O_3 films and industrial-relevant Al_2O_3/SiN_x stacks are shown. This study on ozone-based ALD Al_2O_3 can be an industrial roadmap for simplified fabrication of blister-free rear-side passivation of PERC solar cells without requiring an extra out-gassing step.

The results and findings discussed in this chapter are based on studies conducted at Fraunhofer ISE in Germany. Passivation properties of thermal and plasma-assisted ALD Al_2O_3 are investigated in Section 4.1. The effect of the oxidizing agent on the passivation mechanism is examined in terms of c-Si/Al_2O_3 interface properties, passivation qualities, and thermal stabilities with varied post-annealing treatments. In Section 4.2, ozone concentration-dependent thermal-ALD Al_2O_3 deposition is optimized. Then, optimized layers are adopted to investigate the feasibility of ozone-based thermal ALD Al_2O_3 as a passivation layer at the rear side of PERC solar cells in Section 4.3.

4.1 Silicon Surface Passivation via ALD Al_2O_3: Effect of Oxidant Precursor on Silicon Passivation Quality

4.1.1 Experimental Details

ALD Al_2O_3 films were deposited on both n-type and p-type c-Si with varied thicknesses from 0.1 nm to 10 nm. Symmetrical passivation samples were fabricated on shiny-etched float-zone (FZ) mono c-Si wafers with a resistivity of 1 Ω.cm, and a thickness of 200 μm and 250 μm for n-type and p-type wafers, respectively. FZ wafers were used to suppress trap-assisted recombination in bulk.

Samples were subjected to cleaning with nitric acid HNO_3, and thermal oxidation at 1050 °C to remove FZ defects [29]. The oxide was removed by hydrofluoric acid (HF) (1% wt.) dip prior to ALD Al_2O_3 depositions. Al_2O_3 depositions were carried out by Oxford Instruments FlexAL, which enables both plasma-assisted ALD and thermal-ALD deposition techniques. Trimethylaluminum (Al_2Me_6 or TMA) was used as the aluminum precursor. Argon (Ar) was used as the carrier and purge gas in the processes. Varied deposition techniques and oxidant precursors were used to investigate the effects of these variables on the c-Si surface passivation. Oxidant precursors were either water vapor (H_2O) or ozone (O_3) for thermal-ALD processes and oxygen (O_2) for plasma-assisted ALD processes. Thermal-ALD processes using water vapor or ozone as the oxidizing agent are denoted as thermal H_2O and thermal O_3, respectively. The plasma-ALD process with oxygen precursor is denoted as plasma O_2 hereafter. Ozone was generated by Absolute Ozone® Generators Atlas 30, assembled to the ALD tool. Ozone concentration was expected to be 12.5 % wt. (187 g/Nm^3) for oxygen flow of 1 standard liter per minute (SLM) [30]. However, this ozone concentration value is valid for oxygen flow with nitrogen addition (of around 8-10 %) which is utilized to improve the ozone generation. Since pure oxygen was used for ozone production by Atlas 30 ozone generator, the resulting ozone concentration was expected to be lower than 12.5% wt. with an oxygen flow of 1 SLM. The ozone concentration-dependent ALD Al_2O_3 growth mechanism is demonstrated in Section 4.2 by using MKS Instruments O3CS AX8561 ozone system. GPC results for both ozone generator are compared in Figure 4.5 which is an indirect indication of the ozone concentration fabricated by using Atlas 30 generator to be between 5-20% wt..

The rear sides of the c-Si wafers were deposited with the plasma-assisted ALD Al_2O_3 layers with a fixed film thickness of 15 nm, while the front sides of the c-Si wafers were deposited with three different ALD processes with varied Al_2O_3 target thicknesses from 0.1 nm to 10 nm. Sequential forming gas annealing (FGA) in 50 °C increments was carried out for 5 minutes at temperatures varied from 300 °C to 550 °C in a tube furnace for the activation of passivating Al_2O_3 layers. Passivation

qualities of deposited ALD Al_2O_3 films (both in an as-deposited state and after each sequential annealing step) were investigated with effective minority carrier lifetime measurements using Sinton WTC-120 photoconductance lifetime tester. The thickness of deposited Al_2O_3 layers was measured by J.A. Woollam Spectroscopic Ellipsometry (SE) at an incident angle of 70°, and growth per cycle was calculated for each deposition. SE measurements were fit using Cauchy optical model for Al_2O_3 films. SE measurements were carried out for both as-deposited Al_2O_3 films and after the final FGA at 550 ℃ to observe whether FGA affects the thickness of the Al_2O_3 layers.

4.1.2 Results and Discussion

Measured thicknesses of ALD Al_2O_3 deposited samples which were carried out after ALD depositions (as-deposited) and FGA at 550 ℃, are shown in Figure 4.1. The GPC for each ALD technique is calculated as 0.115 nm/cycle, 0.084 nm/cycle, and 0.073 nm/cycle for plasma O_2, thermal H_2O, and thermal O_3 processes, respectively. Al_2O_3 films thinner than 2 nm are nominal thicknesses calculated from GPC varying between 0.073-0.115 nm/cycle depending on oxidant precursor type. The thickness of the Al_2O_3 films directly after the ALD growth and after the FGA at 550 ℃ are shown by closed and open symbols respectively. No significant thickness variation is observed after the FGA at 550 ℃ compared to the thickness of the samples in the as-deposited state. Moreover, growth delay is observed in the first atomic layers of the ALD processes due to the substrate-inhibited growth behavior. Moreover, a slight increment of thickness is observed after FGA treatment which could be an indication of SiO_2 interlayer formation after the thermal process.

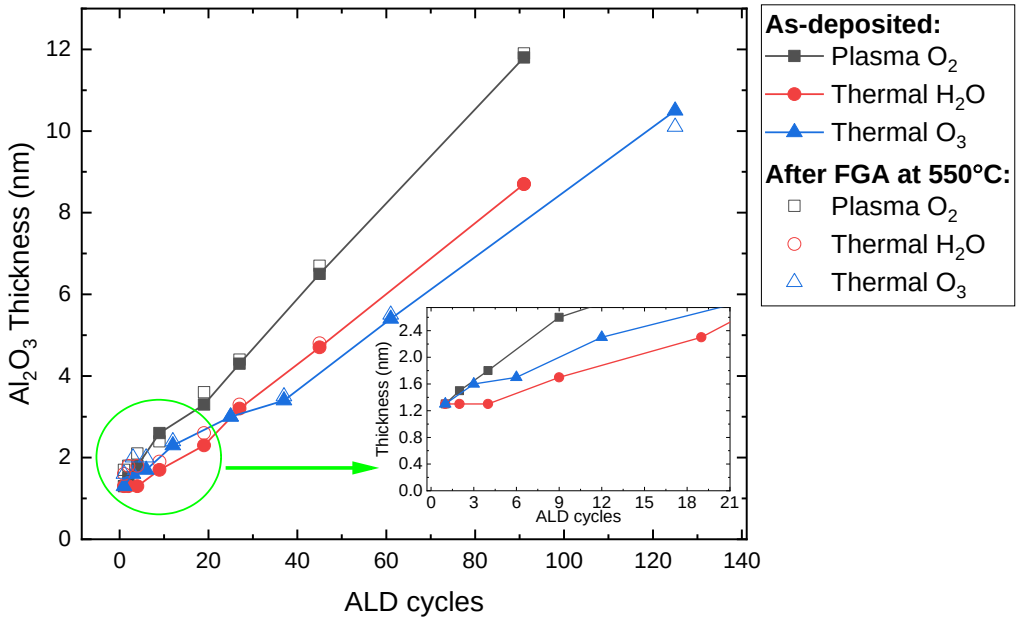

Figure 4.1 Spectroscopic ellipsometry measurement results for varied ALD cycles. Inset shows implication of interfacial silicon oxide formation and initial growth delay.

PCD measurements are carried out after each consecutive annealing step for Al_2O_3 depositions with varied oxidant precursors and film thicknesses. Injection-dependent effective minority carrier lifetimes of 10 nm thick plasma O_2 ALD Al_2O_3 deposited n-type c-Si sample in the as-deposited state and after FGA at temperatures between 300 ℃ and 500 ℃ are shown in Figure 4.2. Effective lifetime τ_{eff} increment is observed when Al_2O_3 thickness increases, as expected. Moreover, effective lifetime τ_{eff} increases with the elevated FGA temperatures, as activation of ALD Al_2O_3 is required.

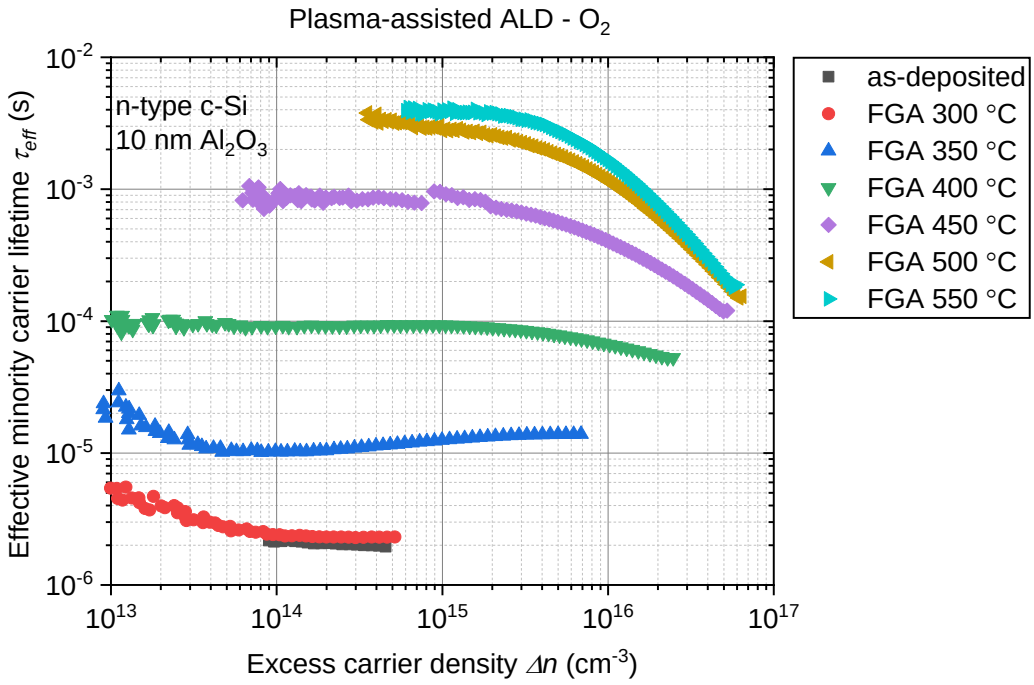

Figure 4.2 Injection-dependent effective minority carrier lifetime τ_{eff} of 10 nm thick plasma-assisted ALD Al_2O_3 deposited n-type c-Si sample for varied FGA temperatures.

Effective lifetimes τ_{eff} at an injection level of $\Delta n = 1 \times 10^{15}\ cm^{-3}$ are compared for each deposition technique, Al_2O_3 thickness, and consecutive FGA temperature in Figure 4.3. First, when optimized ALD process parameters are adopted, surface passivation via ALD Al_2O_3 film is achieved for both p-type and n-type c-Si regardless of oxidant precursor type. This is achieved due to superior Al_2O_3 film properties, providing field-effect passivation and chemical passivation simultaneously due to having a high fixed charge density and moderate D_{it} level [31,32]. Effective lifetime τ_{eff} results of samples with thinner Al_2O_3 film after annealing at 450 °C are slightly lower because of the measurement inaccuracy. Na. ox. represents the reference sample with plasma-assisted ALD Al_2O_3 film at the rear side of the n-type c-Si, while there was no Al_2O_3 film but a layer of native oxide (na. ox.) at the front side of the sample. Therefore, the performance of various Al_2O_3 films utilized on the front side of c-Si samples is indirectly measured and confirmed

compared to the native oxide (SiO_2) formed under ambient air conditions. Although optimum annealing temperature for the activation of ALD grown Al_2O_3 layers is reported to be between 400 ℃ and 450 ℃ in literature, effective lifetime τ_{eff} increment even for the annealing temperature at 500 ℃ is observed for both n-type and p-type c-Si samples [33]. This trend is valid for all ALD processes with varied oxidant precursors. While FGA at 500 ℃ results in maximum effective lifetime τ_{eff} for the Al_2O_3 passivation layers on p-type c-Si, effective lifetime τ_{eff} even increases at an annealing temperature of 550 ℃ for Al_2O_3 passivation films on n-type c-Si. These results imply that typical activation of Al_2O_3 by the FGA process at a temperature of around 425 ℃ could result in underperformed effective lifetime results than a probable achievable effective lifetime by utilizing Al_2O_3. If passivation qualities of the samples deposited with various oxidants are compared, effective lifetimes τ_{eff} of 1.5 ms, 1.4 ms, and 625 µs are obtained on p-type c-Si via thermal H_2O, plasma O_2, and thermal O_3, respectively. Underperforming thermal O_3 Al_2O_3 films might originate from unknown ozone concentration that might alter during the depositions. Underperformed thermal O_3 Al_2O_3 is further improved by using variable ozone concentration in Section 4.2. Still, thermal O_3 Al_2O_3 films provide decent passivation with iV_{oc} values above 700 mV at 1-sun illumination.

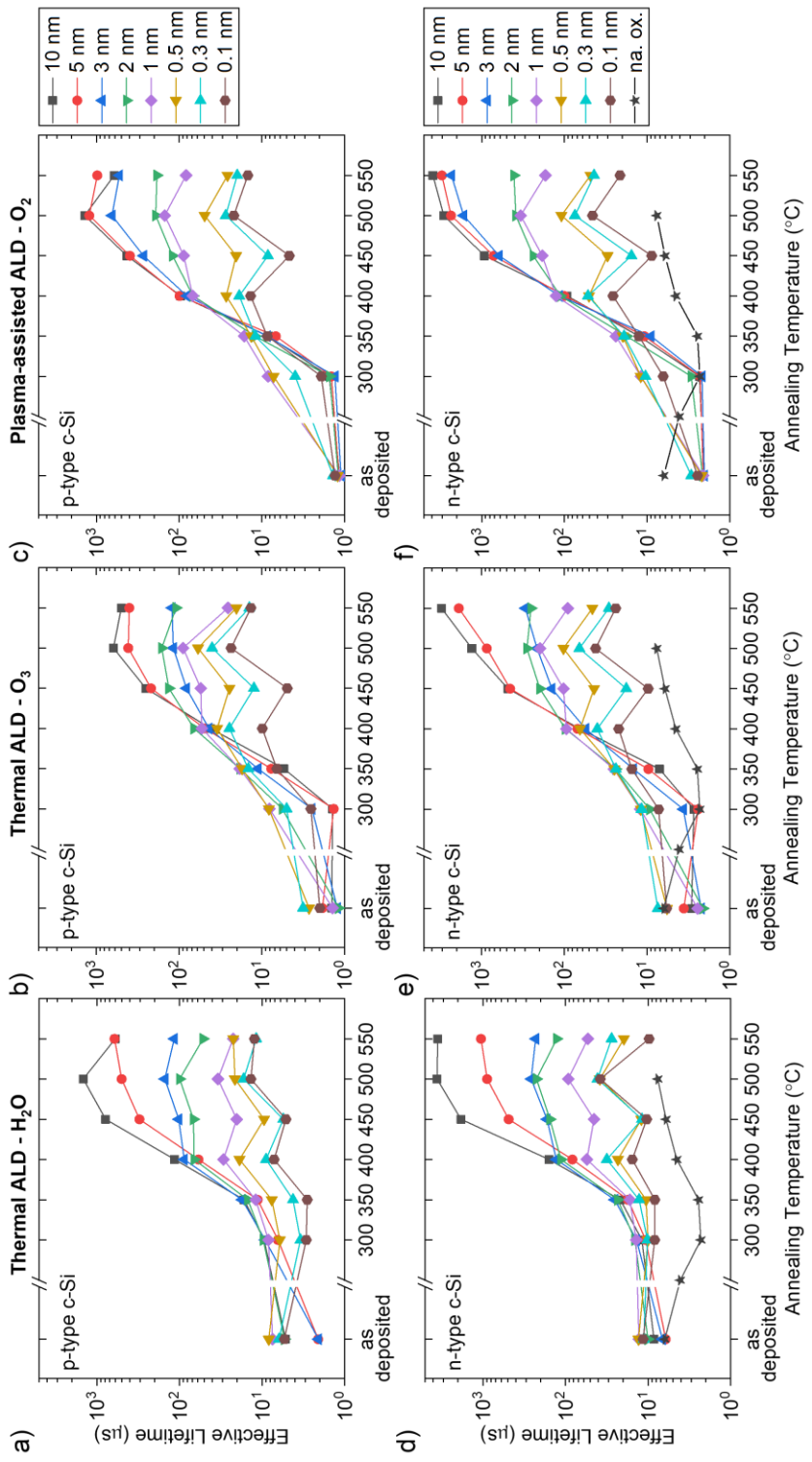

Figure 4.3 Comparison of effective minority carrier lifetimes of Al_2O_3 deposited samples for varied Al_2O_3 thickness and FGA temperature on p-type (top row) and n-type (bottom row) c-Si samples.

Implied open-circuit voltage iV_{oc} values of the samples at 1-sun illumination after each consecutive annealing step are extracted from PCD measurements. Extracted iV_{oc} of the samples with varied Al_2O_3 thickness and ALD deposition technique after FGA at 500 °C and 550 °C are shown in Figure 4.4. iV_{oc} of samples exhibits the same characteristics as effective lifetime results shown in Figure 4.3 (i.e., better surface passivation as the FGA temperature and Al_2O_3 film thickness increase). The effects of deposition technique and FGA temperature are more pronounced for thinner Al_2O_3 films. The thinner Al_2O_3 films and lower FGA temperatures result in insufficient surface passivation, as indicated by low iV_{oc} values (below 600 mV). However, Al_2O_3 films thicker than 5 nm enable iV_{oc} exceeding 700 mV independent of the deposition technique and the oxidant precursor. Superior surface passivation with the maximum implied open-circuit voltage iV_{oc} of 732 mV and 725 mV is achieved with thermal H_2O process on n-type and p-type c-Si, respectively.

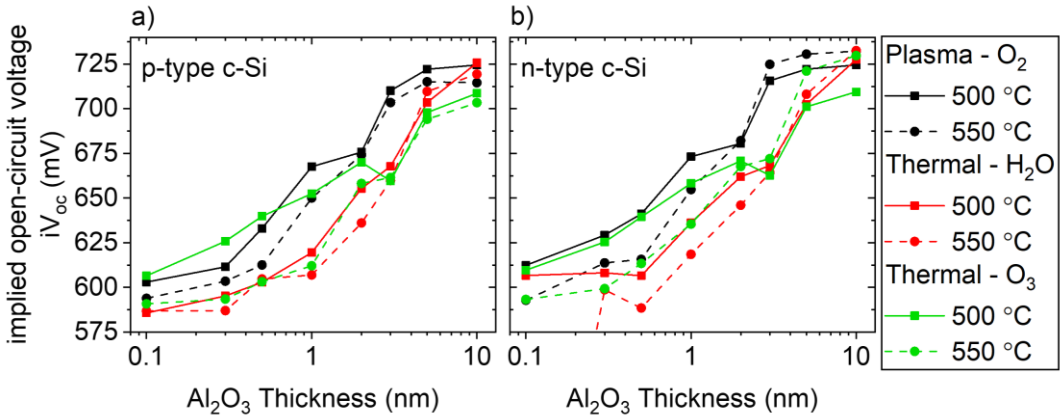

Figure 4.4 Implied open-circuit voltage values at 1-sun illumination extracted from PCD measurements for a) p-type c-Si and b) n-type c-Si samples passivated by varied ALD Al_2O_3 films after FGA at 500 °C and 550 °C.

4.1.3 Conclusion

The influence of oxidant precursor type on the silicon surface passivation quality is demonstrated with varied post-annealing treatments. If passivation qualities of the

samples deposited with various oxidants are compared, effective lifetimes τ_{eff} of 1.5 ms, 1.4 ms, and 625 μs are obtained on p-type c-Si via thermal H_2O, plasma O_2, and thermal O_3 ALD processes, respectively. After thermal treatments, effective lifetimes τ_{eff} of 3.6 ms, 3.9 ms, and 3.1 ms are achieved on n-type c-Si by thermal H_2O, plasma O_2, and thermal O_3 ALD processes, respectively. A good level of surface passivation is obtained with all oxidant precursors with implied open-circuit voltages exceeding 700 mV.

4.2 C-Si Surface Passivation via Ozone-Based Thermal-ALD Al_2O_3

4.2.1 Experimental Details

Ozone-based thermal-ALD Al_2O_3 films were deposited on shiny-etched float-zone (FZ) c-Si wafers. C-Si wafers were subjected to HNO_3 cleaning before ALD depositions. Trimethylaluminum ($Al(CH_3)_3$ or TMA) precursor was used as an Al source. TMA dose and purge times were kept constant, which were 20 ms and 2 s, respectively. On the other hand, ozone dose and ozone purge times were varied for different ozone concentrations. Ozone was generated via MKS Instruments O3CS AX8561 ozone system coupled to FlexAl ALD tool, and ozone concentration in ALD cycles was tuned from 5% wt. (73 g/Nm^3) to 20% wt. (306 g/Nm^3) (minimum and maximum limits of the ozone generator). Oxygen flow was adjusted between 2.5 - 8 SLM to obtain the targeted ozone concentration. Deposition temperature varied from 100 °C to 300 °C, all remaining within the ALD window for thermal ozone-based ALD Al_2O_3 depositions. Al_2O_3 growth and the film uniformity were analyzed by spectroscopic ellipsometry measurements at an angle of 70°, and growth per ALD cycle was calculated for each varied process parameter. The structural analysis of ozone-based ALD Al_2O_3 samples was carried out by FTIR analysis. FTIR data were acquired by Bruker VERTEX 80v spectrometer with attenuated total reflectance (ATR) accessory attached to the instrument.

4.2.2 Results and Discussion

Optimization of the thermal-ALD Al_2O_3 process is carried out by utilizing varied O_3 dose and purge times depending on O_3 concentration. The influence of O_3 purge time on Al_2O_3 growth investigated for various O_3 dose time and O_3 concentration is shown in Figure 4.5. It is observed that GPC saturates for the purge times longer than 15 s. On the other hand, uncontrolled growth is observed for shorter purge times, which results in condensation of the precursor on the surface of the substrate. It is shown that O_3 concentration has a significant impact on GPC, resulting in up to 60% higher GPC for higher O_3 concentration (20% wt.). Besides, O_3 dose time is observed to have less influence on GPC. 5% to 10 % higher GPC is obtained with an O_3 dose time of 125 ms, compared to a shorter O_3 dose time (50 ms). Comparing the effect of ozone concentration on GPC, the ozone concentration of the former ozone generator (Atlas 30) is estimated to be between 10-20% wt., which is shown by star symbols with unknown ozone concentration (unk.% wt.).

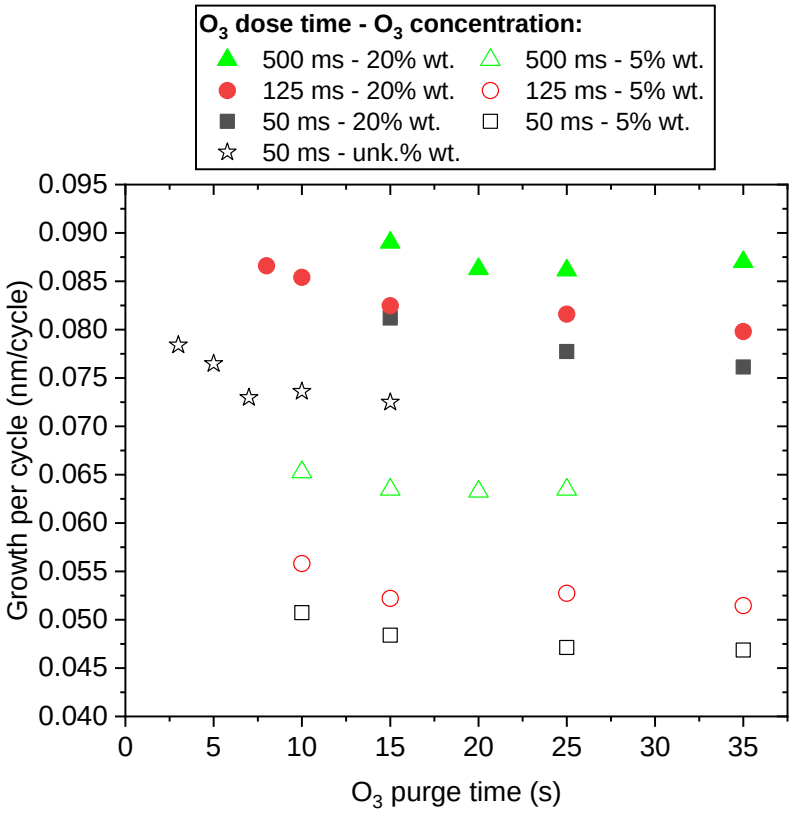

Figure 4.5 Growth per ALD cycle of Al_2O_3 films depending on O_3 purge time for varied O_3 dose times and O_3 concentrations.

Variation of growth per ALD cycle depending on ozone concentration is shown in Figure 4.6. All processes were carried out at a deposition temperature T_{Dep} of 200 °C with an ozone purge time of 30 s to ensure Al_2O_3 growth in the ALD window and to have complete saturation on the c-Si surface for different ozone concentrations. GPC varies in the range of 0.46-0.83 Å/cycle for different O_3 concentrations and O_3 dose times. A linear increase in GPC is observed with increasing O_3 concentration. The dashed line is a guide for the eye to indicate the linear increase with respect to O_3 concentration.

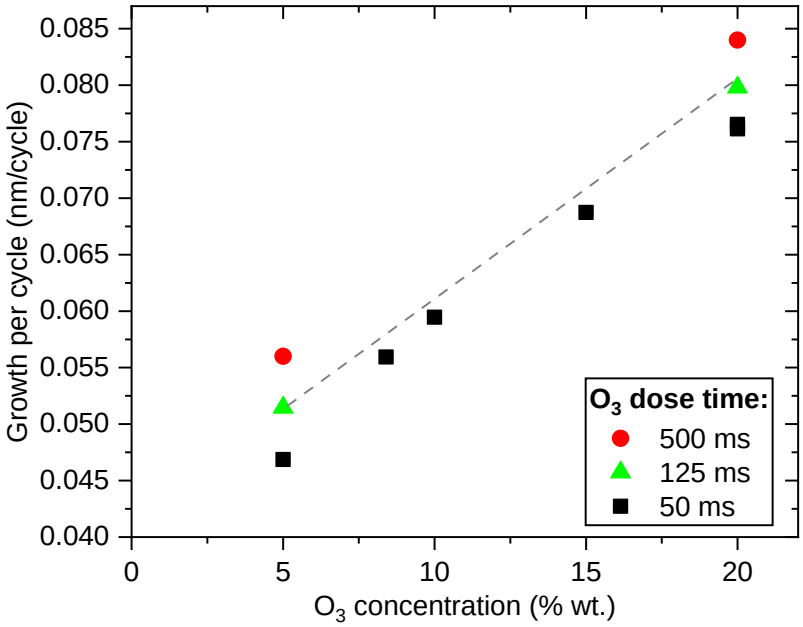

Figure 4.6 Growth per ALD cycle of Al_2O_3 films depending on O_3 concentration and O_3 dose time.

If the precursor purge time is sufficiently long, GPC saturation is expected to be observed for ALD growth with increased precursor dose time. Since optimum dose and purge times of TMA are known from the previous study [34], GPC saturation is ensured by altering the dose and purge time of O_3 dose time for a fixed O_3 concentration of 20% wt.. Variation of GPC depending on O_3 dose time for various O_3 purge times and depositions with an O_3 concentration of 20% wt. is shown in Figure 4.7. It can be concluded that the O_3 dose time of 500 ms ensures the complete surface reaction (i.e., self-limiting, irreversible, and saturating adsorption nature of the ALD process). O_3 purge time of 20 s is required at least to remove by-products and excess precursors in the process chamber to avoid condensation of the precursor (i.e., CVD-like deposition) on the surface of the substrate.

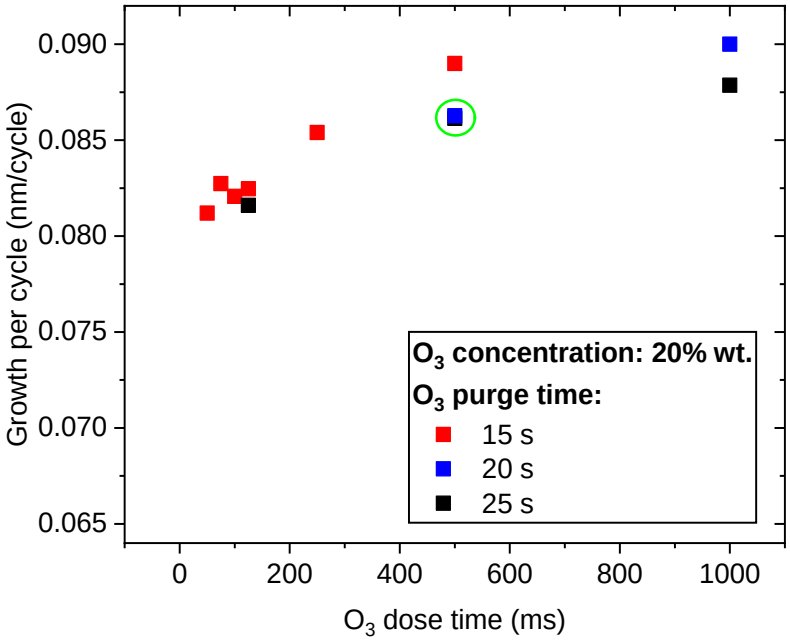

Figure 4.7 Change in growth per ALD cycle of Al_2O_3 films depending on O_3 dose time for varied O_3 purge times and depositions with O_3 concentration of 20% wt..

As the last step of ALD process optimization, ALD deposition temperature has been varied to confirm the ALD temperature window. O_3 concentration was kept constant for MKS O3CS AX8561 ozone generator to be 20% wt.. The same growth behavior is observed for the ALD deposition temperature in the range of 100-300 °C, as GPC values are shown in Figure 4.8 for each deposition temperature, compared to previous results [34]. In conclusion, optimum ozone-based thermal ALD Al_2O_3 deposition parameters are determined as shown in Table 4.1 for the ozone concentration dependent ALD Al_2O_3 passivation study.

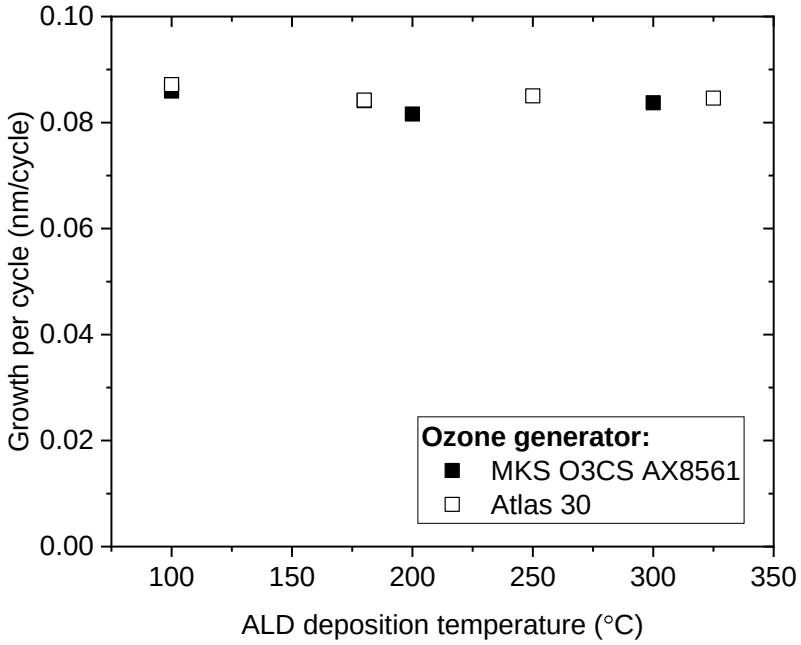

Figure 4.8 GPC behavior depending on the ALD deposition temperature. GPC values of ALD Al_2O_3 depositions by using Atlas 30 ozone generator is adopted from [34].

Table 4.1 Optimized ozone-based thermal ALD Al_2O_3 deposition parameters

Ozone concentration	*TMA dose time (ms)*	*TMA purge time (s)*	*O_3 dose time (ms)*	*O_3 purge time (s)*	*O_2 flow (SLM)*
20% wt.	20	2	500	20	2.5
5% wt.	20	2	500	20	8

Injection-dependent effective minority carrier lifetime τ_{eff} results of 10 nm thick ozone-based thermal ALD Al_2O_3 deposited with optimized deposition parameters, varied ozone concentration, and deposition temperatures on n-type c-Si samples are shown in Figure 4.9. Effective lifetime curves of the samples are shown after FGA temperatures of 425 ℃ and 500 ℃. Effective lifetime results for the varied ozone concentrations and deposition temperatures are close to each other for FGA

temperature of 425 °C. However, the effect of ALD process parameters is more pronounced for FGA temperature of 500 °C.

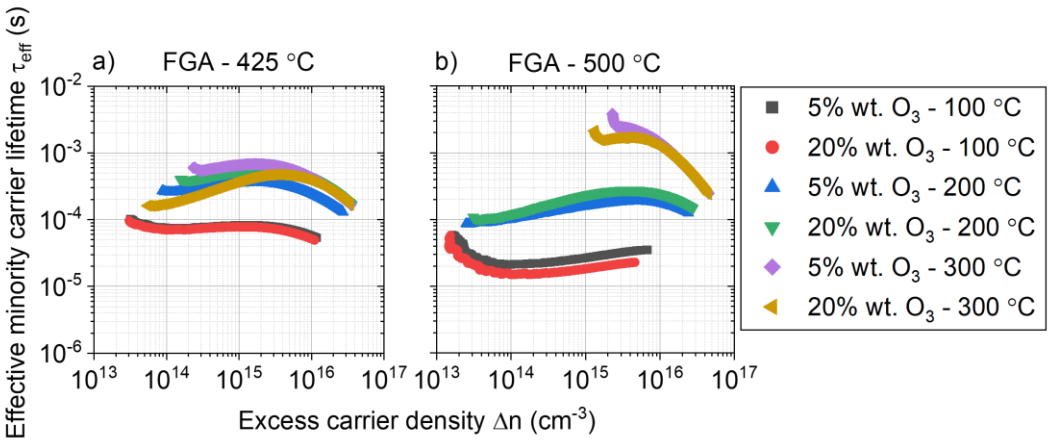

Figure 4.9 Injection-dependent effective minority carrier lifetime τ_{eff} of the ozone-based ALD Al_2O_3 deposited samples with varied ozone concentration and deposition temperature after FGA treatment at a temperature of a) 425 °C and b) 500 °C.

Effective minority carrier lifetime τ_{eff} of the symmetrical Al_2O_3/c-Si/Al_2O_3 samples at an injection level of $\Delta n = 3 \times 10^{15}\ cm^{-3}$ after each 15 minutes of consecutive FGA step is shown in Figure 4.10. Effective lifetime results of ALD Al_2O_3 deposited at different deposition temperatures (100 °C, 200 °C, and 300 °C), whether with low (5% wt.) or high (20% wt.) ozone concentrations, are shown in as-deposited state and after each consecutive FGA step. The most interesting impact of FGA is the shift in the maximum effective lifetime (and hence iV_{oc} values) for varied deposition temperatures. The maximum effective lifetime is observed after annealing at 450 °C, 400 °C, and 500 °C for the ALD deposition temperatures at 100 °C, 200 °C, and 300 °C, respectively. Ozone-based thermal-ALD Al_2O_3 depositions with low and high ozone concentrations exhibit the same trend for each deposition temperature. The highest effective lifetime results achieved are slightly lower than the results in Chapter 4.1. This could be attributed to the effect of c-Si edge passivation. C-Si wafers were cut into quarters to be able to perform annealing under varied ambient.

Therefore, unpassivated c-Si edges lead to a slight decrease in effective lifetime results. Moreover, an identical set of symmetrical Al_2O_3/c-Si/Al_2O_3 samples were annealed under O_2 and forming gas consecutively for 7.5 minutes for each annealing step. Samples with annealing under different gas flows have similar effective lifetime trends depending on the deposition temperature and the ozone concentration. Only FGA performs better than annealing by combining O_2 and forming gas. Therefore, the passivation results of the samples in varied annealing conditions are not shown.

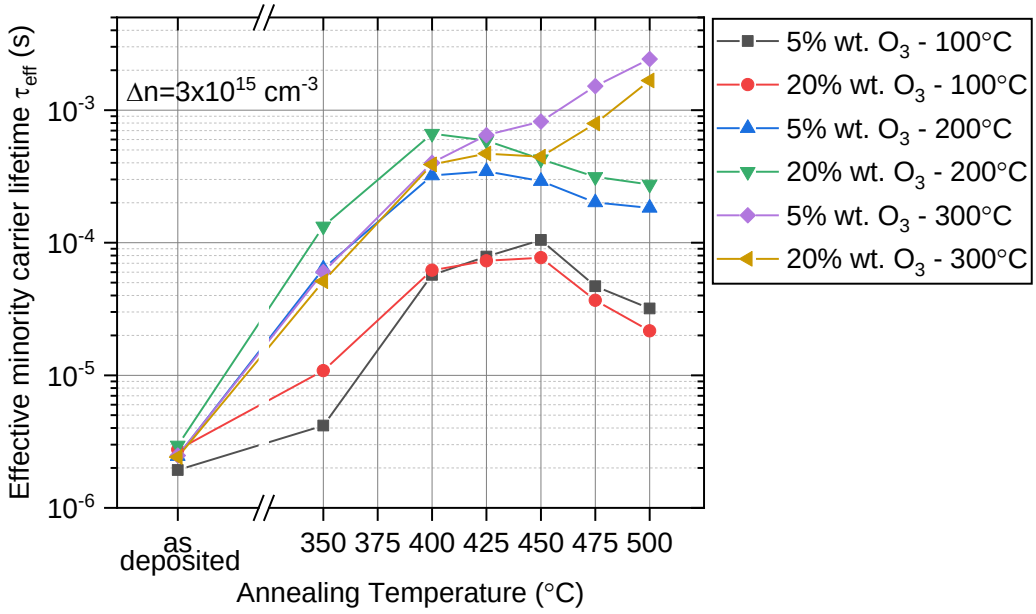

Figure 4.10 Effective lifetime results of n-type c-Si samples at an injection level of $\Delta n = 3 \times 10^{15}\ cm^{-3}$ depending on ALD ozone concentration and the deposition temperature.

Corresponding implied open-circuit voltage iV_{oc} values at 1-sun illumination are given in Figure 4.11. The highest iV_{oc} is 729 mV for ALD deposition temperature of 300 ℃ with 5% wt. ozone concentration. As a result, passivation samples deposited with a temperature of 300 ℃ are prone to be thermally stable up to 500 ℃, and their effective lifetimes improve with the increased FGA temperature. This result is valid for the samples deposited with both low and high ozone concentrations.

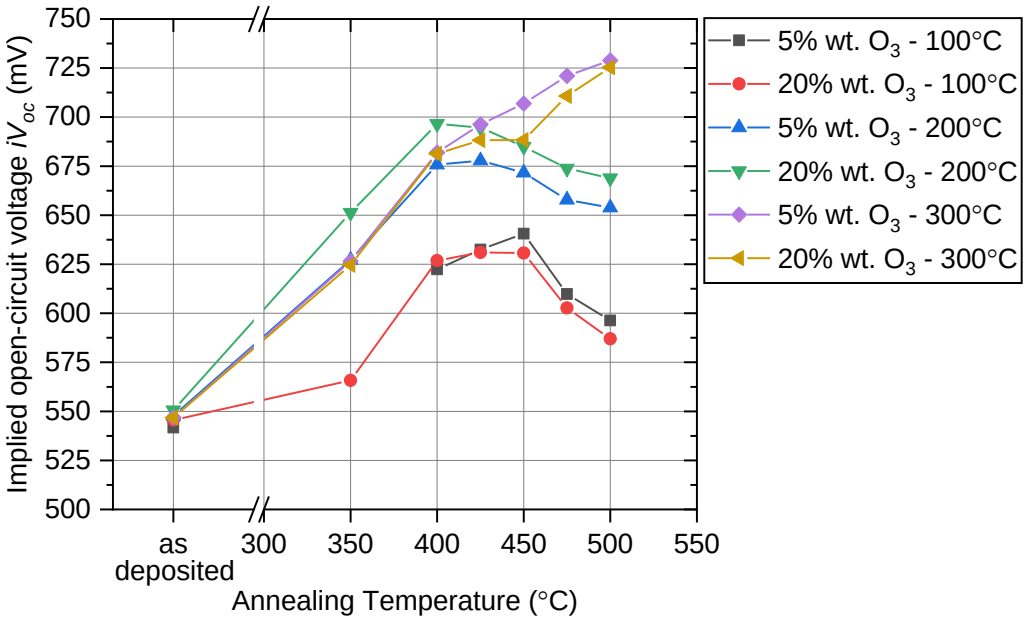

Figure 4.11 Implied open-circuit voltage iV_{oc} of ozone-based ALD Al_2O_3 deposited samples, measured at 1-sun illumination.

Ozone-based ALD Al_2O_3 films fabricated using optimized process parameters are investigated in terms of their compositions by FTIR measurements. Overview FTIR spectra of ALD Al_2O_3 films deposited at various deposition temperatures and with varied ozone concentrations and the assigned vibrational modes are shown in Figure 4.12. The sample compartment is evacuated and purged by dry air to minimize the spectral contribution of water vapor. Then, background measurement is performed and subtracted from the measurements. All spectra are normalized according to the measured thickness of the Al_2O_3 films to subtract the effect of varying optical path length due to shift from nominal film thickness.

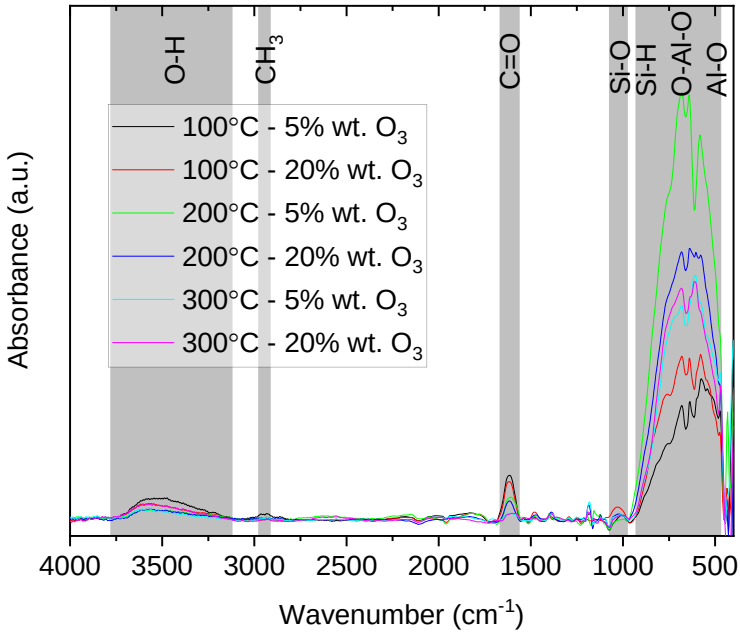

Figure 4.12 Overview FTIR spectra of ALD Al_2O_3 films deposited at varied deposition temperatures and with varied ozone concentrations.

The difference for the absorbance peaks at a wavenumber less than 1000 cm^{-1} is not taken into consideration, as there is a significant influence of silicon substrate as well. Carbon-related absorption peaks are observed for all Al_2O_3 films. At the same time, they are more prominent at the deposition temperature of 100 °C, which might be the reason for lower passivation quality compared to Al_2O_3 films deposited at higher temperatures.

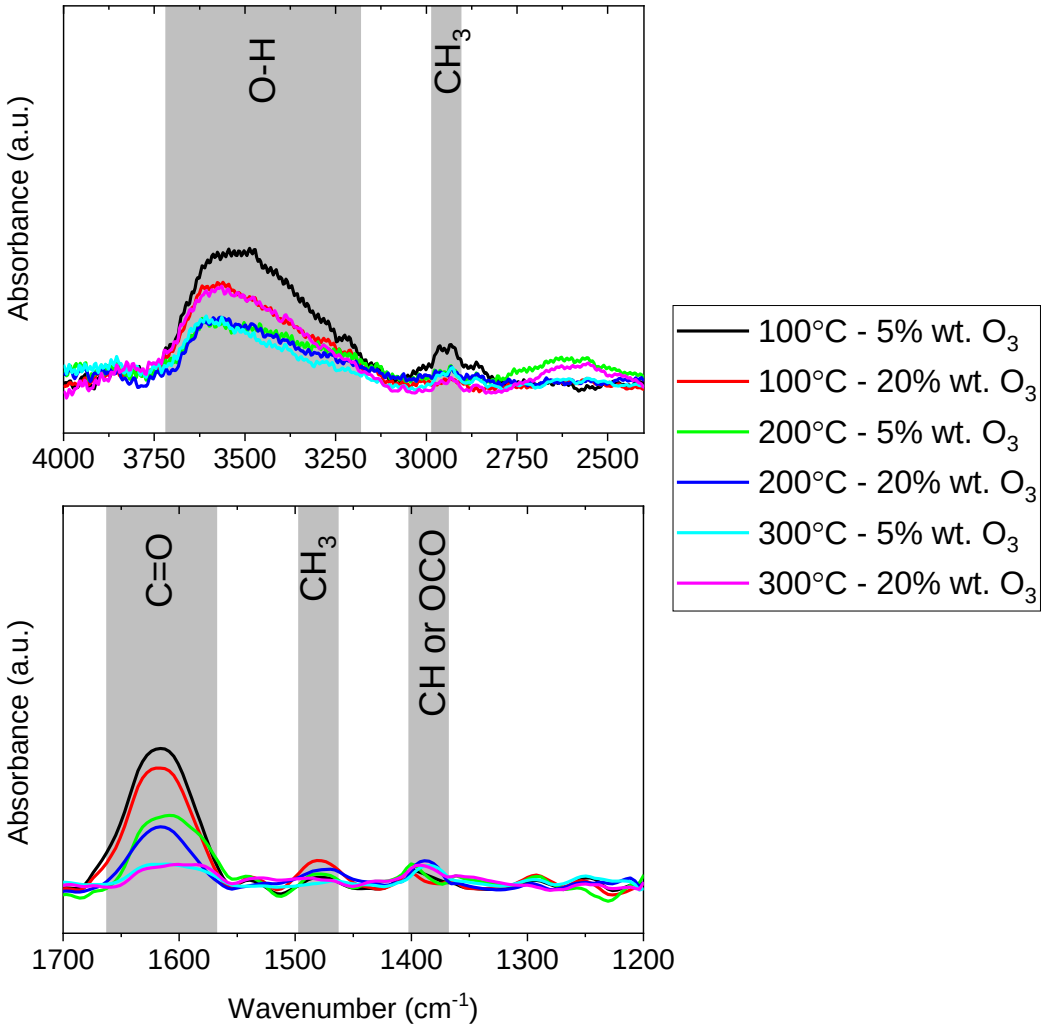

Figure 4.13 FTIR spectra and assigned vibrational modes of ALD Al_2O_3 films for varied deposition temperature and ozone concentrations.

4.2.3 Conclusion

Ozone concentration-dependent thermal-ALD Al_2O_3 films are developed by optimizing the deposition parameters. It is shown that the ozone concentration is a crucial parameter of ozone-based thermal ALD Al_2O_3 depositions in terms of ALD growth behavior. Moreover, the ozone concentration affects the uniformity of Al_2O_3

films. It is concluded that the deposition temperature affects the optimum FGA temperature to achieve a high effective lifetime. This optimized process is used to investigate the implementation of ozone-based thermal ALD Al_2O_3 films in PERC solar cells in Section 4.3.

4.3 Thermal-ALD Ozone Concentration-Dependent c-Si Surface Passivation for PERC Applications

4.3.1 Experimental Details

Symmetrical lifetime test structures were fabricated on shiny-etched p-type FZ c-Si wafers with a resistivity of 1 Ωcm and a thickness of 250 μm. The c-Si wafers were subjected to standard RCA cleaning followed by thermal oxidation at 1050 °C to remove FZ defects [29]. The oxide was removed prior to ALD Al_2O_3 depositions. 3.5 nm, 6.5 nm, and 10 nm thick Al_2O_3 layers were deposited on c-Si via thermal-ALD (Oxford Instruments, FlexAL) using TMA and ozone (O_3) precursors at deposition temperatures (T_{Dep}) of 200 ℃ and 300 ℃. Ozone concentration in ALD cycles was tuned via MKS Instruments O3CS AX8561 ozone system from 5% wt. (73 g/Nm^3) to 20% wt. (306 g/Nm^3). The total number of cycles in ALD processes was adapted according to the ozone concentration to obtain similar Al_2O_3 thickness.

Al_2O_3 deposited samples were subjected to consecutive FGA with varying temperatures from 350 °C to 500 °C with 50 ℃ increments for 15 minutes in a tube furnace. Another set of Al_2O_3 samples was capped with 70 nm of anti-reflection coating SiN_x deposited at 350 °C using inline PECVD (MAiA, Meyer Burger). Al_2O_3/SiN_x stacks were either subjected to consecutive FGA as described above or fast-firing in a rapid thermal annealing furnace. The fast-firing profile was mimicked by a rapid thermal annealing furnace according to the firing profile of an inline fast-firing oven with a peak firing temperature of 750 °C or 800 °C. The typical fast-firing profile is given in Appendix A. These temperature values were preferred as they are typical firing temperature of PERC solar cells after metallization.

Passivation quality of both Al_2O_3 films and Al_2O_3/SiN_x stacks were investigated with injection-dependent effective minority carrier lifetime measurements (Sinton WCT-120 lifetime tester) and quasi-steady-state photoluminescence calibrated minority carrier lifetime imaging. The latter method is especially crucial for samples with non-uniformity, as it enables spatially resolved lifetime measurement [35]. Blistering behavior was investigated by microscope imaging (Olympus MX61). The thickness and uniformity of the deposited films were analyzed via spectroscopic ellipsometry measurements (J.A. Woollam Co.). The process flow is shown in Figure 4.14.

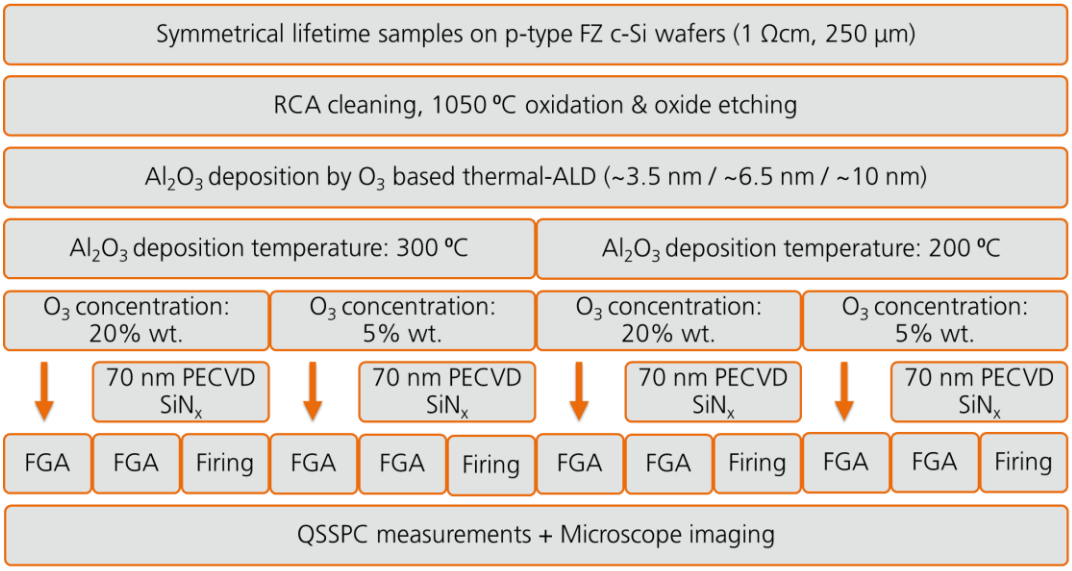

Figure 4.14 Process flow for Al_2O_3 and Al_2O_3/SiN_x samples with varied ALD parameters.

4.3.2 Results and Discussion

A photograph of an Al_2O_3/SiN_x deposited c-Si sample, and the corresponding photoluminescence (PL) image of the sample is shown in Figure 4.15 as an illustrative example. A triangular non-uniformity of the deposited film is observed, which can be seen by an eye inspection. Thickness mapping of Al_2O_3 film deposited at 300 °C with an ozone concentration of 20% wt. is shown in Figure 4.16. Thicker

Al_2O_3 film deposition at the edge of the wafer is also confirmed by spectroscopic ellipsometry measurements. This is attributed to the nature of the thermal-based Al_2O_3 ALD process resulting in backside deposition of the sample. However, a significant improvement in the uniformity of Al_2O_3 films is obtained for the ALD processes utilizing a low ozone concentration. Non-uniformity of the deposited films with high ozone concentration is also evident in quasi-steady-state (QSS)-PL calibrated minority carrier lifetime images as shown in Figure 4.17. While Al_2O_3 films deposited with 5% wt. O_3 concentration have non-uniformity in the range of 1.5-3%, non-uniformity of the Al_2O_3 films deposited with 20% wt. O_3 concentration reaches up to 11%.

a) b)

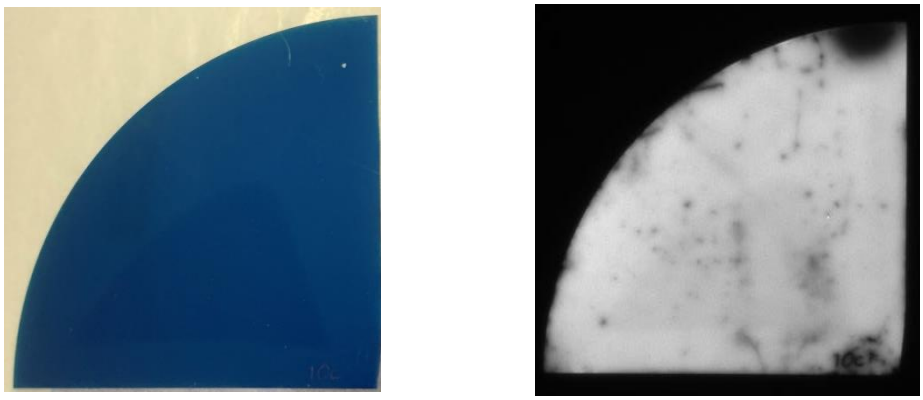

Figure 4.15 a) Photograph and b) Photoluminescence (PL) image of c-Si wafer after Al_2O_3/SiN_x stack deposition.

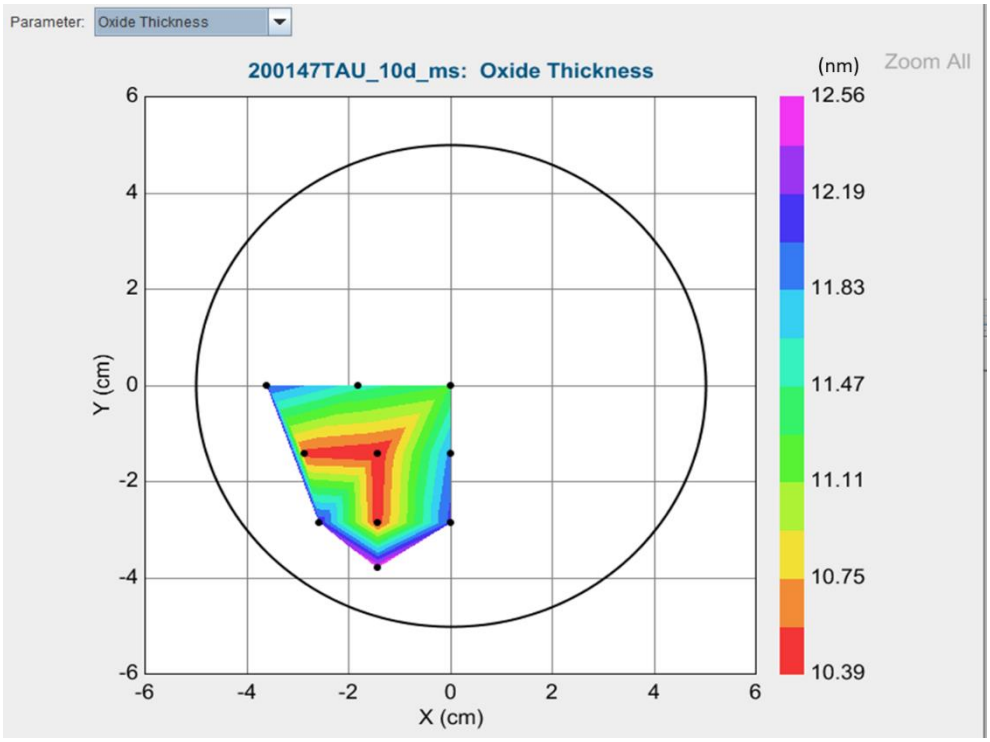

Figure 4.16 Thickness mapping of Al_2O_3 layer deposited at 300 °C with an ozone concentration of 20% wt..

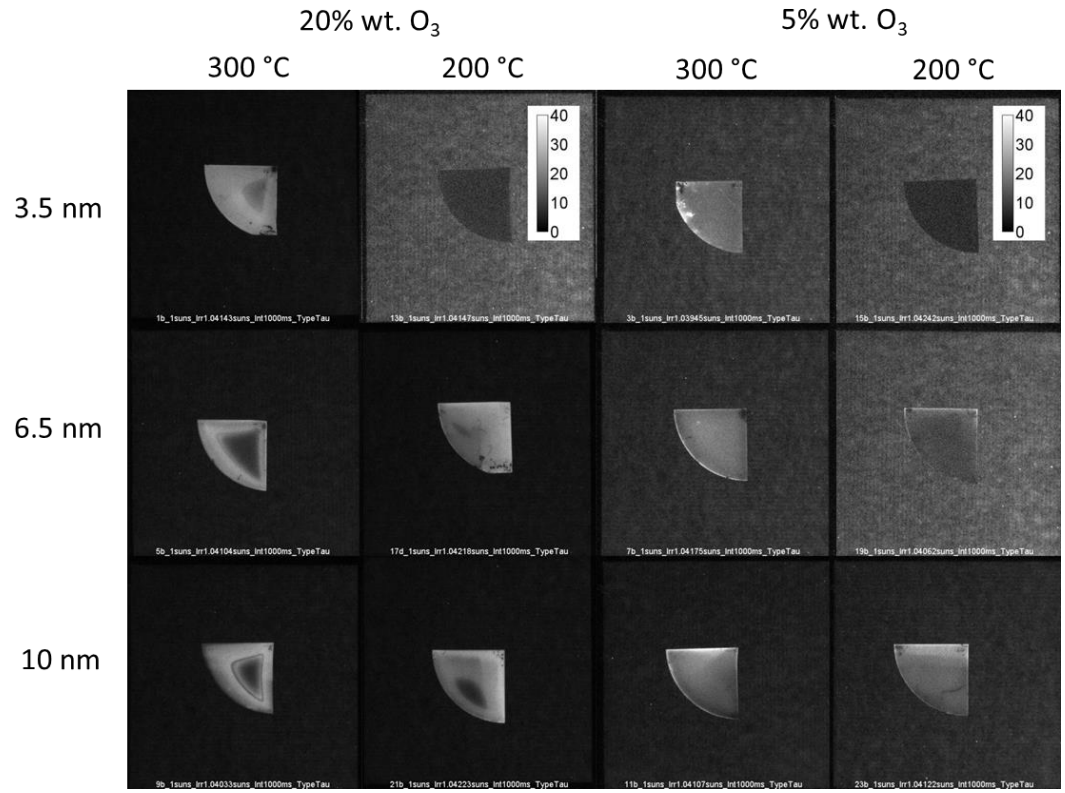

Figure 4.17 QSS-PL calibrated effective lifetime images of Al_2O_3 deposited samples without any thermal treatment.

QSS-PL calibrated effective lifetime images of Al_2O_3 deposited samples with varied ALD deposition temperatures, ozone concentrations, and Al_2O_3 thicknesses after FGA at 500 ℃ are shown in Figure 4.18. QSS-PL calibrated effective lifetime results, and the corresponding PL responses agree with the effective lifetime results obtained from PCD measurements. Therefore, effective lifetime results extracted from the PCD measurements are shown in the next part of this section.

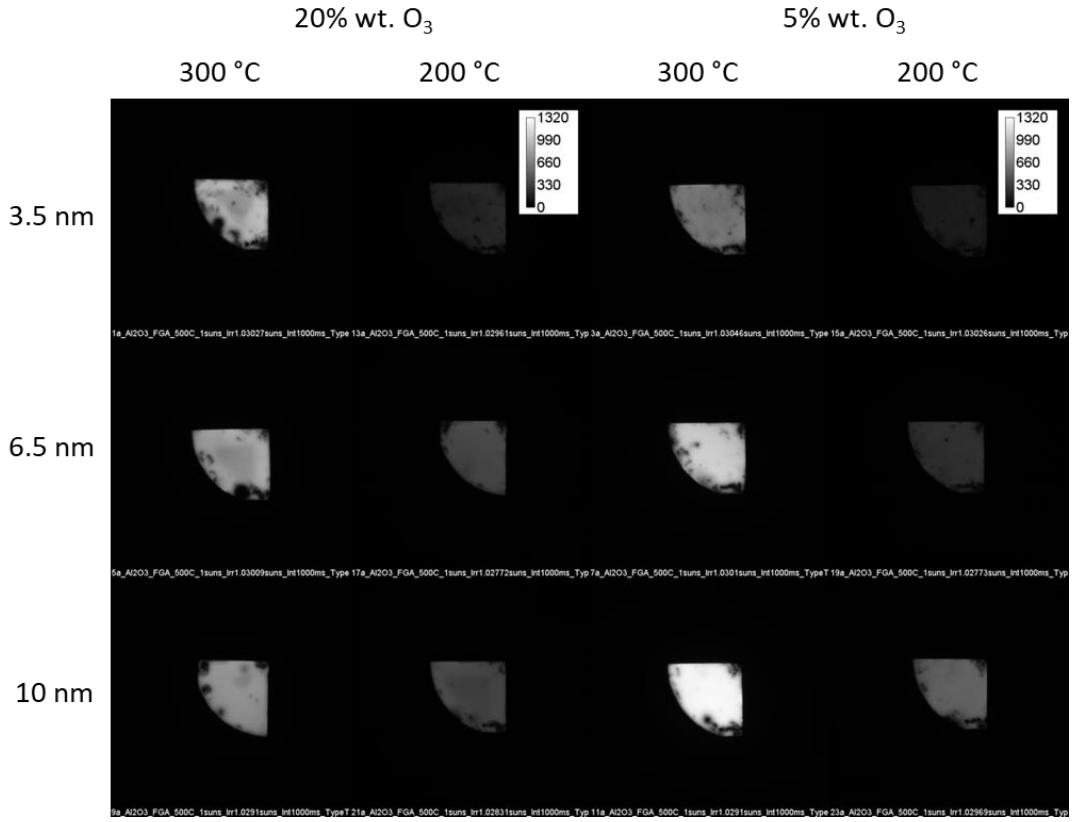

Figure 4.18 PL calibrated effective lifetime images of Al_2O_3 deposited samples with varied ALD deposition temperatures, ozone concentrations and Al_2O_3 thicknesses after FGA at 500 °C.

Effective charge carrier lifetimes measured at an injection level of $\Delta n = 1 \times 10^{15} cm^{-3}$ after each FGA step are shown in Figure 4.19 for Al_2O_3 samples. Effective lifetimes of Al_2O_3 samples are improved clearly when T_{Dep} increased from 200 °C to 300 °C. Al_2O_3 samples deposited at 200 °C reach almost their highest lifetimes after annealing at 400 °C. The effective lifetime of Al_2O_3 samples deposited at 300 °C even increases for annealing temperatures up to 500 °C for low and high ozone concentrations (5% wt. and 20% wt., respectively). Al_2O_3 samples are generally annealed at a temperature range between 400 - 425 °C in standard FGA processes in literature [25,32]. However, our study shows that the lifetime of ozone-based ALD Al_2O_3 samples is further improved with higher FGA temperatures, especially for higher T_{Dep}. There is a slight increase in the lifetime for

thicker Al_2O_3 films. It is also worth to mentioning that similarly high levels of effective lifetime results are achieved independent of Al_2O_3 thickness by selecting appropriate deposition parameters. This result is crucial to determine passivation layer thickness, especially for PERC solar cell applications. The highest lifetime is achieved with 10 nm thick Al_2O_3 deposited at T_{Dep} of 300 °C with 5% wt. O_3 concentration after FGA at 500 °C, resulting in an effective lifetime of 1.9 ms. None of the Al_2O_3 samples show blistering after any FGA step.

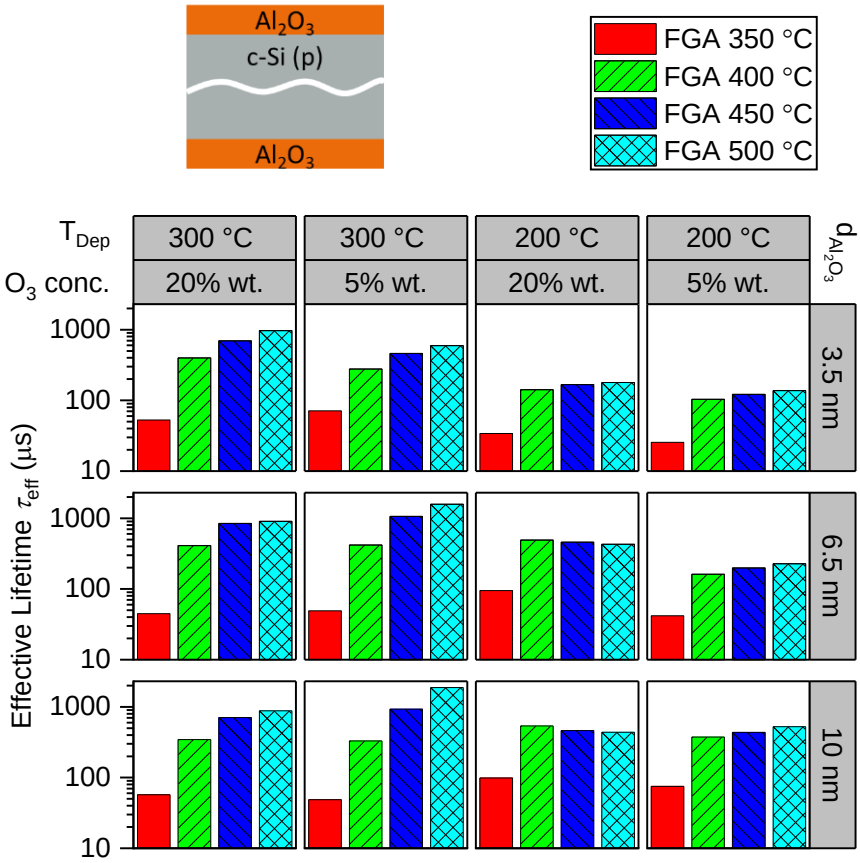

Figure 4.19 Effective charge carrier lifetime results of ozone-based ALD Al_2O_3 samples after consecutive FGA.

Effective lifetime results of Al_2O_3/SiN_x stacks after each consecutive FGA step are shown in Figure 4.20. They exhibit a similar lifetime trend as Al_2O_3 samples when

FGA temperature increases. The lifetime of Al_2O_3/SiN_x stacks after SiN_x deposition indicated by black straight lines (denoted by "As dep.") exhibit better results than Al_2O_3 samples annealed at 350 °C because of SiN_x deposition. In addition, the lifetimes of samples with single Al_2O_3 films, which have poorer passivation quality, improve with the SiN_x capping layer. For instance, an increase in the passivation quality of Al_2O_3 samples for T_{Dep} of 200 °C is observed after capping with SiN_x. However, Al_2O_3 samples already exhibiting high lifetimes are not improved with SiN_x capping. Even if the deposition parameters (i.e., T_{Dep}, O_3 concentration, $d_{Al_2O_3}$) are varied, relatively similar lifetime results are obtained with Al_2O_3/SiN_x stacks compared to samples with single Al_2O_3 layers. The highest lifetime is achieved with 10 nm thick Al_2O_3 deposited at T_{Dep} of 300 °C with 5% wt. of O_3 concentration after FGA at 500 °C (like Al_2O_3 single layers), resulting in an effective lifetime of 1.5 ms. Blistering is not observed for any of the Al_2O_3/SiN_x stacks after the FGA process.

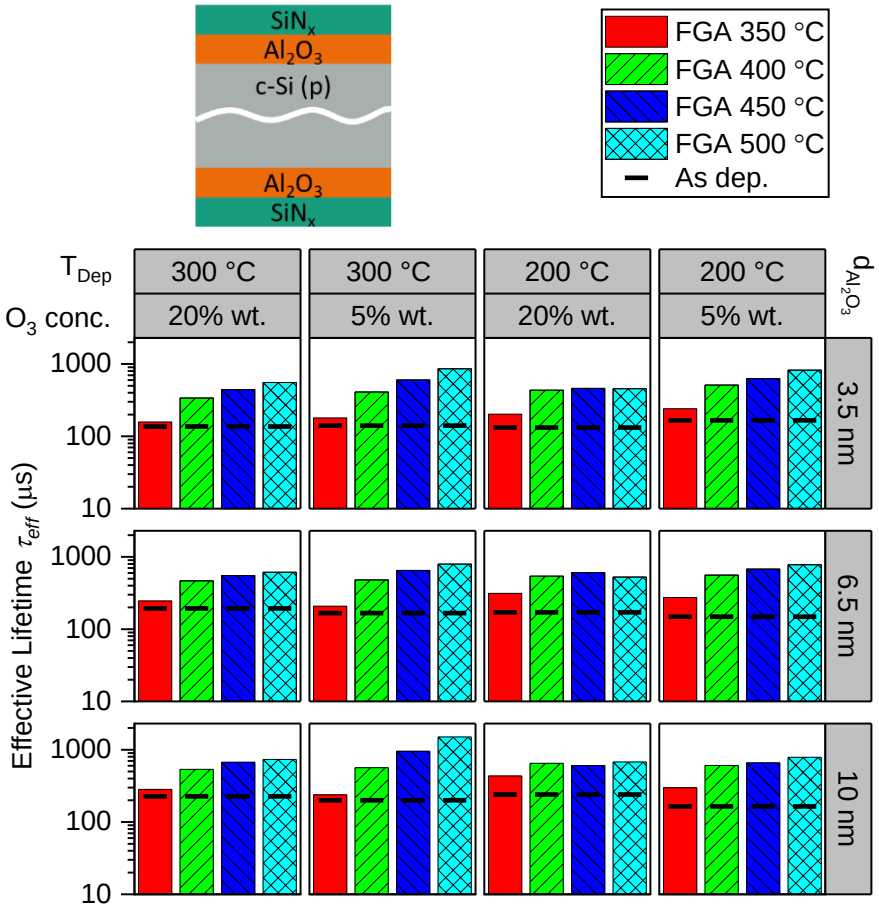

Figure 4.20 Effective charge carrier lifetime results of Al_2O_3/SiN_x stacks after consecutive FGA.

Effective lifetime results of Al_2O_3/SiN_x stacks after firing are shown in Figure 4.21. Lower O_3 concentration outperforms significantly for all ALD Al_2O_3 T_{Dep} and film thicknesses. Surprisingly, passivation quality decreases for thicker Al_2O_3 films deposited with 20% wt. O_3 concentration while it is improved for thicker Al_2O_3 films deposited with 5% wt. O_3 concentration. Similar lifetime results are obtained after fast-firing either at a peak temperature of 750 °C or 800 °C. However, blistering is more pronounced for higher firing temperatures (denoted by the letter 'B' in the lifetime graphs). In addition to high firing temperature, Al_2O_3/SiN_x stacks are prone to have more blistering for higher T_{Dep} of ALD Al_2O_3. However, blister-free

Al_2O_3/SiN_x stacks with excellent surface passivation can be fabricated by choosing suitable deposition parameters. However, blistering does not necessarily mean the samples have a lower effective lifetime.

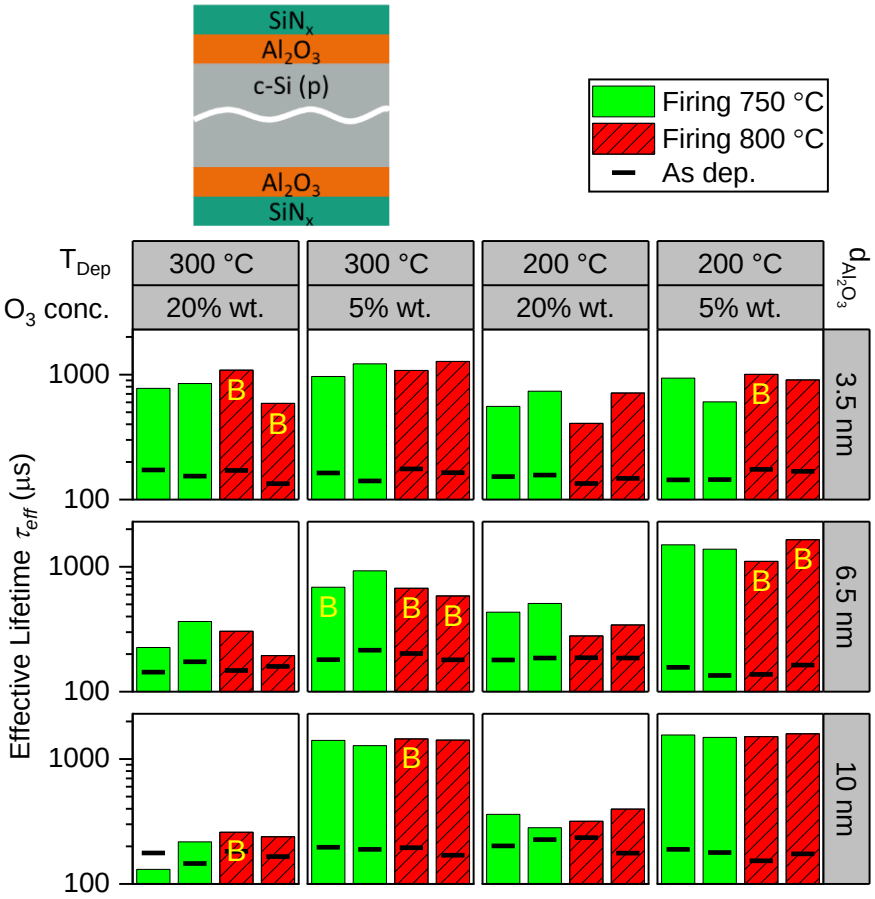

Figure 4.21 Effective charge carrier lifetime results of Al_2O_3/SiN_x stacks after fast-firing with varied temperatures. Samples showing blistering are indicated by letter the 'B'.

Some exemplary microscope images of Al_2O_3/SiN_x stacks with and without blistering formation after fast-firing are shown in Figure 4.22.

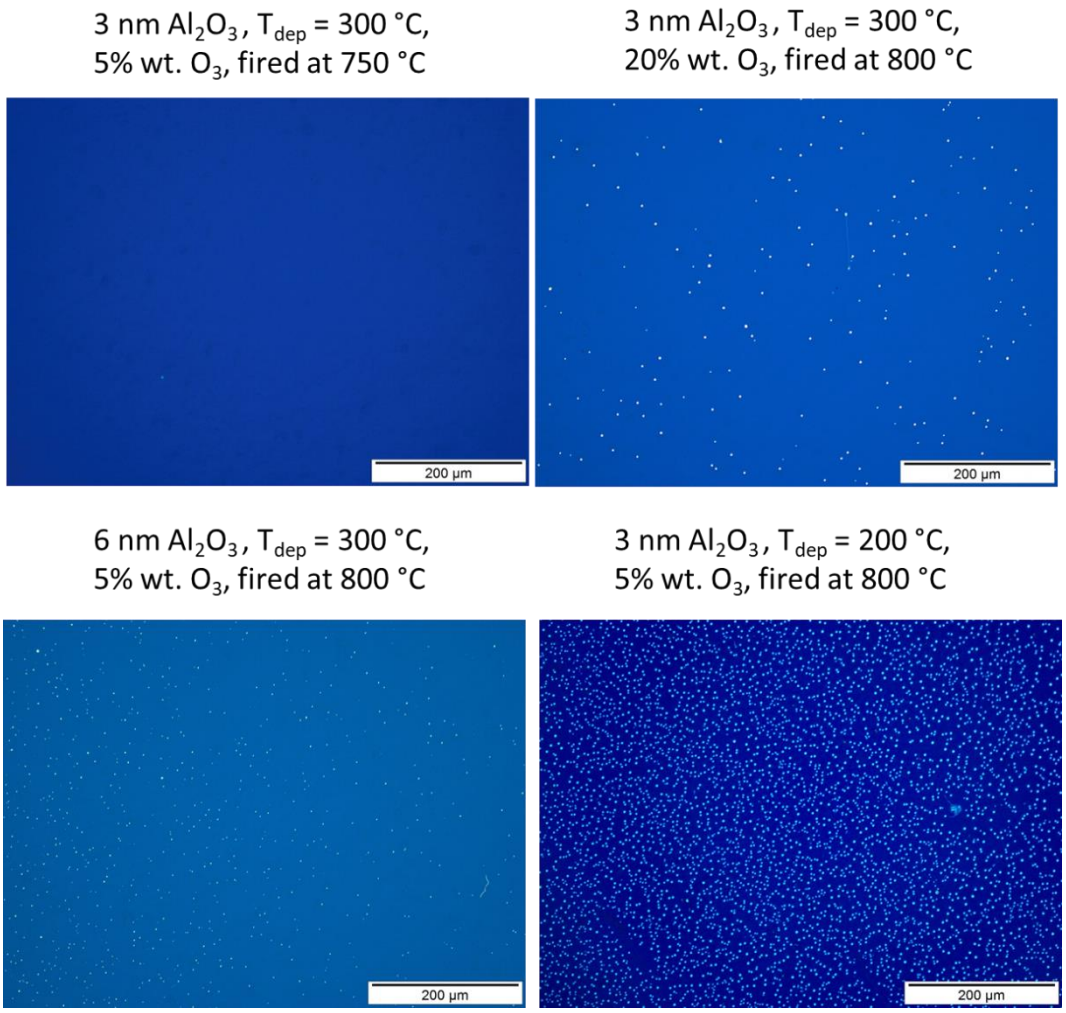

Figure 4.22 Some exemplary microscope images of Al_2O_3/SiN_x stacks after fast-firing to demonstrate blistering behavior.

Table 4.2 Blistering behavior of samples with Al_2O_3/SiN_x stacks for each Al_2O_3 deposition temperature, ozone concentration, Al_2O_3 thickness, and annealing process. Color code: green represents no blistering, yellow (with 'x') represents partial inhomogeneous blistering on some samples, and red (with 'xx') represents severe blistering on samples.

ALD temperature	300 °C					
O_3 concentration	20% wt.	20% wt.	20% wt.	5% wt.	5% wt.	5% wt.
Thermal process	FGA	Firing (750 °C)	Firing (800 °C)	FGA	Firing (750 °C)	Firing (800 °C)
3 nm Al_2O_3			xx			
6 nm Al_2O_3					x	xx
10 nm Al_2O_3			x			x
ALD temperature	200 °C					
O_3 concentration	20% wt.	20% wt.	20% wt.	5% wt.	5% wt.	5% wt.
Thermal process	FGA	Firing (750 °C)	Firing (800 °C)	FGA	Firing (750 °C)	Firing (800 °C)
3 nm Al_2O_3						x
6 nm Al_2O_3						xx
10 nm Al_2O_3						

4.3.3 Conclusion

Regarding improved surface passivation and increasing the efficiency of solar cells to their full potential, Al_2O_3/SiN_x stacks are crucial elements for PERC solar cell technology. Surface passivation can be improved by choosing suitable process parameters. By means of that, optimum stacks are developed by choosing an appropriate process flow without the necessity of an out-gassing step in between the depositions. It is shown that high-quality (i.e., blister-free films with a high effective lifetime) surface passivation films can be fabricated with simplified process flow without the necessity of an out-gassing step. By careful determination of process

parameters, a high effective lifetime up to 1.6 ms, and an implied open-circuit voltage of 728mV are achieved on shiny-etched p-type FZ c-Si with Al_2O_3/SiN_x stacks fired at a high temperature.

CHAPTER 5

BLACK SILICON FABRICATION VIA ICP-RIE AND ITS INCORPORATION IN SILICON SOLAR CELLS

Random pyramidal texturing via wet chemical methods has been a benchmark for c-Si-based solar cell manufacturing. This is a well-known surface modification method to decrease the optical reflection of silicon. It is known that etch rate is a function of etchant solution concentration and dopant concentration in silicon. Moreover, the etching mechanism depends on the crystallographic orientation of the silicon for this etching method [36]. In addition, there have been various attempts to improve the optical absorption of silicon by miscellaneous methods in the literature. By means of these alternative routes, optical gain is acquired by increased absorption of light in the material by surface modifications. Some can be listed as micro- and nanopatterning of the surface via dry etching, laser processing, and wet chemical etching methods. Micro- and nanostructured silicon surfaces have been used for a wide variety of applications. One of the unique applications of micro- and nano-structured silicon is black silicon (b-Si) which has a suppressed optical reflectance in a broad spectral range with an omnidirectional incidence of light. This anti-reflection property is also known to be independent of incident light polarization [37]. B-Si is mostly employed in electro-optical applications such as photodiodes [38-40], photodetectors [41-44], micro-electro-mechanical systems (MEMS) [5,45,46], gas sensors [47], photonics [48-51]. Despite being an indirect semiconductor, b-Si enables silicon to be employed as terahertz emitters [52]. Since the electric field is extremely enhanced in the vicinity of nanostructures, these nanostructured surfaces are also employed in spectroscopic applications such as surface-enhanced Raman scattering (SERS) [53-55]. Furthermore, b-Si is of interest due to its unique surface properties such as superhydrophobicity [56-58] self-cleaning [59-62], and bactericidal activity [63]. Due to these unique surface

properties, b-Si substrates are frequently employed in medicine and biomedical studies for varied purposes such as drug delivery [64,65], biological labeling [66], and bio-sensors [67,68]. Some of the additional b-Si applications that have been extended to various research fields include wafer impurity gettering [69,70], carbon nanotubes [71], lithium-ion batteries [72,73], water splitting [74], photoluminescence [75], laser 3D micro/nano polymerization [76] and boiling heat transfer [77]. In addition, the implementation of b-Si into solar cells is of interest.

The most common b-Si fabrication methods can be listed as metal-assisted wet chemical etching (MACE) [78-88] plasma immersion ion implantation (PIII) [9,77], laser processing [89,90], RIE and ICP-RIE [13,20,91-98]. Other less frequently employed b-Si fabrication methods include electrochemical HF etching [99-101], stain etching [102,103], Fray-Farthing-Chen Cambridge (FFC-Cambridge) process [104] and bottom-up approaches such as chemical vapor deposition (CVD) [105,106] or vapor-liquid-solid (VLS) methods [107,108]. Among these methods, the nano-structuring via RIE reduces the loss of silicon by 67%, which makes it attractive for thin film texturing as well [109].

Compared to conventional surface texturing methods, b-Si has the potential to increase conversion efficiency by absorption enhancement in a wide spectral range when applied in solar cell applications. Therefore, there have been plenty studies on b-Si solar cells in various cell structures, such as aluminum back surface field (Al-BSF) [110-117] PERC [118] , laser-doped selective emitter [119], IBC [120], PERL [121] and TOPCon [122].

This chapter particularly focuses on the b-Si fabrication via ICP-RIE in Section 5.1 and the realization of b-Si PERC solar cells in Section 5.2.

5.1 Black Silicon Fabrication via Reactive Ion Etching Method

5.1.1 Experimental Details

B-Si samples were fabricated by using ICP-RIE Livell plasma tool from Leuven Instruments on p-type, CZ grown, mono c-Si wafers with a resistivity of 1-3 Ωcm and a thickness of 180 μm. Samples were cleaned by RCA cleaning and subjected to various etching treatments prior to b-Si fabrication. SDE was performed by KOH solution with a concentration of 10% wt. at 70 ℃ for 5 minutes. Optimization of the b-Si process was carried out on c-Si wafers either with a dimension of 156x156 mm^2 (M0) or 156.75x156.75 mm^2 (M2). B-Si was fabricated by ICP-RIE in a gas mixture of SF_6 and O_2 at non-cryogenic temperatures. Surface morphology was examined by SEM imaging. Optical characterization of the b-Si samples was carried out by total and diffuse reflectance spectra measured by Bentham PVE 300 system with an integrating sphere. The total weighted average reflectance of the fabricated b-Si samples was calculated in the wavelength range of 350-1100 nm under AM1.5g standard conditions.

5.1.2 Results and Discussion

An optimization study was conducted to fabricate uniform b-Si in a large area on c-Si wafers with a size of M0 and M2. ICP-RIE tool was initially designed for the deep reactive ion etching process for round silicon wafers with a diameter of 8″. Therefore, process chamber has been modified for M0, and M2 sized pseudo square wafer processing within the scope of this study. Some exemplary unsuccessful attempts of b-Si fabrications before the tool modification are shown in Figure 5.1.

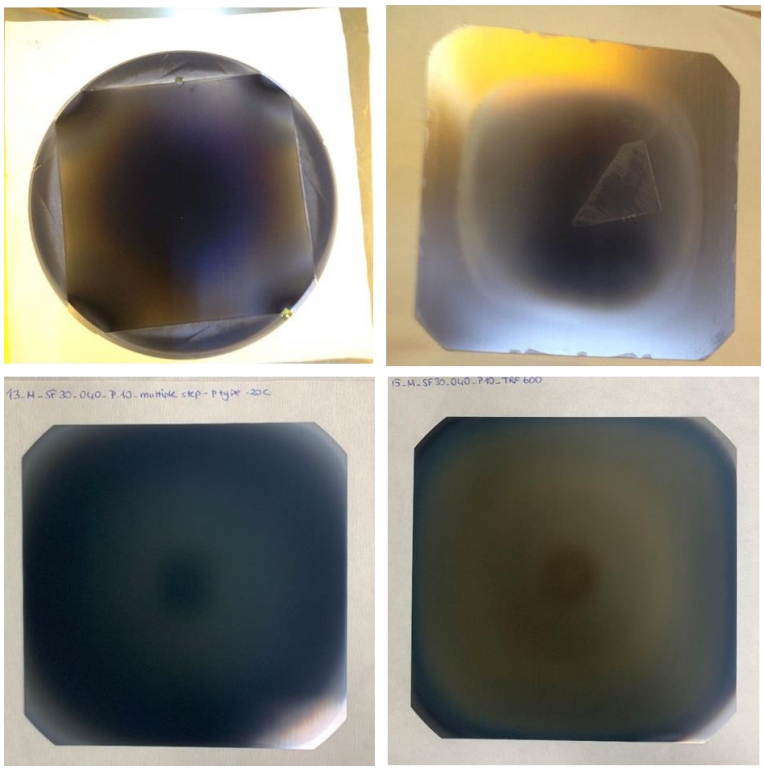

Figure 5.1 B-Si fabrication process results before the modification of ICP-RIE tool and the process optimization.

After the ICP-RIE tool modification, b-Si etching parameters are optimized so that the etching uniformity of the c-Si wafer is improved significantly which is seen in Figure 5.2. Comparable etch rate is achieved throughout the silicon wafer, resulting in homogeneous etching. The etching homogeneity is also confirmed by SEM imaging of the textured surface and reflectance measurements from the different locations of the wafer.

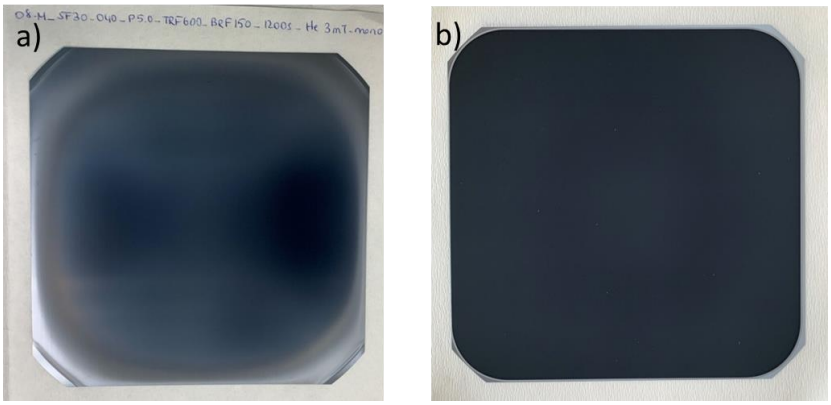

Figure 5.2 Photograph of ICP-RIE processed c-Si wafers a) before and b) after the process optimization.

To investigate the effect of pre-etching treatments on surface morphology and optical properties of b-Si samples, either as-cut, saw damage etched (SDE), or random pyramidal textured wafers are subjected to the b-Si process. Moreover, b-Si processes are carried out either in RIE mode or ICP mode that ions are accelerated towards the c-Si by an additional RF source. SEM images of b-Si samples with different pre-etching treatments and processed by ICP-RIE mode or RIE mode are shown in Figure 5.3. It is observed that there is a significant role of pre-etching treatments on both homogeneity of the b-Si texturing and the surface morphology of the b-Si texturing. A b-Si process on the as-cut c-Si wafer without any pre-texturing results in poor homogeneity of texturing on the c-Si. Moreover, b-Si texturing is not sufficient to remove the saw marks. Mechanical stress induced by the saw damage bends the wafers during the RIE process. This reduces the solar cell fabrication yield and causes problems in the solar cell fabrication steps since the bending is permanent. The saw marks are still clearly visible after both ICP-RIE and RIE processes for 20 minutes, where their surface morphologies are shown in Figure 5.3a and Figure 5.3c, respectively. Wafer bending due to plastic deformation can be avoided by surface pre-treatments. It is crucial to perform either a saw damage etching process with a low concentration KOH solution or a random pyramidal

texturing on the c-Si before the b-Si process to remove the saw marks and eliminate the saw damage.

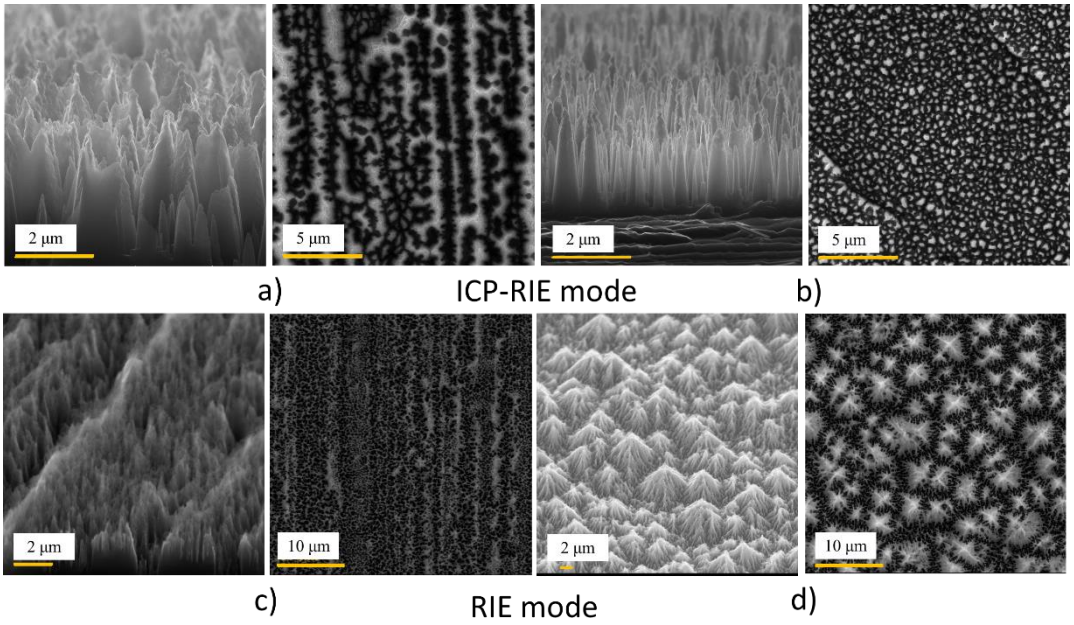

Figure 5.3 SEM images of b-Si samples processed by ICP-RIE mode (a and b) or RIE mode (c and d)

Optical characterization of b-Si samples with different morphologies is carried out by reflectance measurement. All the samples show superior optical properties with a low reflectance in the range of 350-1100 nm. The total weighted average reflectance of b-Si samples with different pre-etching treatments is calculated in the wavelength range of 350-1100 nm under AM1.5g standard conditions, as given in Table 5.1. It is observed that total reflectance is reduced by utilizing the ICP-RIE mode. This is attributed to the increased aspect ratio of the nanotextures with the help of enhanced ion-assisted etching (i.e., boosted ion bombardment). This is an expected result since reflectance values decrease as the aspect ratio of the nanostructures increase [93]. The corresponding total reflectance spectra of b-Si samples with different pre-etching treatments are shown in Figure 5.4. Minimum total reflectance is obtained for SDE samples processed in ICP-RIE mode as 2.3%. Regardless of which mode or

pre-etching treatment is used, reflectance reduces after b-Si texturing, which shows superior optical properties without additional ARC film deposition required.

Table 5.1 Total weighted average reflectance of b-Si samples with various pre-etching treatments.

Wafer type	*RIE mode*	*ICP-RIE mode*
SDE	3.2 %	2.3 %
As-cut	3.9 %	2.6 %
Pyramidal text.	4.3 %	3.0 %

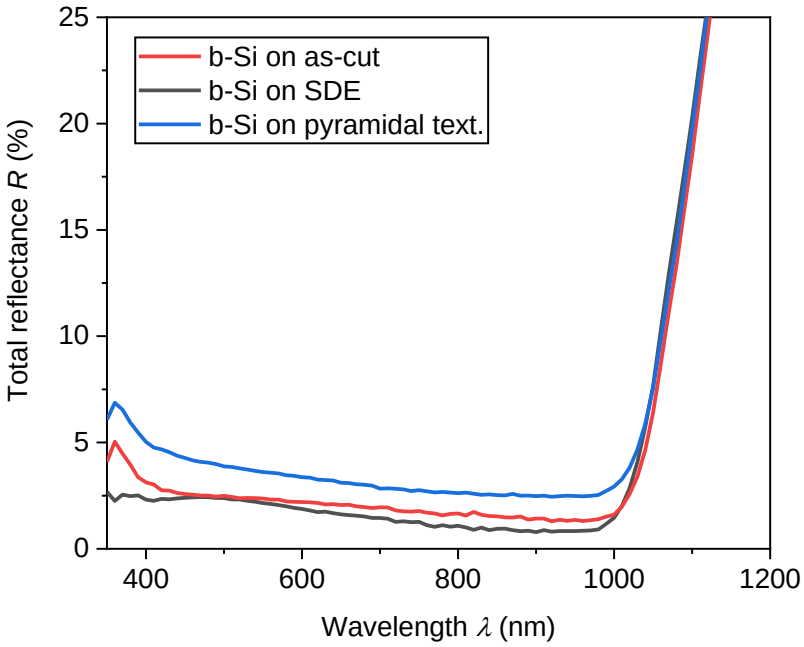

Figure 5.4 Total reflectance spectra of b-Si on the samples with different pre-etching treatments.

Total reflectance spectra of b-Si textured c-Si wafers with varied process parameters are given in Figure 5.5. Relative reflectance of the samples is measured with respect

to barium sulfate disk with an assumption of 100% reflectance. Reflectance measurements are carried out from three different locations on the c-Si wafer, and the averaged spectra are reported. It is seen that the reflectance reduces in a wide spectral range when process pressure is increased from 5 mTorr to 10 mTorr. This is due to the increased chemical etch rate when the pressure is increased during the etching process.

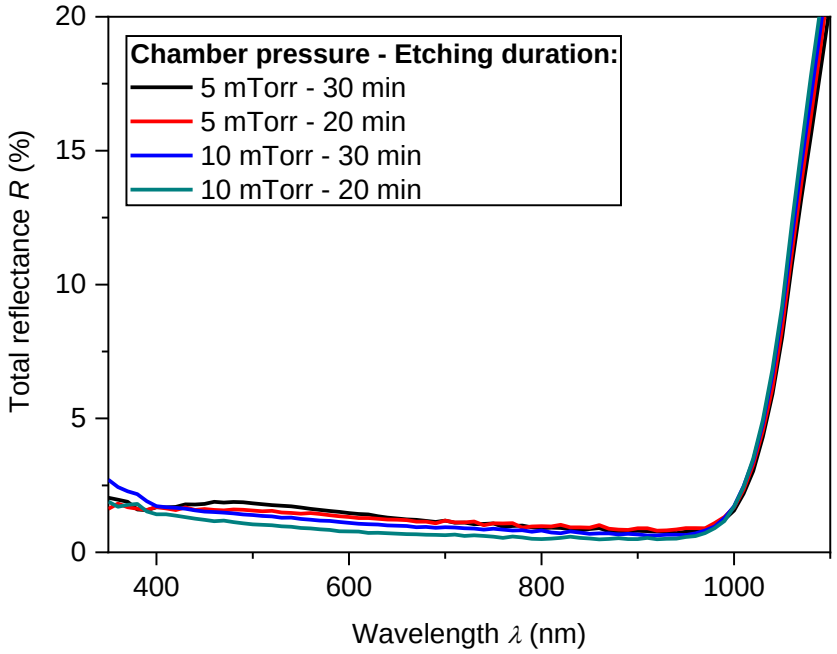

Figure 5.5 Total reflectance of b-Si samples fabricated on SDE c-Si with varied chamber pressure and process durations.

Considering that the difference between the total and diffuse reflectance is negligible (not shown), reflectance haze approaches 100%, especially in the UV region, indicating a superior coupling of light into the b-Si samples. Regarding the etching uniformity and reflectance results, b-Si fabrication is optimized with the process parameters shown in Table 5.2.

Table 5.2 Optimized ICP-RIE etching parameters for the b-Si fabrication

Process parameters	
SF_6 flow	30 sccm
O_2 flow	40 sccm
ICP power	600-700 W
Bottom RF power	0-150 W
Process pressure	5-10 mTorr
Etching duration	10-20 min
Cooling temperature	5 ℃

5.1.3 Conclusion

It is demonstrated that ICP-RIE Livell plasma tool is capable of large area b-Si fabrication with various surface morphologies either in ICP or RIE mode if the tool is modified for pseudo-square wafers. It is shown that there is a significant effect of pre-etching treatments on the surface morphology of b-Si samples. Although similar reflectance values are obtained for the samples with various morphologies, pre-etching treatment is crucial in terms of b-Si uniformity within the wafer and removal of saw damage. Superior b-Si etching uniformity is obtained on both M0 and M2 size c-Si wafers regardless of the doping type of c-Si. A slight difference between the total reflectance and diffuse reflectance of b-Si demonstrates that the b-Si surface has a suppressed optical reflectance in a broad spectral range with an omnidirectional incidence of light. Regarding b-Si application in solar cells, b-Si etching on pyramidal texturing can provide the most suitable surface morphology regarding the aspect ratio of nanostructures and the saw damage marks.

5.2 Influence of Phosphorus Emitter Formation on the Performance of Black Silicon PERC Solar Cells

5.2.1 Experimental Details

PERC solar cells were fabricated on p-type, CZ grown, mono c-Si wafers with a resistivity of 1-3 Ωcm, and a thickness of 180 μm. C-Si wafers, either with a dimension of 156x156 mm^2 (M0) or 156.75x156.75 mm^2 (M2), were used. Wafers were subjected to various etching procedures (i.e., random pyramidal texturing, b-Si etching) depending on the desired surface morphology of the solar cells on the front side. The surface texturing methods and sequences for each group are shown in Table 5.3. SDE was performed by KOH solution with a concentration of 10% wt. at 70 ℃ for 5 minutes. B-Si was fabricated on SDE or pyramidal textured wafers by RIE etching for 20 minutes under a gas mixture of SF_6 and O_2 with a flow of 30 sccm and 40 sccm, respectively, using Leuven Instruments Livell ICP-RIE. These samples are abbreviated as Tex. 1 and Tex. 2, respectively. Another set of samples was subjected to 12 second of KOH treatment with a concentration of 2% wt. at 70 ℃ to reduce the aspect ratio of the nanostructures, which is denoted as Tex. 3. The process flow and schematic cross-section of the fabricated PERC solar cells are shown in Figure 5.6 and Figure 5.7, respectively.

Table 5.3 Surface texturing methods and sequences employed for each group for various surface morphologies

Tex.1	**Tex. 2**	**Tex. 3**	**Pyr.**
SDE	Pyr. texturing	Pyr. texturing	Pyr. texturing
RIE	RIE	RIE	
		KOH	

All samples were cleaned by an ozone cleaning and HF:HCl dip after SDE or pyramidal texturing followed with rinsing by deionized water (DI) and drying under nitrogen flow. Wet chemical processes, such as pyramidal texturing, ozone cleaning, and HF:HCl were carried out by RENA BatchTex automated processing equipment. To investigate the influence of phosphorus (P) emitter formation by various methods, n^+ emitter was formed on both b-Si and pyramidal textured wafers by adopting diffusion and ion implantation methods. Phosphorus diffusion was performed in an atmospheric furnace under the flow of $POCl_3/O_2$ with a flow ratio of 400/2000 sccm. The drive-in step was performed at 875 ℃. For the solar cells with the implanted emitter, different P doses with an energy of 10 keV were employed throughout the P implantation process to obtain various sheet resistances on the samples with different surface morphologies. Samples were subjected to HF dip prior to P activation. If ozone cleaning is performed between the ion implantation and activation steps, it increases Si consumption resulting in removal of the dopants before the activation. The dopant removal is much more pronounced for the b-Si surface which has much larger surface area than the pyramidal textured counterparts. Therefore, ozone cleaning of heavily doped b-Si surface result in more Si removal during the cleaning, leading to low dopant concentration. Although random pyramidal textured solar cells are not much influenced by the intermediate ozone cleaning step, ozone cleaning is strictly not applicable for b-Si nanostructured samples. This phenomenon is confirmed by the numerical simulation of the ozone-based cleaning on the silicon etch rate reported in literature [123]. P activation of the implanted samples was carried out by annealing under nitrogen flow at 875 ℃ for 30 minutes, as previously optimized by our group [124]. 5 nm thick Al_2O_3 film was deposited at 200 ℃ at the rear side of the cells by spatial thermal-ALD from SoLayTec. Then, the samples were annealed at 425 ℃ for 15 minutes under nitrogen flow in a tube furnace for activation and out-gassing purposes. Front SiO_xN_y/SiN_x stack and rear SiN_x films were deposited via PECVD at a temperature of 450 ℃. Laser contact openings (LCO) were realized by using a picosecond laser operating at a wavelength of 532 nm at the rear side. A pulse repetition rate of 400 kHz was adopted. Front and rear

metallizations were carried out by the fully automated Baccini screen-printing tool. While Al fire-through metal paste was used at the rear side, the front metal grid was screen-printed using Ag fire-through metal paste. The fast-firing process was performed at a peak temperature range between 800-850 °C using a conveyor belt furnace. Light I-V measurements were performed on the solar cells using a Class AAA solar simulator. Suns-V_{oc} measurements were carried out by the Sinton WTC-120 tool. Contact resistivity of the front grid was measured on the solar cell stripes taken from the different locations of the solar cells by the TLM method using TLM-SCAN from pv-tools GmbH.

Cleaning and texturing (pyramidal vs. b-Si)	
$POCl_3$ diffusion	P implantation
Single side etching & HF dip	HF dip
	Activation
Rear ALD Al_2O_3 and activation	
Front and rear PECVD SiN_x	
Rear laser contact opening	
Front Ag/Rear Al screen printing	
Fast firing	

Figure 5.6 Process flow of PERC solar cell fabrication.

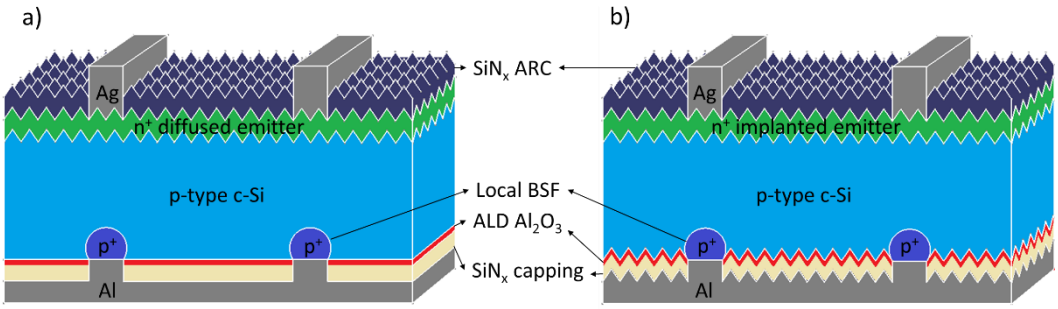

Figure 5.7 Schematic cross-sections of PERC solar cells with a) diffused emitter and b) implanted emitter.

5.2.2 Results and Discussion

The surface morphology of the samples subjected to different surface etching procedures is examined by SEM imaging, as shown in Figure 5.8. While high aspect ratio nanostructures are formed on SDE c-Si via RIE, micron-sized random pyramids still exist after the RIE process on previously pyramidal textured samples. KOH treatment erodes nanostructures, especially at the peaks of the pyramids.

Tex. 1

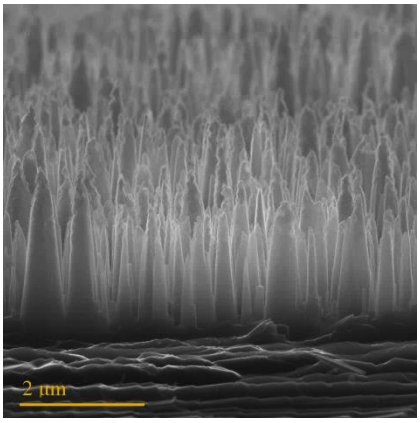

Tex. 2

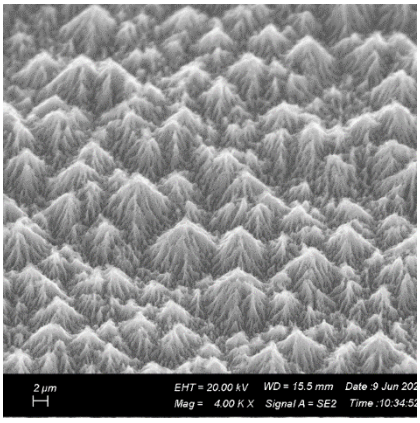

Tex. 3

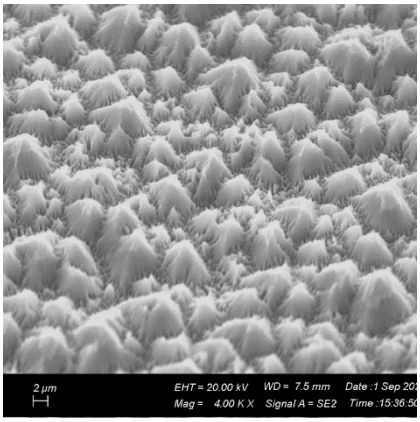

Pyr.

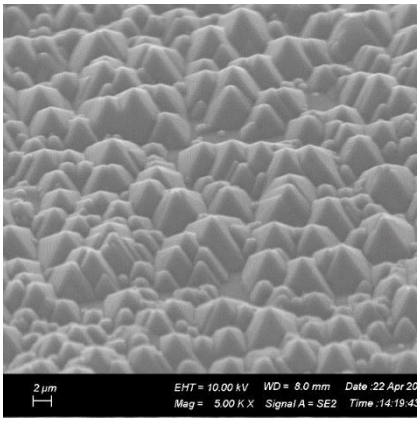

Figure 5.8 SEM images of each group subjected to various surface texturing treatments.

Optical characterization results of the c-Si wafers with different surface morphologies are shown in Figure 5.9. Lower reflectance values are obtained in the UV region as the aspect ratio of the structures increases.

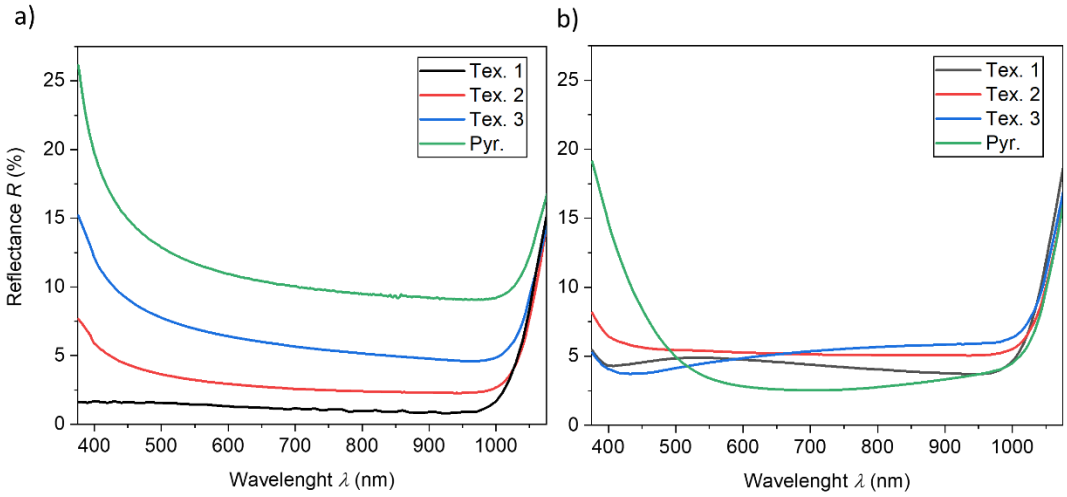

Figure 5.9 Total reflectance spectra of a) textured c-Si wafers with various surface morphologies b) the solar cells with SiO_xN_y/SiN_x ARC film and metal grid.

Fast-firing and screen-printing processes are optimized for b-Si solar cells. PERC solar cells are subjected to fast-firing with varied parameters, and the open-circuit voltage of the solar cells is measured by Suns-V_{oc} measurements, as shown in Figure 5.10. The boxplot consists of V_{oc} data for at least four sub-cells fabricated in the same batch and cut by laser scribing. It is concluded that b-Si solar cells (denoted as Tex. 1) require higher peak firing temperature and slower belt speed to obtain better V_{oc} and contact formation compared to reference PERC solar cells (Pyr.) with random pyramidal etching on the front.

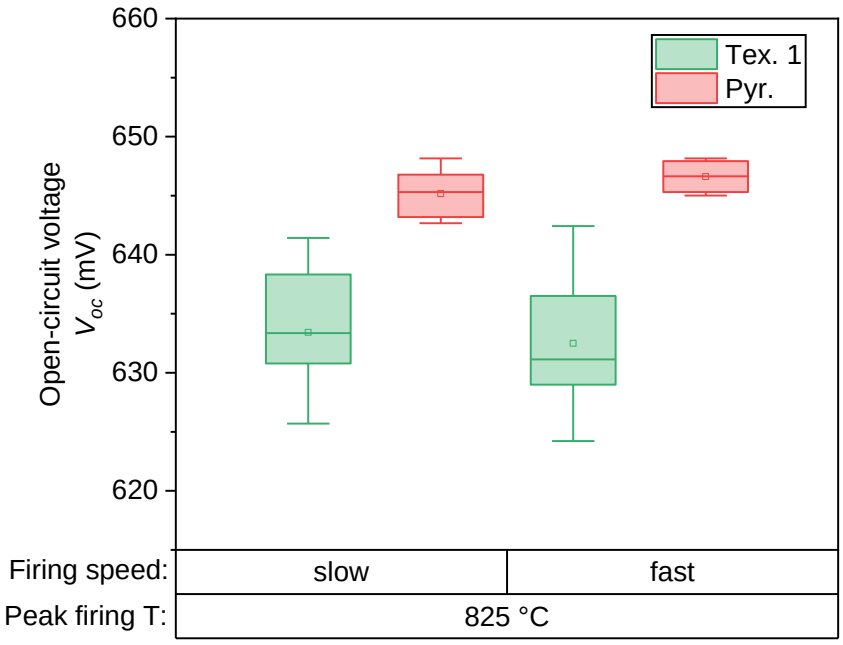

Figure 5.10 Open-circuit voltage values as a function of fast-firing peak temperature and firing belt speed for b-Si (denoted as Tex. 1) and pyramidal textured (denoted as Pyr.) c-Si PERC solar cells.

With the knowledge transferred from these results, b-Si and random pyramidal textured solar cells were fabricated with implanted and diffused emitters. A photograph of solar cells taken from the front side is shown in Figure 5.11.

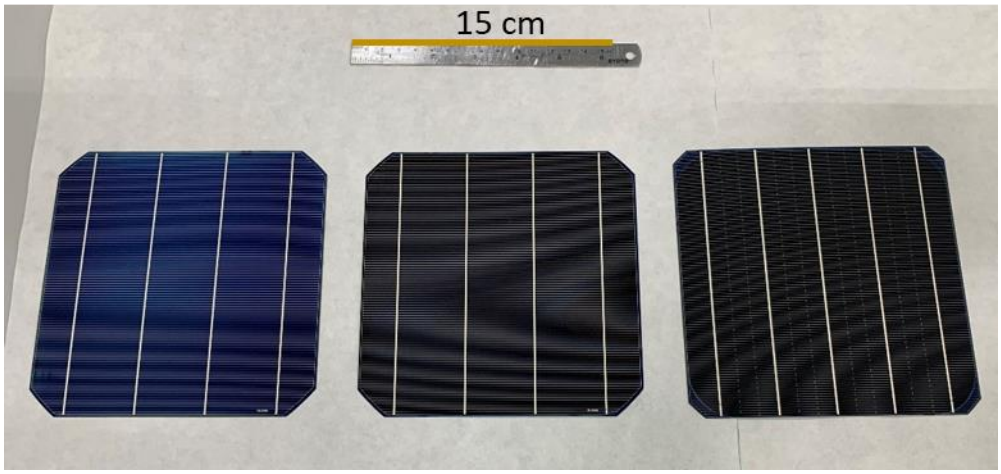

Figure 5.11 Photograph of pyramidal textured (left) and b-Si textured solar cells.

Solar cell parameters extracted from J-V measurements of the solar cells with the implanted and diffused emitters are given in Table 5.4 and Table 5.5, respectively. D1, D2, and D3 correspond to the dose (ion flux) of P during the implantation process. Regarding the diffusion and implantation methods for the emitter formation, excessive ion flux of implantation is required to achieve comparable sheet resistance with diffused samples. Due to being directional, the ion implantation method is more sensitive to surface morphology than diffusion, resulting in more significant variation in sheet resistance. Sheet resistances of doped (diffused or implanted) b-Si samples are likely to be overestimated in the case of current flow being disturbed locally due to the nanostructures on the surface. Still, 4-point-probe (4pp) method enables a qualitative comparison between the various samples and gives comparable values. In contrast to implantation, diffusion on b-Si results in lower sheet resistance than the pyramidal textured surface, as increased surface area boosts phosphorus segregation from PSG into the silicon [116,125,126]. In the case of P implantation, a highly doped shallow emitter is formed on the high aspect ratio structures, resulting in increased sheet resistance. This phenomenon is also consistent with the simulation results shown in the literature [127].

Since the light coupling in the b-Si solar cell is more efficient than the random pyramidal textured solar cells, the photogenerated current density is expected to be higher for b-Si solar cells. However, there is a significant drop in J_{sc} for b-Si solar cells compared to the reference solar cells, which indicates that the recombination current density is much more pronounced for the b-Si solar cells. There are two distinct recombination mechanisms that predominate for b-Si solar cells compared to random pyramidal textured solar cells. First, due to the damage of plasma etching during b-Si fabrication via ICP-RIE, the surface recombination is more pronounced. Moreover, passivation of the b-Si surface by PECVD SiO_xN_y/SiN_x films is not an optimum option. The second main reason is higher contact resistance values on b-Si, which is a result of challenges in having proper metal contact on b-Si via the screen-printing method. Since surface recombination is much more pronounced for b-Si solar cells, the collection probability of the generated carriers decreases significantly

in regions closer to the b-Si surface. It is beneficial to generate carriers close to the depletion region than the surface. Therefore, deep emitter formation is crucial not only to avoid Shunt resistance but also to achieve higher J_{sc} values.

Table 5.4 Solar cell parameters of PERC solar cells with implanted emitter extracted from the light J-V measurements.

Texturing	R_{sheet} ($\Omega/\square$)	V_{oc} (mV)	J_{sc} (mA/cm^2)	*FF* (%)	*PCE* (%)
Tex. 1 (D1)	60	622	27.6	78.8	13.6
Tex. 2 (D1)	120	602	34.4	76.4	15.9
Tex. 2 (D2)	75	606	32.9	76.7	15.3
Tex. 3 (D3)	73	592	33.0	76.0	14.9
Pyr. (D1)	57	634	37.6	77.7	18.6
Pyr. (D2)	42	622	36.6	77.3	17.6

Table 5.5 Solar cell parameters of PERC solar cells with diffused emitter extracted from the light J-V measurements.

Texturing	R_{sheet} ($\Omega/\square$)	V_{oc} (mV)	J_{sc} (mA/cm^2)	*FF* (%)	*PCE* (%)
Tex. 2	38	620	31.0	77.2	14.9
Tex. 3	47	633	35.0	77.3	17.1
Pyr.	55	649	37.7	77.6	19.0

The higher the aspect ratio of the nanostructures, the more hydrophobic the surface is, which introduces a challenge in the screen-printing process resulting in disconnected fingers and hence reduced *FF*. This issue has been addressed in the literature [128]. However, compared to the implanted b-Si solar cells on Tex. 1, a 5-fold improvement in the contact resistivity of b-Si solar cells is achieved by the emitter formation via diffusion on Tex. 3 surface, as shown in Figure 5.12. Therefore,

surface morphology and the doping method play a crucial role in determining contact resistivity and hence *FF* of b-Si solar cells. The boxplot demonstrates contact resistivity distribution in solar cell stripes from the different parts of the wafer with a measurement of at least 90 fingers for each stripe.

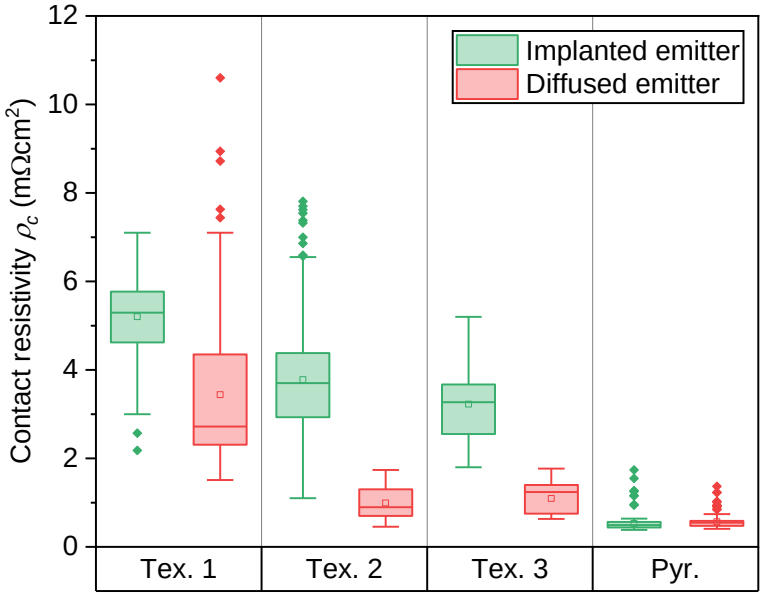

Figure 5.12 Contact resistivity of Ag screen-printed Ag front fingers on varied surface textures.

To overcome the metallization issue on b-Si, the screen-printing parameters are optimized and applied on b-Si solar cells with a better finger grid design which is the rightmost b-Si solar cell in Figure 5.11. Another set of solar cells is fabricated using a 5-busbar front grid with an increased number of fingers, the results of which are shown in It is observed that *FF* values increase significantly with the front grid improvement at the same time, its positive effect on J_{sc}. B-Si PERC solar cell is fabricated with a power conversion efficiency of 19.7% which is comparable to the standard random pyramidal textured PERC solar cell efficiencies. Diffused emitter performs better than the implanted emitter in terms of b-Si solar cell efficiency even if diffused emitter results in lower sheet resistance, increasing Auger recombination.

Table 5.6. It is observed that *FF* values increase significantly with the front grid improvement at the same time, its positive effect on J_{sc}. B-Si PERC solar cell is fabricated with a power conversion efficiency of 19.7% which is comparable to the standard random pyramidal textured PERC solar cell efficiencies. Diffused emitter performs better than the implanted emitter in terms of b-Si solar cell efficiency even if diffused emitter results in lower sheet resistance, increasing Auger recombination.

Table 5.6 Solar cell parameters of PERC solar cells with diffused (denoted as dif.) or implanted emitter with improved front fingers extracted from the light J-V measurements.

Texturing	R_{sheet} ($\Omega/\square$)	V_{oc} (mV)	J_{sc} (mA/cm^2)	*FF* (%)	*PCE* (%)
Tex. 2 (D2)	60	596	31.6	79.8	15.0
Tex. 2 (dif.)	35	626	31.7	80.5	16.0
Tex. 3 (D1)	70	616	35.9	76.2	16.9
Tex. 3 (dif.)	40	647	37.7	80.7	19.7
Pyr. (D2)	40	630	36.5	80.8	18.6
Pyr. (D3)	45	637	37.4	80.9	19.3
Pyr. (dif.)	48	653	38.2	80.7	20.1

5.2.3 Conclusion

It is concluded that b-Si PERC solar cell manufacturing has some challenges compared to its random pyramidal textured counterparts. Understanding of the electrical and optical properties of b-Si solar cells and the corresponding loss mechanisms are required to fabricate high-efficiency b-Si solar cells. Although it is expected to obtain higher short-circuit current density J_{sc} by utilizing b-Si due to

better light coupling into c-Si, J_{sc} values of b-Si solar cells are limited by the increased surface recombination. Moreover, J_{sc} losses are mostly due to the challenge of having proper contact on b-Si surfaces. Optical losses are minimized by utilizing b-Si nanostructures at the front side of the solar cells. However, since a trade-off between optical gain and electrical gain exists, the performance of the b-Si solar cells is limited. Electrical losses are minimized to some extent by reducing the series resistance of the b-Si solar cells. A remarkable improvement of the b-Si solar cell efficiency is achieved by optimizing the fabrication steps, resulting in a power conversion efficiency of 19.7% with a diffused emitter.

CHAPTER 6

DOPANT-FREE CHARGE SELECTIVE CONTACTS FOR C-SI HETEROJUNCTION SOLAR CELLS

Carrier selective contacts have been drawing attention as they are a promising path for c-Si solar cells to move toward their efficiency limits. As an alternative to doped silicon films, dopant-free charge selective contacts utilizing inorganic materials such as transition metal oxides and alkali metal fluorides have been studied extensively in literature [129-135]. Besides inorganic materials, the application of organic materials has also been drawing attention due to their prominent properties such as minimized parasitic absorption, strong dipole moment, and vacuum-free processing. Applying organic materials is appealing as it does not require high-temperature processing. Therefore, the fabrication is fast and simplified, as well as manufacturing costs are reduced. These organic materials have a wide range of application in literature such as work function tuning [136-141], gate dielectric functionalization [142-144], adhesion improvement [145], interface modification in perovskite/silicon tandem solar cells and organic solar cells [146-148], as well as resist material usability [149]. Another remarkable advantage of organic materials is that they can be synthesized with various compounds. Thus, depending on the particular purpose, their electrical, optical, and chemical properties can be modified. With the knowledge transferred from these studies, the application of organic molecules in silicon heterojunction solar cells is of interest [150-152]. For instance, polymeric conductor poly(3, 4-ethylenedioxythiophene):poly(styrene- sulfonate) (PEDOT:PSS) has been used widely in solar cells for a while. PEDOT:PSS has been offered as a replacement for transparent conductive oxides (TCOs) (i.e., indium tin oxide) for organic photovoltaics (OPVs) [153], or as a passivating hole selective layer in silicon heterojunction solar cells [154]. Organic molecules are mostly employed in perovskite solar cells to ensure selective charge transport at the electrodes by

modifying the interfaces and altering the work function of the charge selective contacts with the help of employing dipole moments either with electron-withdrawing or electron-donating properties [155]. Moreover, self-assembled organic molecules are employed to tune interface properties, especially in perovskite solar cell applications [156]. Organic molecules are employed as the surface modifier agents as they can create dipole at the interface [157,158]. By means of that, effective charge carrier transport can be assured at contact by barrier height modification. Studies in the literature show that self-assembled monolayer (SAM) modified ITO has better charge injection performance compared to bare ITO electrodes [159]. Self-assembly is defined as "autonomous organization of components into patterns and structures, without human intervention" [160]. Phosphonic acid-based self-assembled organic molecules are of interest in this study. The bonding of phosphonic acid to oxide with different modes is depicted in Figure 6.1.

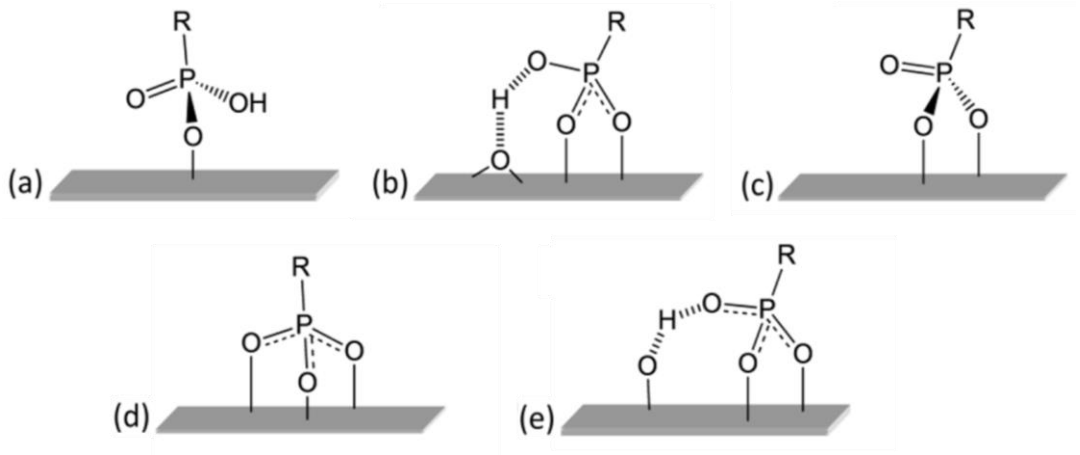

Figure 6.1 Bonding of the phosphonic acid to the surface with different modes: a) monodentate, b) bidentate with H bonding to the surface, c) bidentate, d) tridentate, e) bidentate with residual H bonding to the surface -OH group. Taken from [161].

Herein, the carrier selectivity and charge transport mechanism of self-assembled organic molecule-modified contacts are investigated. In particular, the effect of various tail and head groups on the interface engineering of the charge selective contacts is investigated. Charge selective contacts are tailored by utilizing two

different phosphonic acid-based organic molecules, namely 2PACz and FOPA. Molecular structures of the self-assembled organic molecules are depicted in Figure 6.2. While the functional anchor (head) group is phosphonic acid (-$PO(OH)_2$) for both, tail and head groups alter for each organic material. While 2PACz has a conjugated system, FOPA has a functionalized fluorinated-alkyl chain. The results and findings discussed in this chapter are based on studies conducted at Fraunhofer ISE.

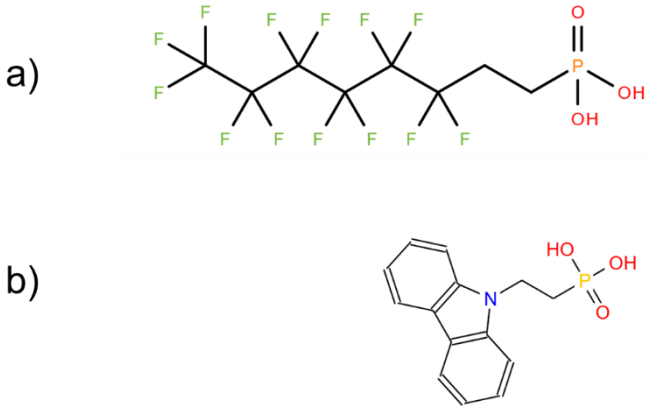

Figure 6.2 Molecular structures of organic molecules used as charge selective contacts: a) FOPA ($C_8H_6F_{13}O_3P$), b) 2PACz ($C_{14}H_{14}NO_3P$).

6.1 Self-Assembled Organic Molecule-Modified Charge Selective Contacts

6.1.1 Experimental Details

Contact resistivity (ρ_c) test structures were fabricated on shiny-etched planar n-type (p-type) FZ c-Si wafers with a resistivity of 1 Ωcm and a thickness of 200 µm (250 µm). After cleaning, Ohmic contact was ensured at the rear side of the samples either by a film of 18 nm thick, phosphorus-doped amorphous silicon (a-Si:H(n)) deposited by PECVD (INDEOtec, Octopus) or by boron/phosphorus implantation (Varian, VIISta HC). Samples were subjected to 1 minute of hydrogen fluoride (HF) dip (1%

wt.) prior to organic molecule depositions. FOPA and 2PACz were purchased from Sigma-Aldrich and TCI Chemicals, respectively. Solutions containing FOPA and 2PACz, each with a concentration of 1 mM, were prepared using tetrahydrofuran and ethanol, respectively. Solutions were stirred until organic molecules dissolved in the solution. Organic molecules were spun directly on either c-Si or 5.5 nm thick, PECVD intrinsic a-Si:H passivated c-Si, followed by hotplate annealing. Hotplate annealing was carried out to ensure the binding of molecules on c-Si, as well as evaporation of the solvents. Both spin-coating and hotplate annealing processes were carried out in ambient air. Spin-coating and hotplate annealing process parameters are given in Table 6.1. A 75 nm thick indium tin oxide (ITO) was sputtered through a shadow mask at 30 °C. 300 nm thick aluminum (Al) or silver (Ag) was thermally evaporated onto front contact through a shadow mask. Then, 300 nm thick Al was thermally evaporated as the full-area metallization on the rear side directly onto the organic molecules.

Table 6.1 Spin-coating and consecutive hotplate annealing process parameters of self-assembled molecule depositions.

Molecule	*Spin-coating (RPM)*	*Annealing temperature (°C)*	*Annealing time (min)*
FOPA	4000	80	10
2PACz	3000	100	10

Schematic cross-sections of ρ_c test structures are depicted in Figure 6.3. Besides ρ_c test structures with self-assembled molecule-modified stacks, symmetrical highly doped c-Si(p)/p+/Al and c-Si(n)/n+/Al contacts were also fabricated to be able to calculate the resistance contribution of the rear contact of the test structures. Dark I-V measurements were performed on the test structures to extract the contact resistivity and to probe the charge selectivity of the stacks containing organic molecules by using B1500A Semiconductor Device Analyzer from Keysight

Technologies. Afterwards, samples were subjected to consecutive hotplate annealing for 10 minutes at temperatures varying from 100 °C to 200 °C, followed by dark I-V measurements after each consecutive annealing step.

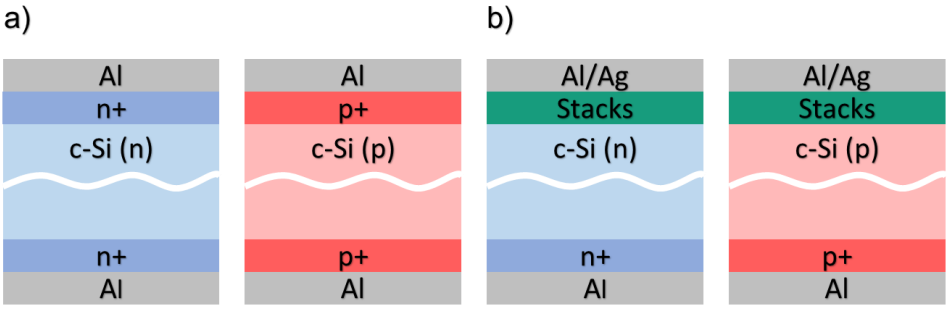

Figure 6.3 Schematic cross-sections of a) symmetrical test structures and b) ρ_c test structures on n-type and p-type c-Si for the carrier selectivity and the contact resistivity analyses.

2×2 cm^2 silicon heterojunction (SHJ) solar cells were fabricated on single-sided textured n-type FZ c-Si with a resistivity of 1 Ωcm and a thickness of 200 µm. Single-sided texturing was performed via alkaline solution on c-Si with a PECVD SiO_2/SiN_x protective capping film on the rear side of the wafers. The protective SiO_2/SiN_x film has been removed by wet chemical etching (HF dip) after random pyramidal texturing of the front side. PECVD a-Si:H(i/p) stacks with a thickness of 5.8/8.2 nm were deposited on the front side of the wafers after cleaning. Organic molecule-modified electron-selective contacts were fabricated on the rear side of the solar cells either with or without PECVD a-Si:H(i) passivation layer. Samples were subjected to 1 min of HF (1% wt.) dip prior to organic molecule depositions. Spin-coating of organic molecules, hotplate annealing, ITO and Al depositions were carried out as described above. Front side metallization was carried out via screen-printing of Ag paste, followed by curing at 130 °C. Schematic cross-sections of SHJ solar cells with organic molecule electron-selective contact are depicted in Figure 6.4. SHJ solar cells with PECVD a-Si:H(i/n) stacks with Al contact on the rear side were also fabricated as a comparison. Solar cell parameters were extracted from the light J-V

measurements. Solar cells were annealed on a hotplate in ambient air for 10 minutes to investigate the thermal stability of the solar cells. XPS measurements of the organic molecule-modified c-Si surfaces were performed in the NAP-XPS system (EnviroESCA, SPECS Surface Nano Analysis GmbH, Berlin) in a vacuum (pressure in the range of 10^{-6} – 10^{-7} mbar) at room temperature.

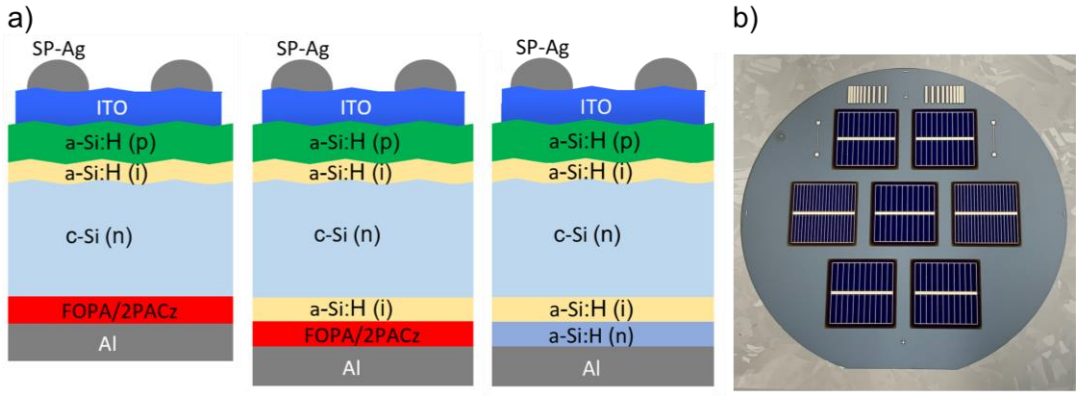

Figure 6.4 a) Schematic cross-section of SHJ solar cells with organic molecule modified electron-selective contacts b) Photograph of the front side of the organic molecule modified SHJ solar cells.

6.1.2 Results and Discussion

Both n-type and p-type c-Si with Ohmic rear contacts are fabricated to be able to examine the charge carrier selectivity of the front stacks with varied capping films. Dark I-V characteristics of the contact resistivity test structures with various front stacks capped by Al on n-type and p-type c-Si are shown in Figure 6.5a and Figure 6.5b, respectively. While Al contact on n-type c-Si shows diode behavior, both FOPA/Al and 2PACz/Al exhibit Ohmic behavior and work as electron-selective contact. It can be inferred that Schottky barrier height modification is achieved at the semiconductor/metal interface by utilizing either 2PACz/Al or FOPA/Al on n-type c-Si. On the other hand, both FOPA/Al and 2PACz/Al contact selectively block holes, as indicated by the rectifying behavior of the I-V curves on p-type c-Si.

Additionally, a-Si:H(i) (denoted as i) film between the c-Si and the self-assembled molecules deteriorates Ohmic contact, as shown by S-shaped I-V curves in Figure 6.5a.

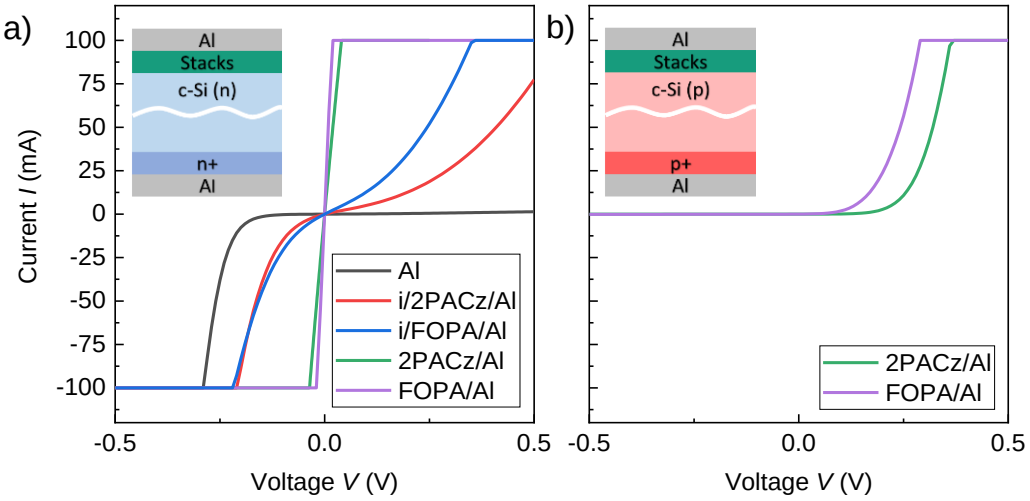

Figure 6.5 Dark I-V characteristics of the contact resistivity test structures for varied stacks capped by Al on (a) n-type c-Si and (b) p-type c-Si.

Contact resistivity of front stacks with varied capping films and metal electrodes is shown in Figure 6.6. The contact resistivity was extracted from the total resistance of the test structures measured by two terminal dark I-V measurements. The total resistance of the samples was calculated by linear regression at zero voltage. Symmetrical c-Si(p)/p+/Al and c-Si(n)/n+/Al samples were fabricated to calculate the resistivity contribution of the rear contacts. Contact resistivity of the rear a-Si:H(n)/Al contact alters between 118 mΩcm^2 and 350 mΩcm^2 depending on the hotplate annealing temperature (i.e., the contact is improved by hotplate annealing temperature up to 175 °C). Contact resistivity values of the front stacks from which the resistivity contributions of the rear contact and the base are subtracted are reported. More information on the contact resistivity analysis can be found in the article previously published [162]. With respect to direct Al contact, three orders of magnitude ρ_c improvement are achieved by implementing 2PACz/Al and FOPA/Al

contacts on n-type c-Si with an average ρ_c of 244 mΩcm^2 and 227 mΩcm^2, respectively. Although ρ_c is improved by 2PACz/Ag and FOPA/Ag contacts compared to Ag contact, Ag capping reduces the performance of electron-selective contacts, increasing ρ_c. Utilizing low work function metal at the electron-selective contact induces downward bending at the surface of c-Si, thus reducing the effective barrier height [157,163,164]. Therefore, the electron-selective contacts are expected to perform better with Al, which has a lower work function than Ag. Although lower ρ_c values are obtained with FOPA/ITO/Al compared to ITO/Al contact, ITO film either on FOPA or on 2PACz leads to an S-shaped I-V curve which indicates rectifying behavior (i.e., like i/2PACz/Al and i/FOPA/Al contacts). Moreover, sputtered ITO was replaced with thermal-ALD deposited aluminum zinc oxide (AZO), resulting in similar rectifying behavior as sputtered ITO. The change in charge selectivity depending on the capping metal has also been reported in the literature for various materials [165]. This is attributed to the carrier selective contacts with low carrier density. In conclusion, they primarily modify the work function rather than implementing charge selectivity.

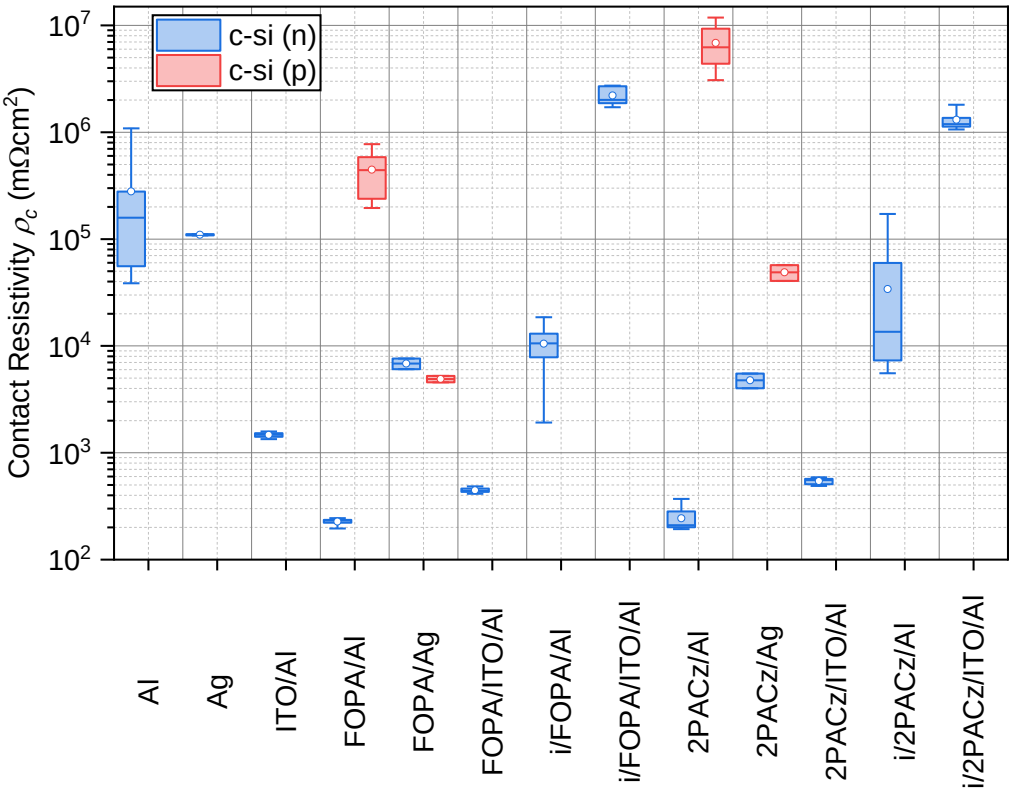

Figure 6.6 Screening FOPA and 2PACz contact resistivity for various stacks and metals on n-type and p-type c-Si contact resistivity test structures.

The evolution of contact resistivity of FOPA and 2PACz modified electron-selective contacts upon subsequent annealing step is shown in Figure 6.7. The red dashed line on the graph corresponds to the maximum level of contact resistance for the effective operation of SHJ solar cells when full-area contacts are employed. Both FOPA/Al and 2PACz/Al contacts are stable upon annealing up to 200 °C. Moreover, they are still stable after six months of storage in ambient air. It is promising that organic-based electron-selective contacts are stable upon annealing, and they are stable even after six months of storage in ambient air, which is unlikely for most organic materials.

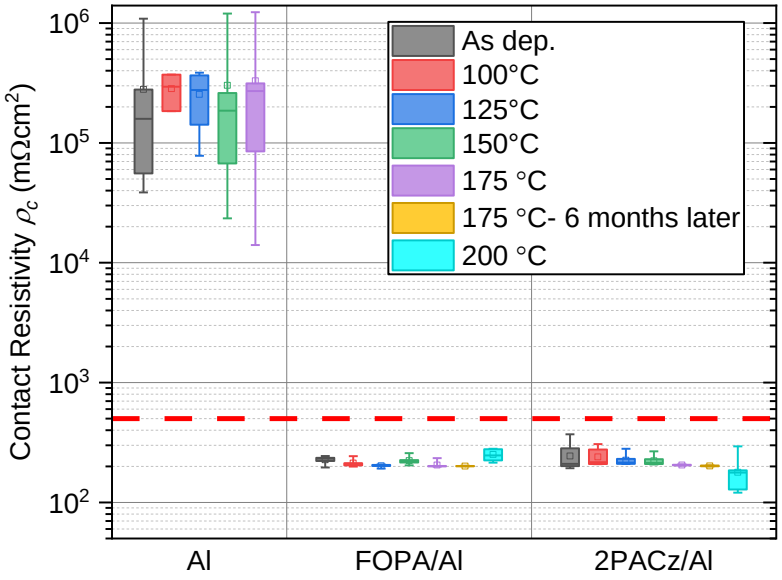

Figure 6.7 Stability of contact resistivity for FOPA/Al and 2PACz/Al contacts after hotplate annealing and storage under ambient air.

Considering the best performing contact resistivity test structures, Al is used at the rear side of the solar cells, including reference SHJ solar cells with a-Si:H(i/n) contacts. Moreover, the rear surface is designed to be planar for all the solar cells to avoid poor adhesion or inhomogeneity of self-assembled molecules. J-V results for the active area of self-assembled organic molecule modified SHJ solar cells, compared to SHJ solar cells with a-Si:H(i/n) electron-selective contacts capped by Al (denoted as i/n/Al) are given in Figure 6.8 for the active area of the SHJ solar cells. Conversion efficiencies of the solar cells increase by implementing both FOPA and 2PACz between Al and c-Si(n) compared to direct Al contact. Better solar cell performance is achieved with FOPA/Al contact than with 2PACz/Al. Despite having promising implied-open-circuit voltage iV_{oc} values (726 mV and 724 mV shown by dotted red lines in Figure 6.8a for i/FOPA and i/2PACz, respectively), the performance of the solar cells deteriorates by the implementation of a-Si:H(i) passivation film between the molecules and c-Si. Degradation of a-Si:H(i) layer during spin-coating or consecutive annealing steps is not observed. Thus, the

significant difference between iV_{oc} and V_{oc} is attributed to a problem of carrier selectivity rather than passivation. This is confirmed by the non-Ohmic behavior of the contact resistivity test structures shown above. Therefore, a decrease in V_{oc}, FF, and η is observed when a-Si:H(i) layer is introduced. Although the values of V_{oc}, FF, and η tend to increase with decreasing ρ_c, why J_{sc} values are out of this trend requires further investigation. Charge carrier separation and extraction problems of organic molecule modified charge selective contacts can be attributed to the nature of the organic molecules. Contrary to inorganic charge transport layers, excited electron-hole pairs are known to be localized in the molecule (i.e., Frenkel-excitons). Therefore, free charge carriers cannot be extracted from the molecules in the case of Frenkel excitons, where exciton diffusion length is in the order of a few nm [166]. Moreover, to construct a charge selective contact, both asymmetry in electron and hole conductivities and an energy barrier to the one type of carriers (via band alignment) should be ensured, which is typically challenging by utilizing organic materials.

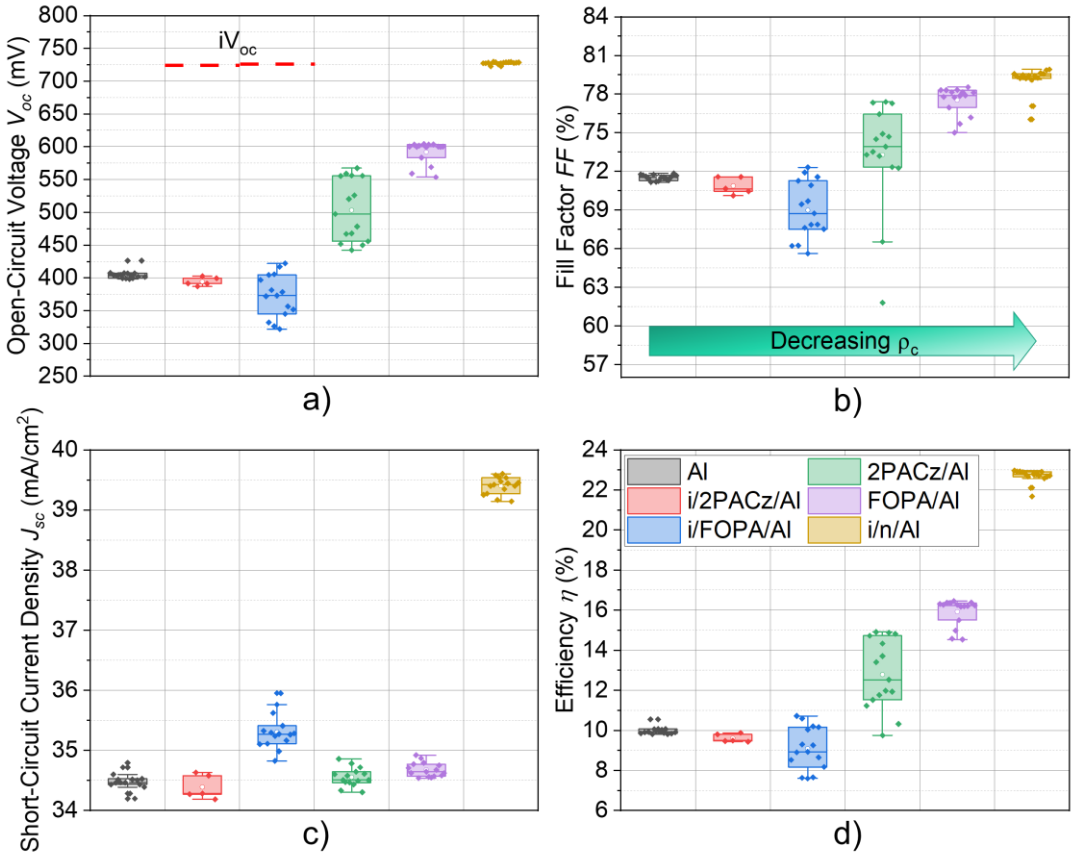

Figure 6.8 Light J-V measurements of SHJ solar cells: a) Open-circuit voltage, b) fill factor, c) short-circuit current density, d) power conversion efficiency.

J-V characteristics of the SHJ solar cells under illumination are shown in Figure 6.9. S-shaped J-V curves are not observed for any of the samples. As a result, *FF* values are at a reasonable level, and the performance of the solar cells is limited mainly by selective carrier extraction.

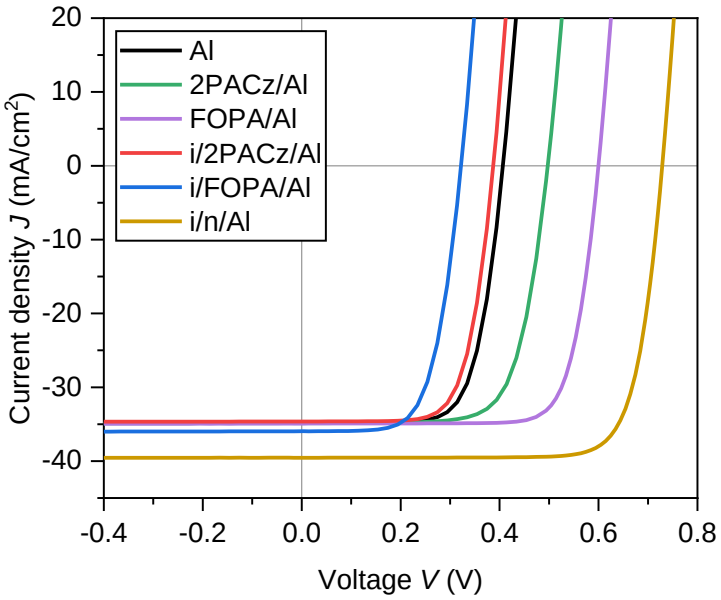

Figure 6.9 J-V characteristics of the SHJ solar cells under illumination.

J-V measurements are carried out to investigate the stabilities of solar cells after hotplate annealing and storage under ambient air. Solar cells stored under ambient air for three weeks yield identical results to the initial measurements. Afterward, solar cells were subjected to consecutive hotplate annealing for 10 min at 150 °C, 175 °C, and 200 °C. J-V measurements of the solar cells in the as-deposited state and after hotplate annealing at 175 °C and 200 °C are shown in Figure 6.10. After annealing at 150 °C, a slight performance loss is observed for the solar cells with 2PACz/Al contact, while the performance of the solar cells with FOPA/Al contact remains the same. On the other hand, a slight increase in *FF*, V_{oc}, and η is observed for the reference solar cell with i/n/Al contact as a result of improvement in series resistance and passivation. These results after annealing at 150 °C are not shown in Figure 6.10 to avoid clutter. The conversion efficiency of the solar cells with 2PACz/Al contact decreases upon annealing. Solar cells with i/n/Al contact improve with annealing at 175 °C. However, severe degradation of the solar cells with i/n/Al contact is observed after annealing at 200 °C. Degradation of the solar cells with

i/n/Al contact can be attributed to the aluminum diffusion into the underlying a-Si:H(i)/a-Si:H(n) stack at elevated temperatures, which is pronounced especially for thin a-Si:H(i)/a-Si:H(n) films reported in the literature [167]. A thicker a-Si:H(i)/a-Si:H(n) stack would be a solution to avoid Si-Al interdiffusion at the electron-selective contact. Solar cells with FOPA/Al electron-selective contact are stable even at 200 °C, at which solar cells with i/n/Al stack degrade. The best-performing solar cell is obtained by FOPA/Al electron-selective contact with a stable conversion efficiency of 16.5%.

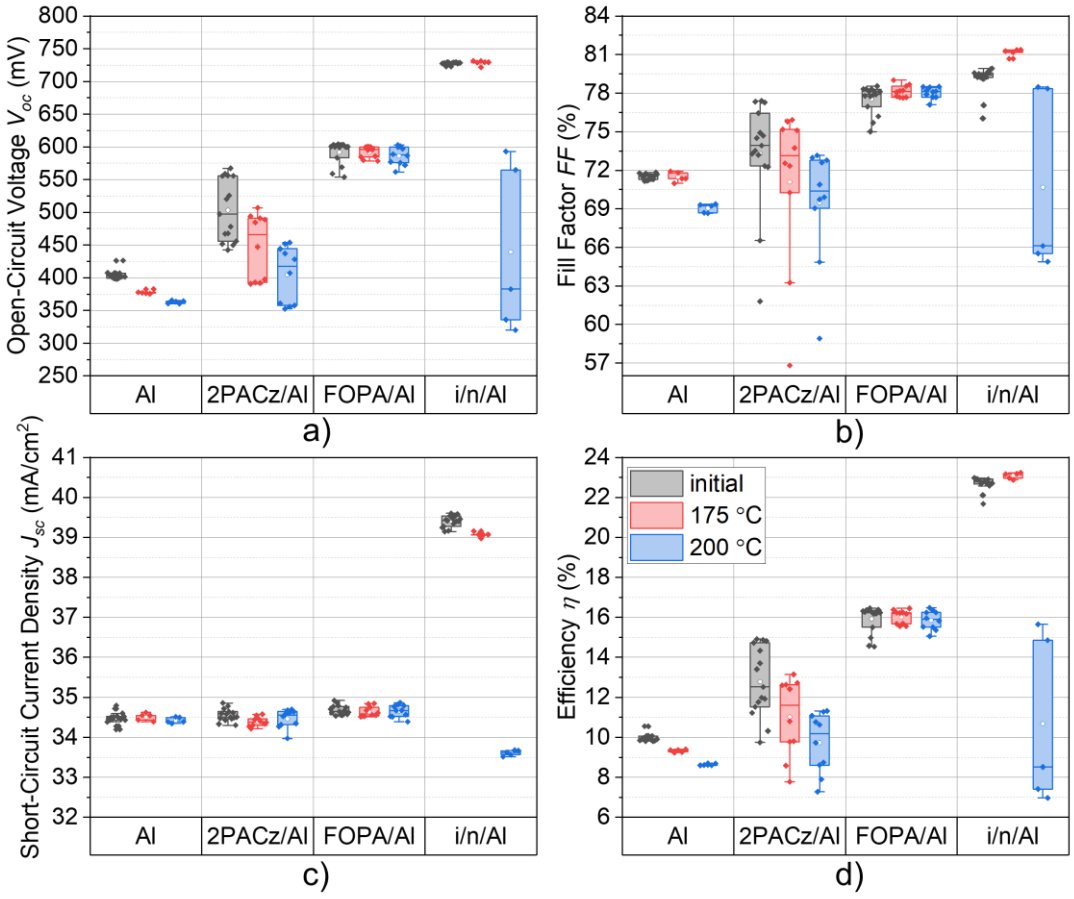

Figure 6.10 Evolution of SHJ solar cell parameters as a function of annealing temperature: (a) Open-circuit voltage, (b) fill factor, (c) short-circuit current density, (d) power conversion efficiency.

External quantum efficiency (EQE) and reflectance spectra of SHJ solar cells are shown in Figure 6.11. There is not a significant reflectance difference between the SHJ solar cells. However, EQE significantly reduces in the IR region by utilizing Al, 2PACz/Al, and FOPA/Al contacts.

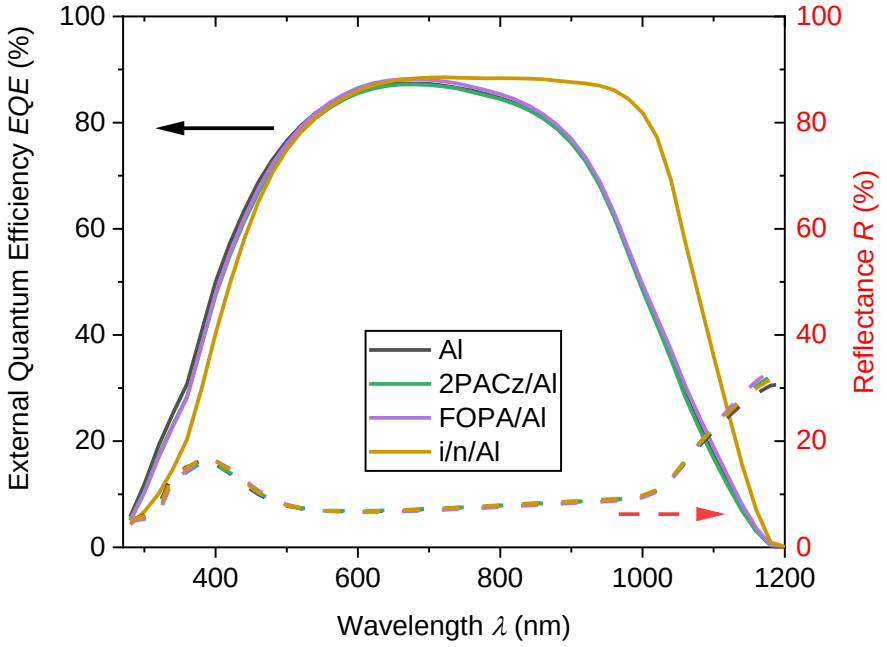

Figure 6.11 External quantum efficiency and the corresponding reflectance spectra of the SHJ solar cells with varied electron-selective contacts.

The elemental composition of self-assembled organic molecule-coated samples is analyzed by XPS measurement. The survey spectra of the organic molecule deposited samples compared to the c-Si substrate, and the corresponding peaks are shown in Figure 6.12.

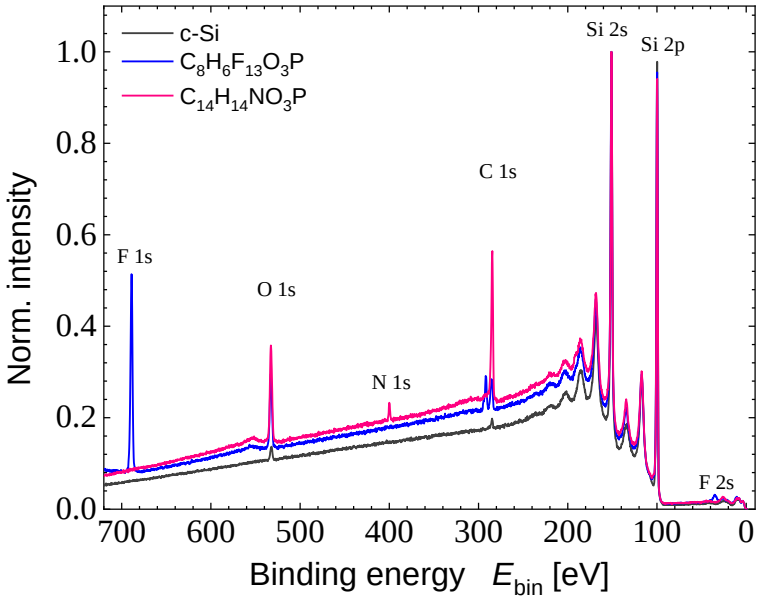

Figure 6.12 The survey spectra of the substrate and organic molecule deposited surfaces.

The fit of high-resolution C 1s and O 1s core spectra gives the different chemical states of carbons and oxygens present on the surface. Compositions of the sample surfaces are given in Table 6.2. The presence of self-assembled organic layers on c-Si is demonstrated.

Table 6.2 Composition of the sample surface given in atomic %.

Sample	*Si (%)*	*C (%)*	*O (%)*	*N (%)*	*F (%)*
c-Si (ref)	96.63	1.84	1.53	-	-
FOPA ($C_8H_6F_{13}O_3P$)	65.75	13.81	6.74	-	13.7
2PACz ($C_{14}H_{14}NO_3P$)	62.71	27.71	8.26	1.32	-

Curve fitting of O 1s peak with high-resolution data acquisition reveals the chemical states of the oxygen on the surface. The amount of chemical states of O is given in Table 6.3. There is a significant difference in the total fraction of SiO_2 present on the surface, which can indicate the surface coverage of each organic material on c-Si. The presence of more PO_3 on c-Si with FOPA can be attributed to the better contact resistivity and better performance of FOPA/Al contacts compared to 2PACz/Al. On the other hand, the significant difference in the amount of OH gives information about the bonding of the phosphonic acid to the surface with different modes. The binding of the phosphonic acid group of FOPA to c-Si can preferably be bidentate or tridentate. However, increased OH amount for 2PACz indicates that the binding of phosphonic acid might be monodentate and bidentate with either H bonding to the surface or residual H bonding. These bonding mechanisms are valid, assuming self-assembled monolayers exist on c-Si by utilizing both FOPA and 2PACz. However, there is no experimental evidence for the self-assembled monolayer formation.

Table 6.3 Chemical states of O on FOPA and 2PACz deposited c-Si surfaces

Sample	*OH (%)*	*SiO_2 (%)*	*PO_3 (%)*
FOPA ($C_8H_6F_{13}O_3P$)	0.4	26.5	73.1
2PACz ($C_{14}H_{14}NO_3P$)	10.3	39.0	50.7

6.1.3 Conclusion

Novel organic material-based electron-selective contacts that can replace doped a-Si:H films are proposed. Charge selectivity and contact resistivity properties of the organic molecule modified contacts are investigated depending on the capping electrode. Considering the poor stability of organic materials in general, a good level

of stability is reported in terms of thermal treatments and storage under ambient air. SHJ solar cells via FOPA and 2PACz modified electron contacts are fabricated. It is reported that FOPA electron-selective contacts outperform compared to 2PACz, with a power conversion efficiency of 16.5%. The reason FOPA has better results can be associated with the presence of more organic material on the c-Si surface as a result of the material analysis.

CHAPTER 7

CONCLUSION AND OUTLOOK

The application of thermal and plasma-ALD Al_2O_3 films with various oxidants was demonstrated, and the effect of oxidant choice on the silicon surface passivation was systematically investigated by post-annealing treatments. Ozone concentration-dependent thermal-ALD Al_2O_3 deposition was optimized. Moreover, the stability of ozone-based thermal-ALD Al_2O_3 deposited samples and Al_2O_3/PECVD SiN_x stacks with varied post-deposition thermal treatments were presented. Tuning the ALD parameters is more crucial for a single Al_2O_3 layer when FGA is utilized to activate surface passivation. Al_2O_3 films showing poor passivation quality were improved to some extent by the SiN_x capping layer. Although the blistering is more likely present on Al_2O_3/SiN_x stacks after being fired at elevated temperatures, blister-free Al_2O_3/SiN_x stacks were obtained with suitable deposition parameters. Hence, blister-free Al_2O_3/SiN_x stacks fired at high temperatures allow for an effective lifetime of 1.5 ms and iV_{oc} of 730 mV when optimized ozone-based ALD Al_2O_3 deposition parameters are applied. Therefore, it can provide an industrial roadmap for simplified fabrication of blister-free rear side passivation of PERC solar cells.

Fabrication of black silicon via ICP-RIE and its implementation in PERC solar cells was demonstrated. Although the generation rate of the carriers is improved using b-Si compared to random pyramidal textured c-Si solar cells with higher reflectance, collection probability decreases significantly for b-Si solar cells, which reduces the light-generated current of the device. To this extent, a roadmap to improve the power conversion efficiency of b-Si solar cells was demonstrated. It is concluded that the best strategy to obtain high efficiency in b-Si solar cells is to facilitate metal contact on b-Si by employing low aspect ratio nanostructures rather than minimizing the optical reflectance. Electrical losses were minimized to some extent by achieving better screen-printing of Ag fingers on the nanostructured b-Si surfaces. The best

performing b-Si solar cell has been fabricated with a conversion efficiency of 19.7% with a total weighted average reflection below 5% after nanotexturing via RIE.

To improve b-Si solar cells, it is also required to reduce recombination losses by adopting conformal passivation on the nanostructures, such as implementing ALD instead of PECVD. With the help of the self-terminating nature of the ALD technique, more conformal deposition can be ensured on high aspect ratio nanostructured surfaces. Therefore, better V_{oc} can be achieved with b-Si solar cells. Moreover, b-Si solar cell fabrication is also challenging as resistive losses are significant because of difficulties in having proper metal contact formation on b-Si. Novel methods, such as micro-grid design for metallization, are proposed to tackle this problem, which would ease the charge extraction, and increase the fill factor by reducing series resistance. Furthermore, to overcome the adhesion problem of the metal on b-Si by screen-printing method, electro-plating can be a suitable metallization technique on b-Si since it is known to perform better on porous structures. Once the surface recombination is suppressed for b-Si, thinner c-Si wafers can be utilized for b-Si solar cell applications since b-Si enables improved light coupling into the solar cell. This, in turn, reduces the cost of the solar cell and nonradiative bulk recombination in the solar cell.

A systematic study on organic molecule-modified electron-selective contacts by implementing phosphonic acid-based self-assembled organic molecules was presented. Charge selectivity properties of FOPA and 2PACz modified contacts in combination with varied capping layers were investigated. Charge selectivity and contact resistivity of the contacts are sensitive to the electrode since the work function of the capping metal affects Schottky barrier height. Three orders of magnitude contact resistivity improvement were achieved by FOPA/Al and 2PACz/Al contacts (ρ_c of 227 mΩcm^2 and 244 mΩcm^2, respectively) compared to Al contact (ρ_c of 2.8×10^5 mΩcm^2). Interfacial engineering of electron-selective contacts on SHJ solar cells via FOPA and 2PACz was demonstrated. The performance of SHJ solar cells with organic molecule-modified electron-selective contacts was improved with decreasing ρ_c. Thermally stable SHJ solar cells with

FOPA/Al electron-selective contacts were fabricated, resulting in a power conversion efficiency of 16.5%. The main challenges of organic molecule applications on c-Si are maintaining excellent surface passivation of c-Si without compromising charge selectivity (i.e., by utilizing thinner a-Si:H(i) film) and providing strong dipole moment via organic molecules.

As a future aspect of employing of the organic molecules in hybrid silicon heterojunction solar cells, a good strategy would be to find or synthesize a suitable organic material to provide both energy level alignment at the interface and band bending in c-Si. This enables the collection of charge carriers effectively. Future studies on organic/inorganic hybrid structures should be focused on understanding the effect of the interface and hence dipole moment creation on the charge carrier extraction and the surface passivation mechanisms. Moreover, organic materials which have matching band alignment with c-Si can be investigated or synthesized for better charge carrier selectivity. The effect of electron-donating and electron-withdrawing substituents on organic molecule/silicon interface, passivation, and charge extraction properties should be investigated in detail.

REFERENCES

[1] "bp Statistical Review of World Energy 2021," 2022.

[2] L. Partain and L. Fraas, *Solar Cells And Their Applications*. 2010.

[3] D. M. Chapin, C. S. Fuller, and G. L. Pearson, "A New Silicon p-n Junction Photocell for Converting Solar Radiation into Electrical Power," *J. Appl. Phys.*, vol. 25, p. 676, 1954.

[4] H. Seidel, L. Csepregi, A. Heuberger, and H. Baumgärtel, "Anisotropic Etching of Crystalline Silicon in Alkaline Solutions: I. Orientation Dependence and Behavior of Passivation Layers," *J. Electrochem. Soc.*, vol. 137, p. 3626, 1990.

[5] H. Jansen, M. de Boer, R. Legtenberg, and M. Elwenspoek, "The black silicon method: a universal method for determining the parameter setting of a fluorine-based reactive ion etcher in deep silicon trench etching with profile control," *J. Micromechanics Microengineering*, vol. 5, p. 115, 1995.

[6] M. Otto, "Passivation of Black Silicon Surfaces with ALD Deposited Al_2O_3," 2015.

[7] E. Yablonovitch, "Statistical ray optics," *J. Opt. Soc. Am.*, vol. 72, no. 7, pp. 899–907, 1982.

[8] F. Flory, L. Escoubas, J. Le Rouzo, and G. Berginc, "Nanophotonics: From Funfdamental Research to Applications," in *Micro- and Nanophotonic Technologies*, P. Meyrueis, Ka. Sakoda, and M. Van de Voorde, Eds. 2017.

[9] Y. Xia, B. Liu, S. Zhong, and C. Li, "X-ray photoelectron spectroscopic studies of black silicon for solar cell," *J. Electron Spectros. Relat. Phenomena*, vol. 184, pp. 589–592, 2012.

[10] H. V. Jansen *et al.*, "Black silicon method XI: Oxygen pulses in SF_6

plasma," *J. Micromechanics Microengineering*, vol. 20, p. 075027, 2010.

[11] G. S. Oehrlein and Y. Kurogi, "Sidewall surface chemistry in directional etching processes," *Mater. Sci. Eng. R Reports*, vol. 24, no. 4, pp. 153–183, 1998.

[12] V. A. Yunkin, D. Fischer, and E. Voges, "Reactive ion etching of silicon submicron-sized trenches in $SF_6/C_2Cl_3F_3$ plasma," *Microelectron. Eng.*, vol. 27, pp. 463–466, 1995.

[13] R. Legtenberg, H. Jansen, M. Deboer, and M. Elwenspoek, "Anisotropic Reactive Ion Etching of Silicon Using $SF_6/O_2/CHF_3$ Gas Mixtures," *J. Electrochem. Soc.*, vol. 142, no. 6, pp. 2020–2028, 1995.

[14] B. Ã. Prasad, S. Bhattacharya, A. K. Saxena, S. R. Reddy, and R. K. Bhogra, "Performance enhancement of mc-Si solar cells due to synergetic effect of plasma texturization and SiN_x:H AR coating," *Sol. Energy Mater. Sol. Cells*, vol. 94, no. 8, pp. 1329–1332, 2010.

[15] S. M. Sze, *Physics of Semiconductor Devices*. John Wiley & Sons, Ltd, 1981.

[16] P. Würfel, *Physics of Solar Cells From Principles to New Concepts*. Wiley-VCH, 2005.

[17] T. Suntola and J. Antson, "Method for producing compound thin films," 1977.

[18] R. W. Johnson, A. Hultqvist, and S. F. Bent, "A brief review of atomic layer deposition: From fundamentals to applications," *Mater. Today*, vol. 17, no. 5, pp. 236–246, 2014.

[19] C. Reichel, "Decoupling Charge Carrier Collection and Metallization Geometry of Back-Contacted Back-Junction Silicon Solar Cells," 2012.

[20] D. Payne *et al.*, "Rapid Optical Modelling of Plasma Textured Silicon," in

European Photovoltaic Solar Energy Conference 2017, 2017, pp. 897–901.

[21] R. A. Sinton and A. Cuevas, "Contactless determination of current-voltage characteristics and minority-carrier lifetimes in semiconductors from quasi-steady-state photoconductance data," *Appl. Phys. Lett.*, vol. 69, pp. 2510–2512, 1996.

[22] B. Vermang *et al.*, "Blistering in ALD Al_2O_3 passivation layers as rear contacting for local Al BSF Si solar cells," *Sol. Energy Mater. Sol. Cells*, vol. 101, pp. 204–209, 2012.

[23] A. Richter *et al.*, "Thermal Stability of Spatial ALD Deposited Al_2O_3 Capped by PECVD SiN_x for the Passivation of Lowly- and Highly-Doped P-Type Silicon Surfaces," in *27th European Photovoltaic Solar Energy Conference and Exhibition, Frankfurt, Germany*, 2012, pp. 1133–1137.

[24] S. Bordihn, V. Mertens, J. W. Müller, and W. M. M. (Erwin) Kessels, "Deposition temperature dependence of material and Si surface passivation properties of O_3-based atomic layer deposited Al_2O_3-based films and stacks," *J. Vac. Sci. Technol. A Vacuum, Surfaces, Film.*, vol. 32, p. 01A128, 2014.

[25] B. Vermang *et al.*, "On the blistering of Al_2O_3 passivation layers for Si solar cells," in *26th European Photovoltaic Solar Energy Conference and Exhibition, Hamburg, Germany*, 2011, p. 1129.

[26] P. Repo, H. Talvitie, S. Li, J. Skarp, and H. Savin, "Silicon surface passivation by Al_2O_3: Effect of ALD reactants," in *SiliconPV 2011, 1st International Conference on Crystalline Silicon Photovoltaics, Energy Procedia*, 2011, vol. 8, pp. 681–687.

[27] G. Von Gastrow, S. Li, P. Repo, Y. Bao, M. Putkonen, and H. Savin, "Ozone-based batch atomic layer deposited Al_2O_3 for effective surface passivation," in *SiliconPV 2013, 3rd International Conference on Crystalline Silicon Photovoltaics, Energy Procedia*, 2013, vol. 38, pp. 890–

894.

[28] G. Von Gastrow, S. Li, M. Putkonen, M. Laitinen, T. Sajavaara, and H. Savin, “Effect of ozone concentration on silicon surface passivation by atomic layer deposited Al_2O_3,” *Appl. Surf. Sci.*, vol. 357, pp. 2402–2407, 2015.

[29] J. Mullins *et al.*, “Thermally activated defects in float zone silicon: Effect of nitrogen on the introduction of deep level states,” *J. Appl. Phys.*, vol. 124, p. 035701, 2018.

[30] “Atlas ozone generator webpage ref.” [Online]. Available: https://absoluteozone.com/products/industrial-ozone-generators/atlas-30-models/atlas-30/.

[31] B. Hoex, J. J. H. Gielis, M. C. M. Van De Sanden, and W. M. M. Kessels, “On the c-Si surface passivation mechanism by the negative-charge-dielectric Al_2O_3,” *J. Appl. Phys.*, vol. 104, p. 113703, 2008.

[32] G. Dingemans, N. M. Terlinden, D. Pierreux, H. B. Profijt, M. C. M. Van De Sanden, and W. M. M. Kessels, “Influence of the oxidant on the chemical and field-effect passivation of Si by ALD Al_2O_3,” *Electrochem. Solid-State Lett.*, vol. 14, no. 1, p. H1, 2011.

[33] C. Barbos *et al.*, “Characterization of Al_2O_3 Thin Films Prepared by Thermal ALD,” in *5th International Conference on Silicon Photovoltaics, SiliconPV 2015 Energy Procedia*, 2015, vol. 77, pp. 558–564.

[34] A. Ek, “Silicon Surface Passivation via Ultra-Thin SiO_2, TiO_2, and Al_2O_3 Layers,” 2019.

[35] J. A. Giesecke, M. C. Schubert, B. Michl, F. Schindler, and W. Warta, “Minority carrier lifetime imaging of silicon wafers calibrated by quasi-steady-state photoluminescence,” *Sol. Energy Mater. Sol. Cells*, vol. 95, pp. 1011–1018, 2011.

[36] F. Restrepo and C. E. Backus, “On Black Solar Cells or the Tetrahedral Texturing of a Silicon Surface,” *IEEE Trans. Electron Devices*, vol. 23, no. 10, pp. 1195–1197, 1976.

[37] Y. F. Huang *et al.*, “Improved broadband and quasi-omnidirectional anti-reflection properties with biomimetic silicon nanostructures,” *Nat. Nanotechnol.*, vol. 2, pp. 770–774, 2007.

[38] T. Tsang, A. Bolotnikov, A. Haarahiltunen, and J. Heinonen, “Quantum efficiency of black silicon photodiodes at VUV wavelengths,” *Opt. Express*, vol. 28, no. 9, p. 13299, 2020.

[39] M. Garin *et al.*, “Black-Silicon Ultraviolet Photodiodes Achieve External Quantum Efficiency above 130%,” *Phys. Rev. Lett.*, vol. 125, no. 11, p. 117702, 2020.

[40] M. A. Juntunen, J. Heinonen, V. Vähänissi, P. Repo, D. Valluru, and H. Savin, “Near-unity quantum efficiency of broadband black silicon photodiodes with an induced junction,” *Nat. Photonics*, vol. 10, pp. 777–782, 2016.

[41] M. Steglich *et al.*, “A normal-incidence PtSi photoemissive detector with black silicon light-trapping,” *J. Appl. Phys.*, vol. 114, p. 183102, 2013.

[42] Z. Huang, J. E. Carey, M. Liu, X. Guo, E. Mazur, and J. C. Campbell, “Microstructured silicon photodetector,” *Appl. Phys. Lett.*, vol. 89, p. 033506, 2006.

[43] M. U. Pralle *et al.*, “Black silicon enhanced photodetectors: a path to IR CMOS,” in *Infrared Technology and Applications XXXVI*, vol. 7660, no. May 2010, p. 76600N.

[44] T. Zhang *et al.*, “Optical and Electronic Properties of Femtosecond Laser-Induced Sulfur-Hyperdoped Silicon N+/P Photodiodes,” *Nanoscale Res. Lett.*, vol. 12:522, 2017.

[45] H. Jansen, M. de Boer, and M. Elwenspoek, “The black silicon method VI: High aspect ratio trench etching for MEMS applications,” in *Proceedings of Ninth International Workshop on Micro Electromechanical Systems*, 1996, pp. 250–257.

[46] G. Barillaro, A. Nannini, and M. Piotto, “Electrochemical etching in HF solution for silicon micromachining,” *Sensors Actuators A Phys.*, vol. 102, pp. 195–201, 2002.

[47] V. Mulloni and L. Pavesi, “Porous silicon microcavities as optical and electrical chemical sensors,” *Appl. Phys. Lett.*, vol. 76, p. 2523, 2000.

[48] M. G. Berger *et al.*, “Porosity superlattices: a new class of Si heterostructures,” *J. Phys. D. Appl. Phys.*, vol. 27, pp. 1333–1336, 1994.

[49] M. G. Berger *et al.*, “Investigation and design of optical properties of porosity superlattices,” *Thin Solid Films*, vol. 255, pp. 313–316, 1995.

[50] V. Torres-Costa and R. J. Martín-Palma, “Application of nanostructured porous silicon in the field of optics. A review,” *J. Mater. Sci.*, vol. 45, pp. 2823–2838, 2010.

[51] L. Pavesi, C. Mazzoleni, A. Tredicucci, and V. Pellegrini, “Controlled photon emission in porous silicon microcavities,” *Appl. Phys. Lett.*, vol. 67, p. 3280, 1995.

[52] P. Hoyer, M. Theuer, R. Beigang, and E. B. Kley, “Terahertz emission from black silicon,” *Appl. Phys. Lett.*, vol. 93, p. 091106, 2008.

[53] M. S. Schmidt, J. Hübner, and A. Boisen, “Large area fabrication of leaning silicon nanopillars for Surface Enhanced Raman Spectroscopy,” *Adv. Opt. Mater.*, vol. 24, pp. OP11–OP18, 2012.

[54] Y. L. Deng and Y. J. Juang, “Black silicon SERS substrate: Effect of surface morphology on SERS detection and application of single algal cell analysis,” *Biosens. Bioelectron.*, vol. 53, pp. 37–42, 2014.

[55] G. Seniutinas *et al.*, “Versatile SERS sensing based on black silicon,” *Opt. Express*, vol. 23, no. 5, p. 6763, 2015.

[56] Z. Ma, C. Jiang, W. Yuan, and Y. He, “Large-scale Patterning of Hydrophobic Silicon Nanostructure Arrays Fabricated by Dual Lithography and Deep Reactive Ion Etching,” *Nano-Micro Lett.*, vol. 5, no. 1, pp. 7–12, 2013.

[57] G. Sun, T. Gao, X. Zhao, and H. Zhang, “Fabrication of micro/nano dual-scale structures by improved deep reactive ion etching,” *J. Micromechanics Microengineering*, vol. 20, p. 075028, 2010.

[58] D. Lee, D. Pyo, C. Cho, and B. Kim, “Effects on micropyramid and nanoneedle structures for superhydrophobicity on Si surface,” *Vacuum*, vol. 131, pp. 188–193, 2016.

[59] M. Barberoglou, V. Zorba, A. Pagozidis, C. Fotakis, and E. Stratakis, “Electrowetting properties of micro/nanostructured black silicon,” *Langmuir*, vol. 26, no. 15, pp. 13007–13014, 2010.

[60] J. Zhu, C. M. Hsu, Z. Yu, S. Fan, and Y. Cui, “Nanodome solar cells with efficient light management and self-cleaning,” *Nano Lett.*, vol. 10, pp. 1979–1984, 2010.

[61] Y. Liu, A. Das, Z. Lin, I. B. Cooper, A. Rohatgi, and C. P. Wong, “Hierarchical robust textured structures for large scale self-cleaning black silicon solar cells,” *Nano Energy*, vol. 3, pp. 127–133, 2014.

[62] D. Qi *et al.*, “Simple approach to wafer-scale self-cleaning antireflective silicon surfaces,” *Langmuir*, vol. 25, no. 14, pp. 7769–7772, 2009.

[63] E. P. Ivanova *et al.*, “Bactericidal activity of black silicon,” *Nat. Commun.*, vol. 4, p. 2838, 2013.

[64] J. H. Park, L. Gu, G. Von Maltzahn, E. Ruoslahti, S. N. Bhatia, and M. J. Sailor, “Biodegradable luminescent porous silicon nanoparticles for in vivo

applications," *Nat. Mater.*, vol. 8, pp. 331–336, 2009.

[65] J. Salonen, A. M. Kaukonen, J. Hirvonen, and V. P. Lehto, "Mesoporous silicon in drug delivery applications," *J. Pharm. Sci.*, vol. 97, no. 2, pp. 632–653, Feb. 2008.

[66] L. Wang, V. Reipa, and J. Blasic, "Silicon Nanoparticles as a Luminescent Label to DNA," *Bioconjug. Chem.*, vol. 15, pp. 409–412, 2004.

[67] M. P. Stewart and J. M. Buriak, "Chemical and biological applications of porous silicon technology," *Adv. Mater.*, vol. 12, no. 12, pp. 859–869, 2000.

[68] L. De Stefano *et al.*, "Optical Sensors for Vapors, Liquids, and Biological Molecules Based on Porous Silicon Technology," *IEEE Trans. Nanotechnol.*, vol. 3, no. 1, pp. 49–54, 2004.

[69] M. Hassen *et al.*, "Performance improvements of crystalline silicon by iterative gettering process for short duration and with the use of porous silicon as sacrificial layer," *Sol. Energy Mater. Sol. Cells*, vol. 87, pp. 493–499, 2005.

[70] T. P. Pasanen, H. S. Laine, V. Vähänissi, J. Schön, and H. Savin, "Black silicon significantly enhances phosphorus diffusion gettering," *Sci. Rep.*, vol. 8, no. 1991, 2018.

[71] S. Fan, M. G. Chapline, N. R. Franklin, T. W. Tombler, A. M. Cassell, and H. Dai, "Self-oriented regular arrays of carbon nanotubes and their field emission properties," *Science (80-.).*, vol. 283, no. 5401, pp. 512–514, 1999.

[72] M. Ge, X. Fang, J. Rong, and C. Zhou, "Review of porous silicon preparation and its application for lithium-ion battery anodes," *Nanotechnology*, vol. 24, p. 422001, 2013.

[73] A. Vu, Y. Qian, and A. Stein, "Porous Electrode Materials for Lithium-Ion Batteries – How to Prepare Them and What Makes Them Special," *Adv. Energy Mater.*, vol. 2, pp. 1056–1085, 2012.

[74] J. Oh, T. G. Deutsch, H. C. Yuan, and H. M. Branz, “Nanoporous black silicon photocathode for H_2 production by photoelectrochemical water splitting,” *Energy Environ. Sci.*, vol. 4, pp. 1690–1694, 2011.

[75] A. Serpenguzel, A. Kurt, I. Inanç, J. E. Cary, and E. Mazur, “Luminescence of black silicon,” *J. Nanophotonics*, vol. 2, p. 021770, 2008.

[76] A. Zukauskas *et al.*, “Black silicon: substrate for laser 3D micro/nano-polymerization,” *Opt. Express*, vol. 21, no. 6, p. 6901, 2013.

[77] L. X. Yang, Y. M. Chao, L. Jia, and C. B. Li, “Wettability and boiling heat transfer study of black silicon surface produced using the plasma immersion ion implantation method,” *Appl. Therm. Eng.*, vol. 99, pp. 253–261, 2016.

[78] H. J. Choi, S. Baek, H. S. Jang, S. B. Kim, B. Y. Oh, and J. H. Kim, “Optimization of metal-assisted chemical etching process in fabrication of p-type silicon wire arrays,” *Curr. Appl. Phys.*, vol. 11, pp. S25–S29, 2011.

[79] L. T. Cong *et al.*, “Decisive role of dopants in the optical properties of vertically aligned silicon nanowires prepared by metal-assist chemical etching,” *Opt. Mater. (Amst).*, vol. 121, p. 111632, 2021.

[80] J. Kim, Y. H. Kim, S. H. Choi, and W. Lee, “Curved silicon nanowires with ribbon-like cross sections by metal-assisted chemical etching,” *ACS Nano*, vol. 5, no. 6, pp. 5242–5248, 2011.

[81] H. Han, Z. Huang, and W. Lee, “Metal-assisted chemical etching of silicon and nanotechnology applications,” *Nano Today*, vol. 9, no. 3, pp. 271–304, 2014.

[82] B. Ozdemir, M. Kulakci, R. Turan, and H. E. Unalan, “Effect of electroless etching parameters on the growth and reflection properties of silicon nanowires,” *Nanotechnology*, vol. 22, no. 15, p. 155606, 2011.

[83] H. Morinaga, M. Suyama, and T. Ohmi, “Mechanism of Metallic Particle Growth and Metal-Induced Pitting on Si Wafer Surface in Wet Chemical

Processing," *J. Electrochem. Soc.*, vol. 141, no. 10, pp. 2834–2841, 1994.

[84] R. Li, S. Chuwongin, S. Wang, and W. Zhou, "Ag-Assisted Electrochemical Etching of Silicon for Antireflection in Large Area Crystalline Thin Film Photovoltaics," in *2012 38th IEEE Photovoltaic Specialists Conference*, 2012, pp. 002563–002565.

[85] J. De Boor, N. Geyer, J. V. Wittemann, U. Gösele, and V. Schmidt, "Sub-100 nm silicon nanowires by laser interference lithography and metal-assisted etching," *Nanotechnology*, vol. 21, no. 9, p. 095302, 2010.

[86] H. Asoh, F. Arai, and S. Ono, "Effect of noble metal catalyst species on the morphology of macroporous silicon formed by metal-assisted chemical etching," *Electrochim. Acta*, vol. 54, no. 22, pp. 5142–5148, 2009.

[87] F. Es, M. Kulakci, and R. Turan, "An Alternative Metal-Assisted Etching Route for Texturing Silicon Wafers for Solar Cell Applications," *IEEE J. Photovoltaics*, vol. 6, no. 2, pp. 440–446, 2016.

[88] Z. Huang, N. Geyer, P. Werner, J. de Boor, and U. Gösele, "Metal-assisted chemical etching of silicon: a review.," *Adv. Mater.*, vol. 23, no. 2, pp. 285–308, Jan. 2011.

[89] L. A. Dobrzański and A. Drygała, "Laser processing of multicrystalline silicon for texturization of solar cells," *J. Mater. Process. Technol.*, vol. 191, pp. 228–231, Aug. 2007.

[90] S. Kontermann, T. Gimpel, A. L. Baumann, K. M. Guenther, and W. Schade, "Laser processed black silicon for photovoltaic applications," in *SiliconPV: April 03-05, 2012, Leuven, Belgium, Energy Procedia*, 2012, vol. 27, pp. 390–395.

[91] Z. Fekete, Á. C. Horváth, Z. Bérces, and A. Pongrácz, "Black poly-silicon: A nanostructured seed layer for sensor applications," *Sensors Actuators, A Phys.*, vol. 216, pp. 277–286, 2014.

[92] D. H. Macdonald *et al.*, “Texturing industrial multicrystalline silicon solar cells,” *Sol. Energy*, vol. 76, pp. 277–283, 2004.

[93] K. N. Nguyen *et al.*, “Study of black silicon obtained by cryogenic plasma etching: Approach to achieve the hot spot of a thermoelectric energy harvester,” *Microsyst. Technol.*, vol. 18, no. 11, pp. 1807–1814, 2012.

[94] S. Ma *et al.*, “A theoretical study on the optical properties of black silicon,” *AIP Adv.*, vol. 8, p. 035010, 2018.

[95] Z. Yue, H. Shen, and Y. Jiang, “Antireflective nanostructures fabricated by reactive ion etching method on pyramid-structured silicon surface,” *Appl. Surf. Sci.*, vol. 271, pp. 402–406, 2013.

[96] M. Steglich, T. Käsebier, M. Zilk, T. Pertsch, E. B. Kley, and A. Tünnermann, “The structural and optical properties of black silicon by inductively coupled plasma reactive ion etching,” *J. Appl. Phys.*, vol. 116, p. 173503, 2014.

[97] G. Agarwal, S. De Iuliis, L. Serenelli, E. Salza, and M. Tucci, “Dry texturing of mc-Si wafers,” *Phys. Status Solidi Curr. Top. Solid State Phys.*, vol. 8, no. 3, pp. 903–906, 2011.

[98] J. Hirsch, M. Gaudig, N. Bernhard, and D. Lausch, “Optoelectronic properties of Black-Silicon generated through inductively coupled plasma (ICP) processing for crystalline silicon solar cells,” *Appl. Surf. Sci.*, vol. 374, pp. 252–256, 2016.

[99] L. Stalmans *et al.*, “Porous silicon in crystalline silicon solar cells: A review and the effect on the internal quantum efficiency,” *Prog. Photovoltaics Res. Appl.*, vol. 6, pp. 233–246, 1998.

[100] V. Y. Yerokhov and I. I. Melnyk, “Porous silicon in solar cell structures: a review of achievements and modern directions of further use,” *Renew. Sustain. energy Rev.*, vol. 3, pp. 291–322, 1999.

[101] P. Kleimann, J. Linnros, and R. Juhasz, “Formation of three-dimensional microstructures by electrochemical etching of silicon,” *Appl. Phys. Lett.*, vol. 79, p. 1727, 2001.

[102] E. Vázsonyi *et al.*, “Porous silicon formation by stain etching,” *Thin Solid Films*, vol. 388, pp. 295–302, 2001.

[103] R. J. Martín-Palma, L. Vázquez, J. M. Martínez-Duart, M. Schnell, and S. Schaefer, “Antireflective porous-silicon coatings for multicrystalline solar cells: The effects of chemical etching and rapid thermal processing,” *Semicond. Sci. Technol.*, vol. 16, pp. 657–661, 2001.

[104] X. Liu, P. R. Coxon, M. Peters, B. Hoex, J. M. Cole, and D. J. Fray, “Black silicon: fabrication methods, properties and solar energy applications,” *Energy Environ. Sci.*, vol. 7, pp. 3223–3263, 2014.

[105] L. Tsakalakos, J. Balch, J. Fronheiser, B. A. Korevaar, O. Sulima, and J. Rand, “Silicon nanowire solar cells,” *Appl. Phys. Lett.*, vol. 91, p. 233117, 2007.

[106] Y. Li *et al.*, “Novel Silicon Nanohemisphere-Array Solar Cells with Enhanced Performance,” *Small*, vol. 7, no. 22, pp. 3138–3143, 2011.

[107] M. D. Kelzenberg *et al.*, “Enhanced absorption and carrier collection in Si wire arrays for photovoltaic applications,” *Nat. Mater.*, vol. 9, pp. 239–244, 2010.

[108] C.-L. Cheng, C.-W. Liu, J.-T. Jeng, B.-T. Dai, and Y.-H. Lee, “Fabrication and Characterizations of Black Hybrid Silicon Nanomaterials as Light-Trapping Textures for Silicon Solar Cells,” *J. Electrochem. Soc.*, vol. 156, p. H356, 2009.

[109] Q. Tan, F. Lu, C. Xue, W. Zhang, L. Lin, and J. Xiong, “Nano-fabrication methods and novel applications of black silicon,” *Sensors Actuators, A Phys.*, vol. 295, pp. 560–573, 2019.

[110] E. Garnett and P. Yang, “Light trapping in silicon nanowire solar cells,” *Nano Lett.*, vol. 10, pp. 1082–1087, 2010.

[111] W. C. Hsu, Y. S. Lu, J. Y. Chyan, and J. A. Yeh, “High-efficiency 6″ multicrystalline black solar cells based on metal-nanoparticle-assisted chemical etching,” *Int. J. Photoenergy*, vol. 2012, 2012.

[112] B. Radfar, F. Es, and R. Turan, “Effects of different laser modified surface morphologies and post-texturing cleanings on c-Si solar cell performance,” *Renew. Energy*, vol. 145, pp. 2707–2714, 2020.

[113] F. Es, G. Baytemir, M. Kulakci, and R. Turan, “Metal-assisted nano-textured solar cells with SiO2/Si3N4 passivation,” *Sol. Energy Mater. Sol. Cells*, vol. 160, no. October 2016, pp. 269–274, 2017.

[114] W. C. Wang, M. C. Tsai, J. Yang, C. Hsu, and M. J. Chen, “Efficiency enhancement of nanotextured black silicon solar cells using Al_2O_3/TiO_2 dual-layer passivation stack prepared by atomic layer deposition,” *ACS Appl. Mater. Interfaces*, vol. 7, pp. 10228–10237, 2015.

[115] D. Li *et al.*, “Formation of nanostructured emitter for silicon solar cells using catalytic silver nanoparticles,” *Appl. Surf. Sci.*, vol. 264, pp. 621–624, 2013.

[116] J. Oh, H. C. Yuan, and H. M. Branz, “An 18.2% efficient black-silicon solar cell achieved through control of carrier recombination in nanostructures,” *Nat. Nanotechnol.*, vol. 7, pp. 743–748, 2012.

[117] B. Kafle *et al.*, “On the emitter formation in nanotextured silicon solar cells to achieve improved electrical performances,” *Sol. Energy Mater. Sol. Cells*, vol. 152, pp. 94–102, 2016.

[118] Z. Huang *et al.*, “20.0% Efficiency Si Nano/Microstructures Based Solar Cells with Excellent Broadband Spectral Response,” *Adv. Funct. Mater.*, vol. 26, pp. 1892–1898, 2016.

[119] R. S. Davidsen *et al.*, “Black silicon laser-doped selective emitter solar cell

with 18.1% efficiency," *Sol. Energy Mater. Sol. Cells*, vol. 144, pp. 740–747, 2016.

[120] H. Savin *et al.*, "Black silicon solar cells with interdigitated back-contacts achieve 22.1% efficiency," *Nat. Nanotechnol.*, vol. 10, pp. 624–628, 2015.

[121] P. Repo *et al.*, "N-type black silicon solar cells," *Energy Procedia*, vol. 38, pp. 866–871, 2013.

[122] J. Benick *et al.*, "High-Efficiency n-Type HP mc Silicon Solar Cells," *IEEE J. Photovoltaics*, vol. 7, no. 5, pp. 1171–1175, 2017.

[123] G. Bektaş, "Ion Implanted Homojunction Crystalline Silicon Solar Cells," Middle East Technical University, 2022.

[124] L. Mohr, T. Krick, M. Zimmer, A. Fischer, and A. Moldovan, "Numerical Simulation of an Ozone-Based Wet-Chemical Etching," in *SiliconPV 2019, the 9th International Conference on Crystalline Silicon Photovoltaics*, 2019, p. 050007.

[125] B. Kafle *et al.*, "On the nature of emitter diffusion and screen-printing contact formation on nanostructured silicon surfaces," *2017 IEEE 44th Photovolt. Spec. Conf. PVSC 2017*, vol. 7, no. 1, pp. 1–3, 2017.

[126] G. Scardera *et al.*, "On the Enhanced Phosphorus Doping of Nanotextured Black Silicon," *IEEE J. Photovoltaics*, vol. 11, no. 2, pp. 298–305, 2021.

[127] D. Turkay and S. Yerci, "Two-dimensional numerical analysis of phosphorus diffused emitters on black silicon surfaces," *PVCon 2018 - Int. Conf. Photovolt. Sci. Technol.*, pp. 1–8, 2018.

[128] Y. Xia, B. Liu, J. Liu, Z. Shen, and C. Li, "A novel method to produce black silicon for solar cells," *Sol. Energy*, vol. 85, pp. 1574–1578, 2011.

[129] W. Wang *et al.*, "21.3%-efficient n-type silicon solar cell with a full area rear TiO_x/LiF/Al electron-selective contact," *Sol. Energy Mater. Sol. Cells*,

vol. 206, p. 110291, 2020.

[130] T. Matsui, M. Bivour, P. F. Ndione, R. S. Bonilla, and M. Hermle, “Origin of the tunable carrier selectivity of atomic-layer-deposited TiO_x nanolayers in crystalline silicon solar cells,” *Sol. Energy Mater. Sol. Cells*, vol. 209, p. 110461, 2020.

[131] T. Matsui, M. Bivour, M. Hermle, and H. Sai, “Atomic-Layer-Deposited TiO_x Nanolayers Function as Efficient Hole-Selective Passivating Contacts in Silicon Solar Cells,” *ACS Appl. Mater. Interfaces*, vol. 12, pp. 49777–49785, 2020.

[132] J. Bullock *et al.*, “Lithium Fluoride Based Electron Contacts for High Efficiency n-Type Crystalline Silicon Solar Cells,” *Adv. Energy Mater.*, vol. 6, no. 14, p. 1600241, 2016.

[133] M. Bivour, B. Macco, J. Temmler, W. M. M. Kessels, and M. Hermle, “Atomic Layer Deposited Molybdenum Oxide for the Hole-selective Contact of Silicon Solar Cells,” in *6th International Conference on Silicon Photovoltaics, Energy Procedia*, 2016, vol. 92, pp. 443–449.

[134] M. Bivour, J. Temmler, H. Steinkemper, and M. Hermle, “Molybdenum and tungsten oxide: High work function wide band gap contact materials for hole selective contacts of silicon solar cells,” *Sol. Energy Mater. Sol. Cells*, vol. 142, pp. 34–41, 2015.

[135] J. Geissbühler *et al.*, “22.5% Efficient Silicon Heterojunction Solar Cell With Molybdenum Oxide Hole Collector,” *Appl. Phys. Lett.*, vol. 107, p. 081601, 2015.

[136] B. De Boer, A. Hadipour, M. M. Mandoc, T. van Woudenbergh, and P. W. M. Blom, “Tuning of metal work functions with self-assembled monolayers,” *Adv. Mater.*, vol. 17, no. 5, pp. 621–625, 2005.

[137] G. Ligorio, N. Zorn Morales, and E. J. W. List-Kratochvil, “Large and

continuous tuning of the work function of indium tin oxide using simple mixing of self-assembled monolayers," *Appl. Phys. Lett.*, vol. 116, p. 241603, 2020.

[138] T. Schulmeyer *et al.*, "Modification of $BaTiO_3$ thin films: Adjustment of the effective surface work function," *J. Mater. Chem.*, vol. 17, pp. 4563–4570, 2007.

[139] A. Asyuda *et al.*, "Self-Assembled Monolayers with Embedded Dipole Moments for Work Function Engineering of Oxide Substrates," *J. Phys. Chem. C*, vol. 124, pp. 8775–8785, 2020.

[140] J. Rittich, S. Jung, J. Siekmann, and M. Wuttig, "Indium-Tin-Oxide (ITO) Work Function Tailoring by Covalently Bound Carboxylic Acid Self-Assembled Monolayers," *Phys. Status Solidi*, vol. 255, p. 1800075, 2018.

[141] I. Lange *et al.*, "Tuning the Work Function of Polar Zinc Oxide Surfaces using Modified Phosphonic Acid Self-Assembled Monolayers," *Adv. Funct. Mater.*, vol. 24, pp. 7014–7024, 2014.

[142] A. Petritz *et al.*, "Embedded Dipole Self-Assembled Monolayers for Contact Resistance Tuning in p-Type and n-Type Organic Thin Film Transistors and Flexible Electronic Circuits," *Adv. Funct. Mater.*, vol. 28, p. 1804462, 2018.

[143] O. Acton *et al.*, "Spin-Cast and Patterned Organophosphonate Self-Assembled Monolayer Dielectrics on Metal-Oxide-Activated Si," *Adv. Mater.*, vol. 23, pp. 1899–1902, 2011.

[144] D. Liu, X. Xu, Y. Su, Z. He, J. Xu, and Q. Miao, "Self-Assembled Monolayers of Phosphonic Acids with Enhanced Surface Energy for High-Performance Solution-Processed N-Channel Organic Thin-Film Transistors," *Angew. Chemie*, vol. 125, pp. 6342–6347, 2013.

[145] X. Liu, S. H. Mohamed, J. M. Ngaruiya, M. Wuttig, and T. Michely, "Modifying the growth of organic thin films by a self-assembled

monolayer," *J. Appl. Phys.*, vol. 93, pp. 4852–4855, 2003.

[146] A. Al-Ashouri *et al.*, "Conformal monolayer contacts with lossless interfaces for perovskite single junction and monolithic tandem solar cells," *Energy Environ. Sci.*, vol. 12, pp. 3356–3369, 2019.

[147] A. Al-Ashouri *et al.*, "Monolithic perovskite/silicon tandem solar cell with >29% efficiency by enhanced hole extraction," *Science (80-.).*, vol. 370, no. 6522, pp. 1300–1309, 2020.

[148] Y. Lin *et al.*, "18.4% Organic Solar Cells Using a High Ionization Energy Self-Assembled Monolayer as Hole-Extraction Interlayer," *ChemSusChem*, vol. 14, pp. 3569–3578, 2021.

[149] T. Hatt *et al.*, "Hydrophobic AlO_x Surfaces by Adsorption of a SAM on Large Areas for Application in Solar Cell Metallization Patterning," *ACS Appl. Mater. Interfaces*, vol. 13, pp. 5803–5813, 2021.

[150] W. Ji, T. Allen, X. Yang, G. Zeng, S. De Wolf, and A. Javey, "Polymeric Electron-Selective Contact for Crystalline Silicon Solar Cells with an Efficiency Exceeding 19%," *ACS Energy Lett.*, vol. 5, pp. 897–902, 2020.

[151] C. Reichel *et al.*, "Effect of Thermal Annealing on the Charge Carrier Selectivity of Ultra-Thin Organic Interface Dipoles in Silicon Organic Heterojunction Solar Cells," *Sol. RRL*, vol. 5, p. 2100466, 2021.

[152] Z. Sun *et al.*, "20% efficiency mg/PCBM/p-type silicon hybrid solar cells," *Sol. Energy Mater. Sol. Cells*, vol. 235, p. 111453, 2022.

[153] A. Elschner, F. Jonas, S. Kirchmeyer, and W. Lövenich, "PEDOT-based Layers for TCO-Substitution and Hole-Injection," *SID Symp. Dig. Tech. Pap.*, vol. 39, no. 1, pp. 407–410, 2012.

[154] R. Gogolin, D. Zielke, A. Descoeudres, M. Despeisse, C. Ballif, and J. Schmidt, "Demonstrating the high V_{oc} potential of PEDOT:PSS/c-Si heterojunctions on solar cells," in *7th International Conference on Silicon*

Photovoltaics, SiliconPV 2017, Energy Procedia, 2017, vol. 124, pp. 593–597.

[155] J. F. Butscher *et al.*, “Enhancing the Open-Circuit Voltage of Perovskite Solar Cells by Embedding Molecular Dipoles within Their Hole-Blocking Layer,” *ACS Appl. Mater. Interfaces*, vol. 12, pp. 3572–3579, 2020.

[156] Y. Hou *et al.*, “Efficient tandem solar cells with solution-processed perovskite on textured crystalline silicon,” *Science (80-.).*, vol. 367, pp. 1135–1140, 2020.

[157] C. Reichel *et al.*, “Electron-selective contacts via ultra-thin organic interface dipoles for silicon organic heterojunction solar cells,” *J. Appl. Phys.*, vol. 123, p. 024505, Jan. 2018.

[158] R. Wick-Joliat *et al.*, “Stable and tunable phosphonic acid dipole layer for band edge engineering of photoelectrochemical and photovoltaic heterojunction devices,” *Energy Environ. Sci.*, vol. 12, no. 6, pp. 1901–1909, 2019.

[159] A. Forment-Aliaga and E. Coronado, “Hybrid Interfaces in Molecular Spintronics,” *Chem. Rec.*, vol. 18, pp. 737–748, 2018.

[160] G. M. Whitesides and B. Grzybowski, “Self-assembly at all scales,” *Science (80-.).*, vol. 295, no. 5564, pp. 2418–2421, 2002.

[161] A. Cattani-Scholz, “Functional Organophosphonate Interfaces for Nanotechnology: A Review,” *ACS Appl. Mater. Interfaces*, vol. 9, pp. 25643–25655, 2017.

[162] C. Luderer, C. Messmer, M. Hermle, and M. Bivour, “Transport Losses at the TCO/a-Si:H/c-Si Heterojunction: Influence of Different Layers and Annealing,” *IEEE J. Photovoltaics*, vol. 10, no. 4, pp. 952–958, Jul. 2020.

[163] J. Cho *et al.*, “Passivating electron-selective contacts for silicon solar cells based on an a-Si:H/TiO_x stack and a low work function metal,” *Prog.*

Photovoltaics Res. Appl., vol. 26, no. 10, pp. 835–845, 2018.

[164] M. Liu *et al.*, "SnO_2/Mg combination electron selective transport layer for Si heterojunction solar cells," *Sol. Energy Mater. Sol. Cells*, vol. 200, p. 109996, 2019.

[165] S. Zhong *et al.*, "Mitigating Plasmonic Absorption Losses at Rear Electrodes in High-Efficiency Silicon Solar Cells Using Dopant-Free Contact Stacks," *Adv. Funct. Mater.*, vol. 30, p. 1907840, 2020.

[166] J. Rittich, "The Mechanism of Work Function Tuning with Covalently Bound Self-Assembled Monolayers A Study on Electrode Functionalization for the Optimization of Organic Electronics," Aachen University, 2018.

[167] J. L. Bryan *et al.*, "Aluminum–silicon interdiffusion in silicon heterojunction solar cells with a-Si:H(i)/a-Si:H(n/p)/Al rear contacts," *J. Phys. D. Appl. Phys.*, vol. 54, p. 134002, 2021.

APPENDICES

A. Fast-Firing Profile for PERC Solar Cells

A typical fast-firing profile is shown in Figure A.1.

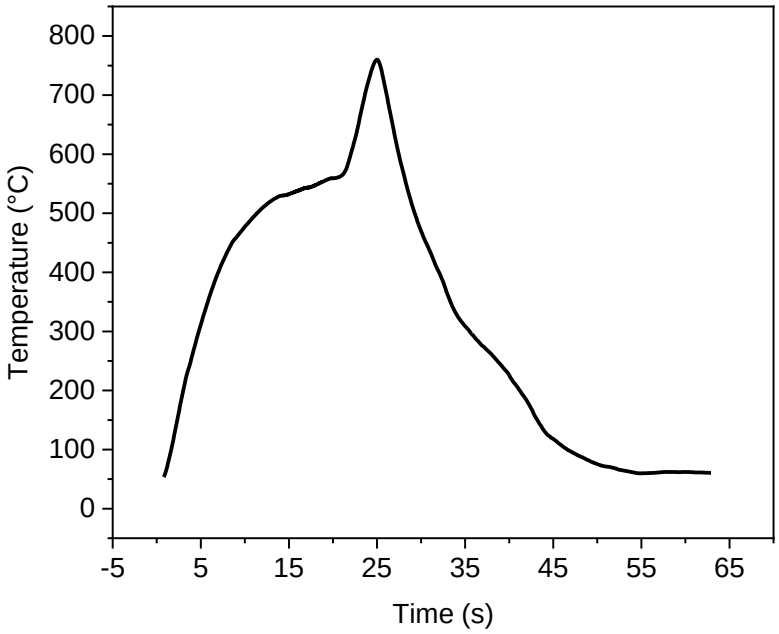

Figure A.7.1 Fast-firing profile for PERC solar cells

CURRICULUM VITAE

PERSONAL INFORMATION

Surname, Name: Sarıgül Duman, Elif
Nationality:
Date and Place of Birth:
Marital Status:
Phone:
email:

EDUCATION

Degree	Institution	Year of Graduation
MS	METU Physics	2014
BS	METU Physics	2011
High School	Kadir Has Anatolian High School, İstanbul	2006

WORK EXPERIENCE

Year	Place	Enrollment
2021-Present	ODTÜ-GÜNAM	Researcher
2019-2021	Fraunhofer ISE	Visitor Scientist
2017-2020	ODTÜ-GÜNAM	Research Assistant
2016-2017	THK University, Aeronautical Eng.	Research Assistant
2011-2016	Atılım University, Physics Group	Research Assistant

FOREIGN LANGUAGES

Advanced English, Elementary German

PUBLICATIONS

1. Sarıgül Duman E., Richter A., Reichel C., Fittkau J., Le Tiec C., Moldovan A. and Benick J. "Al_2O_3/SiN_x Stacks with Ozone-based ALD Al_2O_3 for Surface Passivation: Superior Layer Stability after Firing", AIP Conference Proceedings **2487**, 050005 (2022)

2. Sarıgül Duman E., Kohlstädt M., Reichel C., Tutsch L., Bivour M. and Hermle M. “Self-Assembled Organic Molecule Modified Electron-Selective Contacts for Silicon Heterojunction Solar Cells” AIP Conference Proceedings, (accepted)

3. Sarıgül Duman E., Bektaş G., Keçeci A. E., Canar H. H., Asav H., Aliefendioğlu A. and Turan R. “Influence of Phosphorus Emitter Formation on the Performance of Black Silicon Solar Cells” Renewable Energy, (manuscript in preparation)

4. Soydan M. C., Ghobadi A., Yildirim D. U., Sarıgül Duman E., Bek A., Erturk V. B. and Ozbay E. “Lithography-Free Random Bismuth Nanostructures for Full Solar Spectrum Harvesting and Mid-Infrared Sensing” Advanced Optical Materials, **8**, 1901203 (2020)

5. Doğancı E., Kaya Ş., Aktağ A., Sarıgül Duman E., Turan R., Karaçalı H. and Yılmaz E. “Fabrication and Characterization of Si-PIN Photodiodes” Turkish Journal of Physics, **43**(6), 556-562 (2019)